Detection of Decameter Radio Wave Pulses from the Center Part of Our Galaxy Suggesting Sources at Rotating Super Massive Black Hole Binary

Hiroshi Oya[1,2]

[1]*Geophysical Department, Graduate School for Science, Tohoku University, Aoba, Aramaki, Sendai 980-8578, Japan*
[2]*Space and Astrophysics Research Task, Seisa University, 1805-2, Kokubu-Hongou Oiso, Kanagawa 259-0111, Japan*
e-mail: kan_oya-s@outlook.jp

Citation: Oya, H. (2019), Detection of decameter radio wave pulses from the center part of our Galaxy suggesting sources at rotating super massive black hole binary, 1–50, doi:10.5047/978-4-88704-171-4, TERRAPUB.

Abstract By using the long baseline interferometer for the decameter wavelength radio waves at Tohoku University operated at 21.86 MHz, we observed decameter radio wave pulses from our Galaxy center mainly in June 2016 and June 2017. Due to the extremely low S/N (signal to noise ratio), where the noise is from 300 to 500 times larger than the signal level, the observed interferometer data are uniquely analyzed to detect the source direction. Separation of the signal from the high background noise is accomplished by applying the Interferometer Fringe Function Correlation Method (IFFCM) where the aperture synthesis method of the interferometer data that utilizes the Earth's rotation is modified to eliminate any ambiguity of phase shifts in the system. Pulse forms in the signal are confirmed in the Fourier transformed domain by applying FFT operations to the time series data of the IFFCM; by taking an average of the FFT results over 2016 independent sets, the pulse frequencies are separated from the background white noise. The resulting signals indicate a source direction identified to be at Sgr A* within ±6 arc minutes. The signals are characterized by an ensemble of pulses with fundamental periods of (173 ± 1) sec and (148 ± 1) sec corresponding to the spin periods of two sources which we call Gaa and Gab, respectively, whose frequencies periodically vary with a common period of (2200 ± 50) sec. We suggest being based on Kerr black hole theory that Gaa and Gab are super massive Kerr black holes, with masses of $(2.27 \pm 0.02) \times 10^6 M_\odot$ and $(1.94 \pm 0.01) \times 10^6 M_\odot$, respectively, and with a total mass of $(4.22 \pm 0.03) \times 10^6 M_\odot$ form a binary system orbiting at 2200 ± 50 sec.

Keywords: Center of our Galaxy, decameter radio wave, interferometer observations, black hole binary.

1. INTRODUCTION

After the first suggestion that a massive black hole might exist at the center of our Galaxy (Lynden-Bell and Rees, 1971), a sequence of results from successful research has suggested a limit to the mass of the possible super massive black hole. In the early phase of the studies the possibility of a super massive black hole had been estimated from observations of gas flows in the central few parsecs of the Galactic center (Lacy *et al*., 1980; Serabyn and Lacy, 1985). By using radio waves Lo and Clausen (1983) investigated the flow of the ionized gas within 1.5 pc of the Galactic center. After a series of studies to search for a super massive black hole from the signature of gravity on gas motions that suggested a mass concentration of $3\sim4 \times 10^6 M_\odot$ (Serrabyn and Lacy, 1985), a new era in the search for the black hole at the Galactic center has come; that is, studies on detailed observations of individual stellar motions have been initiated. After the initial work to trace the orbits of the individual stars around Sgr A* (Genzel and Eckart, 1999; Fragile and Mathews, 2000; Ghez *et al*., 2000), we now can track the paths of close to 40 stars, especially the star labelled S2 (S02) (e.g. Gillessen *et al*., 2017) that approaches Sgr A* to within 125 AU (Genzel *et al*. and Review and References therein). All of the efforts associated with the collaborative works to track the individual stars ultimately approached the goal, indicating that the Galactic center contains a highly concentrated mass of about $(4.28 \pm 0.31) \times 10^6 M_\odot$ using a distance coupled with determination of the location of Sgr A* at 8.33 ± 0.12 kpc (Gillessen *et al*., 2017).

Quite independently of the current work we initiated a study to detect decameter radio wave pulses whose periods we assumed to synchronize with the spins of possible super massive black holes at the Galactic center. Decameter radio waves have low frequency characteristics that might be caused by relativistic effects near the region extremely close to the event horizon of spinning black holes, i.e., Kerr black holes. After the discovery of Jansky (1933), it has become common knowledge that decameter radio waves are the dominant components in the Galaxy disk and the center part as well. We then recognized that even if there exists a

doi:10.5047/978-4-88704-171-4

coherent component of the decameter radio waves generated at sources close to the event horizon of possible Kerr black holes, such waves could be buried within the extremely intense background noise. In other words, existing information from the central objects has never been detected throughout the history of radio astronomy for more than three-quarters of a century.

The purpose of the present paper is to describe recent progress of the observations and data analyses of decameter radio waves from the center of our Galaxy, using the long baseline interferometer for the decameter wavelength radio waves at Tohoku University operated at 21.86 MHz. Observations were carried out mainly in June 2016 and June 2017. The data analyses show an ensemble of pulses emitted from rotating compact objects that can be attributed to the existence of massive spinning black holes.

The objective signals are under extremely low S/N conditions where the signal power is less than 1/300∼1/500 of the total sky noise; even when we collimate the receiving direction using the interferometer, the noise power level is still higher by 15 dB than the objective signals. Since a large number of averaging times are required, we apply a unique method to analyze the observed interferometer data. We detect the source direction by separating the signal from the extremely high background noise by applying the Interferometer Fringe Function Correlation Method (IFFCM) where the standard aperture synthesis method of the interferometer data that uses the Earth's rotation is modified to eliminate ambiguity of the phase shifts in the system. Details of IFFCM will be given in Sec. 5.

Pulse forms in the signal are confirmed in the Fourier transformed domain obtained by applying a FFT to the time series data of IFFCM; by taking the sufficient average of the FFT results over 2016 independent sets, the pulse frequencies are clearly separated from the background white noise. The resulting signals whose source direction is within ±6 arc minutes of Sgr A* are characterized by an ensemble of pulses with fundamental periods of (173 ± 1) sec and (148 ± 1) sec corresponding to two sources that we call Gaa and Gab, respectively. These frequencies periodically vary with a common period of (2200 ± 50) sec. A fatal problem for decameter observations of celestial objects is the ionospheric effect, which biases the observed source direction due to refraction through the ionosphere. Since the ambiguity of the phase differences of the signals received at each station of the interferometer can be eliminated by IFFCM, the possible bias due to ionosphere propagation is also eliminated by taking the unknown phase shift caused by ionosphere propagation to be equivalent to the ambiguity of the phase differences at each station of the interferometer; due to this elimination function, we are able to virtually shift the interferometer stations outside the ionosphere. Details for this direction finding processes will be described in Sec. 8.

There are criticisms for the possibility of detecting decameter radio wave pulses emitted from the sources located at the center of our Galaxy, from the standpoints of propagation conditions. The first point is that the scattering of the decameter radio waves propagating through the long distance in Galactic space causes blurring or elimination of the pulse forms due to mixing of the time delaying components from the multi-paths. The second point is the existing high plasma density near the Galaxy center where the plasma density and therefore the corresponding plasma frequency are much higher than the decameter radio wave frequency.

With respect to the first point of criticism, the problem is raised from today's paradigm to understand the propagation effects due to multiple paths by discarding the bandwidth of the signal on the pulse propagations. That is, in the well-known theory of the effects of multiple paths (Little, 1968; Sheuer, 1971) it is simply considered that the overlapping of arriving signals of a single frequency with no bandwidth takes place between signals which are taking different paths due to scattering by plasma irregularities. This means that there is no constraint to make the overlap of time delayed signals blur the pulse shape. We consider that setting the bandwidth is essential to send the pulses; when the correlation is lost for signals within a bandwidth, no pulse can be transmitted and is received just as noise. If we select a suitably narrow bandwidth to receive the pulse form for the observation system, we are not bothered by arriving incoherent single frequency signals which take multi-paths due to the scattering because they are considered as noise. We receive coherent signals, within a selected bandwidth, which endure mild refraction processes that do not harm the original wave forms. These subjects are described in Sec. 3.

The second criticism is raised by considering a simple non-magnetized plasma in propagating media where the electromagnetic waves with frequencies lower than the plasma frequency cannot propagate. It has been widely accepted, however, in solar system plasma physics that electromagnetic waves with much lower frequency than the local plasma frequency are able to propagate in the form of whistler mode electromagnetic waves. The existence of the magnetic fields near the event horizon of the black hole is evident (see Eatough *et al*., 2013, for an example). The original radio waves generated in the form of a whistler mode then propagate by changing modes to the ordinary mode of electromagnetic waves in plasma by adapting to the environment of propagation. This subject will be described in detail in Sec. 9.

The deduced spectra that are characterized by multiple side bands with a given frequency gap correspond to frequency modulations caused by orbital motions of two objects possibly to be a binary black hole. Analyses of the Doppler effects indicate orbital motions for two objects, in assumed circular orbits with period of (2200 ± 50) sec, that are moving at around 18% and 21% of the speed of light. Considering Newtonian dynamics, we thus suggest that there is a massive black hole binary with masses of $(2.27 \pm 0.02) \times 10^6 M_\odot$ and $(1.94 \pm 0.01) \times 10^6 M_\odot$. These resulting masses are the minimum possible values because calculations are based on an assumption of coincidence of the orbital plane with the line of sight from the observer. Nevertheless, the total mass of the presently deduced mass is $(4.22 \pm 0.03) \times 10^6 M_\odot$ that is extremely close to the latest results of the black hole mass $(4.35 \pm 0.13) \times 10^6 M_\odot$ at the Galactic center (Gillessen *et*

doi:10.5047/978-4-88704-171-4

al., 2017). This subject will be described in detail in Sec. 10.

Apparently the results of this paper have encountered a paradigm problem which states that an extremely massive black hole binary moving within a short distance of 0.27 AU exists with stable orbits without losing the orbital potential energy via radiation of gravitational waves. We do not deny the present results; however, because the present paradigms for gravitational waves from a black hole still require improvement; even the origin of the gravitational force is left for future studies in the field of astrophysics and physics of gravitational forces. These subjects are deferred for our next paper.

2. OBSERVATION SYSTEM

2.1 System General

The principal instrumentation for the present study is based on the long baseline interferometer of decameter radio waves established by Tohoku University in Miyagi Prefecture, Japan. The system consists of three stations at Yoneyama, Zao, and Kawatabi, which receive signals of cosmic origin. The locations of these observation stations are listed in Table 1 (see Fig. 1 also). The receiving systems of the interferometer consist of a 10 m tip to tip Yagi antenna which is followed by preamplifier and the main receiver that is equipped with a 4 stage super-heterodyne system of 500 Hz bandwidth with a sensitivity of −130 dBm (see Fig. 2). The observations for this study were made at 21.86 MHz, which is down converted to 1 kHz with a bandwidth of 500 Hz; the signals with a central frequency of 1 kHz are then sent from each observation station of the interferometer system to the central station at Sendai through the FM telemetry system. To keep the phase of the observed signals constant, all supplied local signals of the super heterodyne systems and telemetry carrier signals are controlled their phase by the cesium vapor time standard at the signal generator located at each station.

Table 1. Location of the stations of the interferometer system.

Station	Latitude	Longitude
Yoneyama	38°36′50.3″	141°14′33.1″
Zao	38°06′32.4″	140°31′34.5″
Kawatabi	38°45′04.5″	140°45′44.0″

At the main station at Sendai, the signals received by the FM telemeter system are demodulated to recover the original signals at the receiving points. Reproduced signals converted to 1 kHz with 500 Hz bandwidth are divided into three channels whose center frequencies are set, for each observation station, at 900 Hz, 1000 Hz, and 1100 Hz, using narrow band active filters with a bandwidth of 100 Hz. The necessity of narrow band filters will be described in Sec. 3 of this paper. In the last stage of the data acquisition system at main station at Sendai, the received signals of nine channels in total corresponding to each signal from three stations being divided into three channels, are converted into digital data series through the AD converter which provides 3000 or 6000

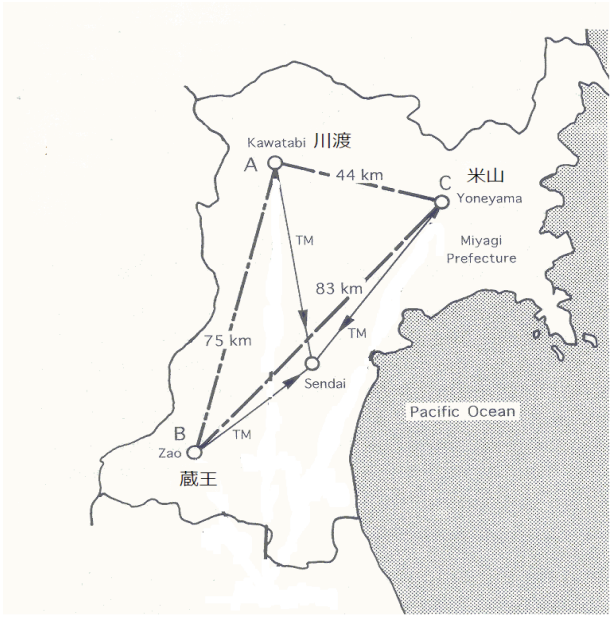

Fig. 1. Location of the station of the Tohoku University decameter radio wave long base line interferometer in Miyagi Prefecture, Japan. The interferometer consists of three observation stations at Yoneyama, Zao and Kawatabi; the received signals are sent to main station at Sendai where formation of the correlation function of the interferometer data is carried out.

data points (with 16 bits for each) per a second. The total data of 4 GB or 8 GB which are obtained by five hours of continuous observation at the three stations for every night of observation are stored on hard disk derived memory devices.

2.2 Antenna and Interferometer Resolution

The antenna at each station is non resonant type five element Yagi whose main beam is fixed in the direction of the exact local south with elevation angle of 45 degree. The beam width to verify the antenna directivity is corresponding to the antenna gain of 12 dB. While the resolution of the direction finding of the sources is wide, as will be described in Sec. 8, the principal function of the direction finding of signal sources is rely on the interferometer function without depending on individual antenna directivity at each stations of interferometer system; but when the resolution becomes fine to be about 0.1 degree, the direction finding is affected by directivity of the local antenna. When we apply the orthodox method to decide the source direction, the potential capability of the present interferometer system may show the spec that are given in Table 2. In the present work, however, we do not employ the orthodox method, because of extremely low signal to noise ratio which forces the long time integration of the data, but utilize a method called here Interferometer Fringe Function Correlation Method (IFFCM) where the time depending data series of interferometer (fringe function) caused by the earth rotation is utilized. In IFFCM no calibration for the absolute phase shifts of the systems is required because these unknown quantities can be eliminated analytically in the processes of IFFCM as details will be given in Sec. 5. To calculate correlation between the

doi:10.5047/978-4-88704-171-4

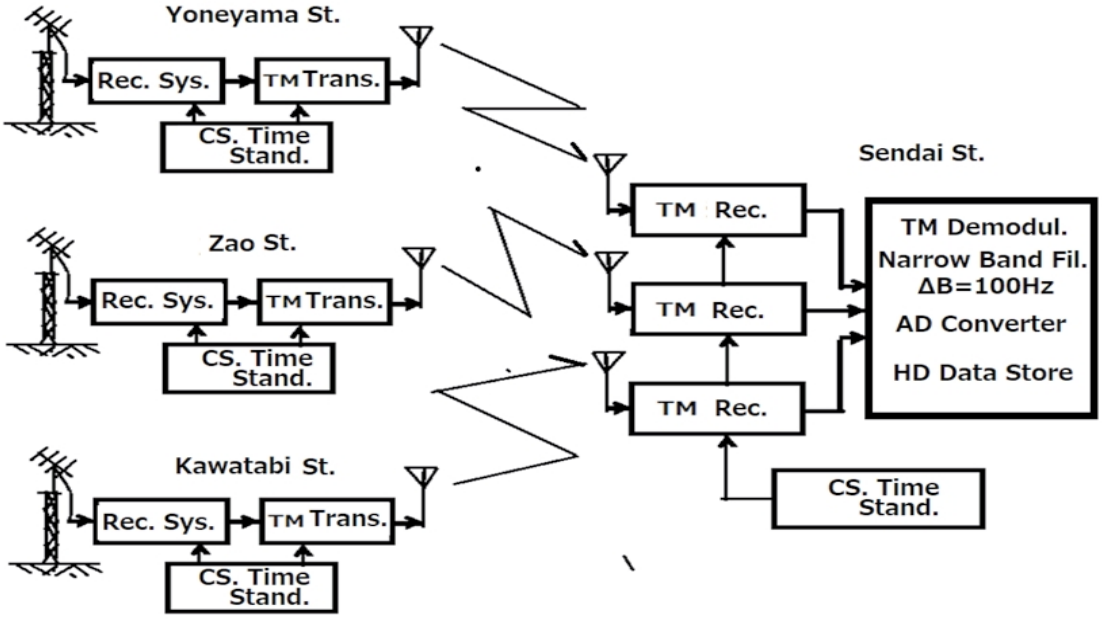

Fig. 2. The block diagram showing the core function of the interferometer system. Data detected by the main receiver are transported by the FM telemeter system to Sendai where demodulated original signals are divided into three channels, for each station, through narrow band filters with bandwidth of 100 Hz. Data through the three channels assigned to each station are converted into digital data series through the AD converter which provides 3000 or 6000 data points (with 16 bits for each) per second. The total data of 4 GB or 8 GB which are obtained by five hours of continuous observation at the three stations for every night of observation are stored on hard disk derived memory devices.

Table 2. Potential resolution of the interferometer system.

Arriving	K-Z (77 km)	Y-Z (83 km)	Y-K (44 km)
Angle (degree)	Arc sec	Arc sec	Arc Sec
10	108.7	98.2	185.2
20	55.18	49.86	94.05
30	37.74	34.11	64.33
40	29.36	26.53	50.04
50	24.63	22.26	41.99
60	21.79	19.69	37.14
70	20.08	18.15	34.23
80	19.16	17.32	32.66
90	18.87	17.05	32.17

template fringe function to search for source direction and observed fringe function in IFFCM, integration of functions during an essentially required period is inevitable; the integration reduces the resolution of the detected source direction largely instead of advantage to reduce the back ground noise and elimination of the ionosphere effects which bother the detection of the source direction as also it will be given in Sec. 7. Then resolution of the direction finding of system becomes much wider (6 arc min: see Sec. 5) than the nominal potential values given in Table 2.

3. NECESSITY OF NARROW BAND DATA SAMPLING

The established theory for the pulse transmission across the long distance of the interstellar medium express that the pulse form is distorted by multiple-path effects due to the scattering of the propagating radio waves by existing irregularities of plasma distributions. In the traditional description of the multiple-path theory (Little, 1968; Sheuer, 1971) a transmitted pulse is divided into multiple components whose arrival times are not synchronized but diverge within an average time interval ΔT that is expressed by $(L/2c)\bar{\theta}^2$ where L and c are the propagation distance and the light velocity, respectively; $\bar{\theta}$ is the deviation of arriving angle of radio waves

doi:10.5047/978-4-88704-171-4

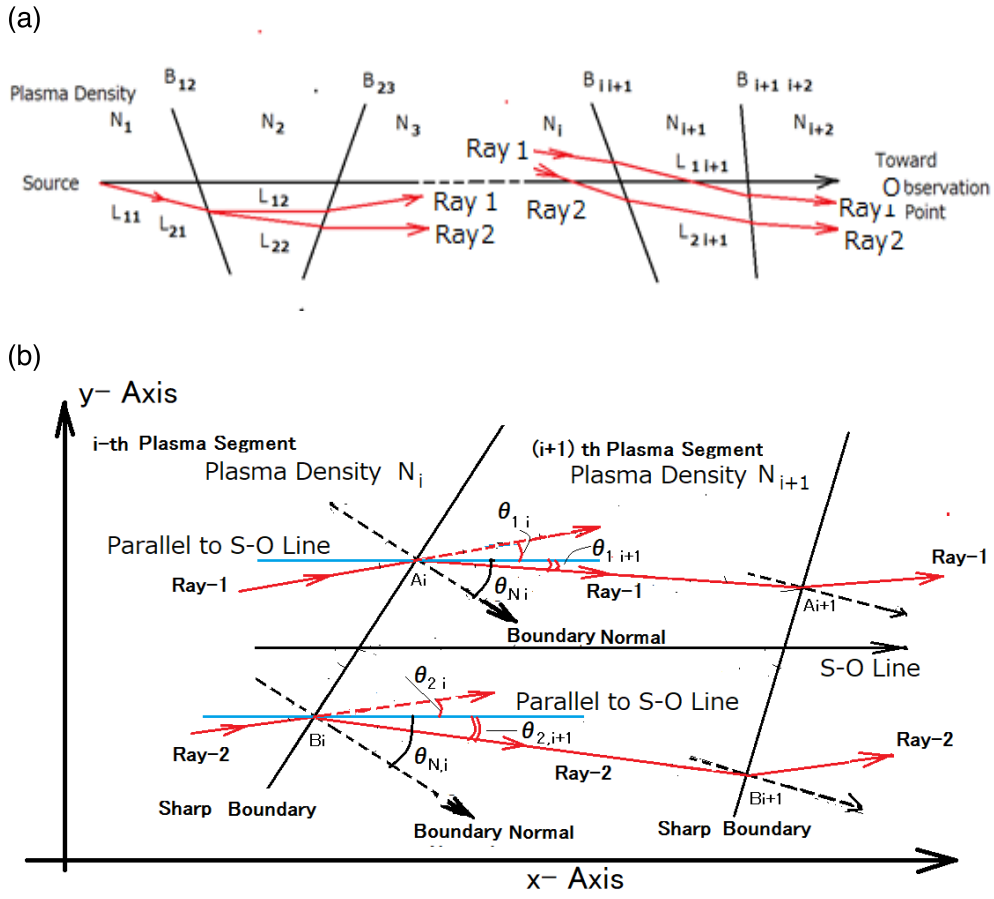

Fig. 3. (a) The model of the propagation environment with plasma density irregularity Plasma irregularity is represented by series of segments of different plasma density N_{i+1} for the region separated by two sharp boundaries B_{ii+1} and $B_{i+1\,i+2}$. Ray1 and Ray2 represent the low frequency limit and high frequency limit of the transporting pulse within a given frequency band, respectively. (b) Detailed depiction of the i-th and $(i+1)$-th plasma segments for the macroscopic geometry given in Fig. 3(a) with the concept of ray paths that are refracted at the corresponding sharp boundary.

that is given by

$$\bar{\theta} = \theta_0 \exp\left(-\frac{\theta^2}{\theta_0^2}\right), \tag{1}$$

where $\theta_0 = (1/8\pi^2)(\Delta\omega_P/\omega)^2\sqrt{L/\ell}$; ℓ is thickness of the equivalent screen. and $\Delta\omega_P$ is defined as the "average perturbation of plasma angular frequency" that is expressed for the average plasma density perturbation ΔN in an irregular plasma media as,

$$\Delta\omega_P^2 = (\Delta N)e^2/m\epsilon_0 \tag{2}$$

with electron charge e, electron mass m and dielectric constant ϵ_0 for vacuum in mks units. The results of the pulsar studies (Rankin *et al*., 1970), which were made observation in the UHF frequency range at 400 MHz for the pulsar at the Crab nebula located at a distance of about 7000 ly, indicate that the blurring time of the arrival of the pulsar signal is 0.3 m sec. If we follow the same category for the observations of the pulse from the center part of our Galaxy at 8.3 kpc distance, for decameter radio waves at 21.86 MHz, the blurring time becomes almost a few hundred sec. This means that we are not able to make accurate observations of the pulse signal from the Galactic center at a low frequency range around 20 MHz.

We find, however, that there is a discrepancy in the current multiple-path theory which concerns only wide band signals where the importance of bandwidth is ignored. That is, as an asymptotic stage of the wide band system, only a single frequency represents signals which are subjected to the multiple-path effect in the traditional multi-path theory for the waves propagating through the interstellar plasma. We propose then the necessity of a bandwidth for the effective detection of the pulse form transmitting through the interstellar medium. That is, we employ the concept of observations within a narrow frequency band where the correlation of the signals is maintained to carry the pulse forming a wave packet even when propagating through long distances through the interstellar medium with irregular plasma distributions. We call this theory, based on the concept of narrow frequency band observation, the coherent refraction theory.

In this coherent refraction theory, we trace the propagation paths of two representative frequencies (the highest and lowest frequencies within a given frequency band) at which signals maintain correlation through the entire propagation course. In Fig. 3(a), the model of the propagation paths is

doi:10.5047/978-4-88704-171-4

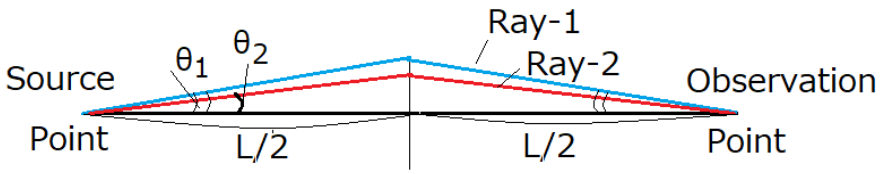

Fig. 4. Symmetry model of the difference of propagation paths between ray-1 and ray-2 corresponding to Eq. (14).

given for two representative frequencies to carry the pulse; the plasma distribution with irregularity is expressed by segments with sharp boundary surfaces whose normal is oriented randomly. To express the coherent refraction condition in detail, for the radio waves with two representative frequencies to transport a pulse, the geometry of the rays and boundary of the model irregularity are indicated in Fig. 3(b) where the ray directions for two representative radio waves in the i-th and $(i+1)$-th part of the irregularity segments are indicated by the deviation angle θ_{Ni} of the boundary normal direction from the direction of the source—observation points line (S-O line). The deviation angle θ_{Ni} of the boundary normal of i-th segments from the S-O line fall within angle ranges, $-90^\circ \le \theta_{Ni} \le 90^\circ$.

In Fig. 3(b), the Ray-1 and Ray-2 with frequency ω and $\omega + \Delta\omega$, respectively, which represent a pulse encounter with the sharp boundary of the plasma irregularity at the points A_i and B_i. As it has been indicated, propagation directions of rays and boundary normal are described in x-y coordinate where S-O line becomes x axis while y axis is defined perpendicular to the S-O line. Then at the points A_i and B_i, the wave normal vectors $\boldsymbol{k}_\alpha$ for ray-α ($\alpha = 1$ for Ray-1 and $\alpha = 2$ for Ray-2) and vector of the boundary normal $\boldsymbol{n}_i$ are express with unit vectors $\boldsymbol{x}$ and $\boldsymbol{y}$ directed to x and y axes, respectively, as

$$\boldsymbol{k}_{\alpha i} = \cos\theta_{\alpha i}\boldsymbol{x} + \sin\theta_{\alpha i}\boldsymbol{y}, \tag{3}$$

$$\boldsymbol{k}_{\alpha\, i+1} = \cos\theta_{\alpha\, i+1}\boldsymbol{x} + \sin\theta_{\alpha\, i+1}\boldsymbol{y}, \tag{4}$$

and

$$\boldsymbol{n}_i = \cos\theta_{Ni}\boldsymbol{x} + \sin\theta_{Ni}\boldsymbol{y}. \tag{5}$$

Then incident angle $\theta_{I\alpha i}$ is expressed in the following relationship as

$$\boldsymbol{n}_i \cdot \boldsymbol{k}_{\alpha i} = \cos\theta_{I\alpha i}. \tag{6}$$

From Eqs. (3), (5) and (6) the incident angle of the ray-α is given by

$$\theta_{I\alpha i} = \theta_{Ni} - \theta_{\alpha i}. \tag{7}$$

After passing through the i-th boundary, ray-α propagates in the direction with angles $\theta_{\alpha\, i+1}$ ($\alpha = 1$ and 2) with respect to the S-O line. The details of the mathematical manipulations are given in Appendix A where we trace the refraction of two rays that represent pulse transmission from the source to the observation points. When we introduce the perturbation density ΔN_i that are related to the density N_i of the plasma at the i-th segment (see Fig. 3(a) and 3(b)) with the average plasma density N_a as

$$N_i = N_a + \Delta N_i, \tag{8}$$

and the difference of the boundary normal between i-th and $(i+1)$-th boundary as

$$\theta_{N\, i,i+1} = \theta_{N\, i+1} - \theta_{N\, i}, \tag{9}$$

we can express the deviation angle $\theta_{\alpha\, i+1}$ of the ray-α in the $(i+1)$-th plasma segment, taking M as $i+1$ for Eq. (A.18) in Appendix A, as

$$\begin{aligned}\theta_{\alpha\, i+1} &= -\frac{1}{2}\left(\frac{\omega_{pU}}{\omega_\alpha}\right)^2 \cdot \sum_{j=i}^{i+1} \Delta N_{j+1} \cdot \Delta\theta_{Nj,j+1} \\ &= -\frac{1}{2}\left(\frac{\omega_{pU}}{\omega_\alpha}\right)^2 \Delta N_{i+1} \cdot \Delta\theta_{Ni,i+1}.\end{aligned} \tag{10}$$

The path length $\xi_{\alpha\, i+1}$ for propagation, through the $(i+1)$-th plasma segment, is then expressed assuming small $\theta_{\alpha\, i+1}$ with width L_{i+1} of the $(i+1)$-th segment, as

$$\xi_{\alpha\, i+1} = \frac{L_{i+1}}{\cos\theta_{\alpha\, i+1}} = L_{i+1}\left(1 + \frac{1}{2}\theta^2_{\alpha\, i+1}\right). \tag{11}$$

That is, the total propagation path lengths ΔL between ray-1 and ray-2 is expressed by

$$\Delta L = \sum_{i=1}^{\mathrm{Max}} (\xi_{1\, i} - \xi_{2\, i}) = \frac{1}{2}\sum_{i=1}^{\mathrm{Max}} L_i(\theta^2_{1\, i} - \theta^2_{2\, i}) \tag{12}$$

where Max indicates the maximum number of the segments at the observation point.

As details have been described in Appendix B, we can write $\theta^2_{\alpha\ \mathrm{Max}}\ (= \theta^2_\alpha)$ with σ_N and σ_θ of the standard deviations of Gaussian distribution for ΔN_i and $\Delta\theta_{Ni-1,i}$, respectively, as

$$\theta^2_{\alpha\ \mathrm{Max}} \equiv \theta^2_\alpha = \frac{1}{4}\left(\frac{\omega_{pU}}{\omega_\alpha}\right)^4 \sigma^2_N \sigma^2_\theta. \tag{13}$$

The relation given by Eq. (12) can be rewritten by

$$\Delta L = \frac{1}{2}\sum_{i=1}^{\mathrm{Max}} L_i(\theta^2_{1i} - \theta^2_{2i}) = \frac{1}{2}L_\cdot(\theta^2_1 - \theta^2_2). \tag{14}$$

doi:10.5047/978-4-88704-171-4

Table 3. Observation list of Galaxy center by long base line interferometer.

Date in 2016	Start Time (JST)	Stop Time (JST)	Average Group
June 5 to June 6	23:30:00	04:30:00	GA-1
June 6 to June 7	23:30:00	04:30:00	GA-1
June 7 to June 8	23:30:00	04:30:00	GA-1
June 8 to June 9	23:30:00	04:30:00	GA-1
June 9 to June 10	23:00:00	04:00:00	GA-1
June 15 to June 16	23:00:00	04:00:00	Not Utilized
June 16 to June 17	23:00:00	04:00:00	GA-1
June 17 to June 18	23:00:00	04:00:00	GA-1
June 18 to June 19	23:00:00	04:00:00	GA-2
June 20 to June 21	23:00:00	04:00:00	GA-2
June 21 to June 22	23:00:00	04:00:00	GA-2
June 22 to June 23	23:00:00	04:00:00	Not Utilized
June 26 to June 27	23:00:00	04:00:00	GA-2
June 27 to June 28	23:00:00	04:00:00	GA-2
June 28 to June 29	22:00:00	03:00:00	GA-2
June 29 to June 30	22:00:00	03:00:00	GA-2

We can express the propagations of the ray-1 and ray-2 by a model given in Fig. 4. Assuming standard deviation of the variation of the plasma density to be maximum which is close to plasma density of Galaxy space N_G, and assuming that the standard deviation of the variation of boundary normal direction of each irregular segment takes a maximum of $\pi/2$, we can express:

$$\Delta L = \frac{\pi^2}{32}\sum_{i=1}^{\mathrm{Max}} L_i\left[\left(\frac{\omega_G}{\omega_1}\right)^4 - \left(\frac{\omega_G}{\omega_2}\right)^4\right] = \frac{\pi^2}{32}L\left[\left(\frac{\omega_G}{\omega_1}\right)^4 - \left(\frac{\omega_G}{\omega_1+\Delta\omega}\right)^4\right]. \quad (15)$$

From Eq. (15), the propagation path length ΔL between the cases of the ray-1 and ray-2 is, then, expressed by

$$\Delta L = \frac{\pi^2}{8}L\left(\frac{\omega_G}{\omega_1}\right)^4 \cdot \frac{\Delta\omega}{\omega_1}. \quad (16)$$

For L of 8.3 kpc between the Galactic center and an observation point, the difference time ΔT of the arrival of ray-1 and ray-2 that is given by $\Delta L/c$ with Eq. (16) is estimated using the deduced average electron density fluctuation based on observation of the Crab pulsar (Rankin *et al*., 1970). The delay time at the frequency 21.860 MHz with bandwidth of 100 Hz is deduced to be 0.6 msec; this means that we can detect pulses from the Galactic center with periods larger than 10 msec (for an examole), even with the decameter wavelength range radio waves when we select the suitable narrowband width.

Before closing this Sec. 3, we should notify that some of mathematical symbols utilized in this Sec. 3 will appear in the other section of this paper; those symbols which will appear in other section, however, are not utilized with same meaning as defined in Sec. 3; but they will indicate the significance defined in the corresponding section.

4. OBSERVATION

Observations of decameter radio waves operating with the described interferometer system were made during three intervals. The first period is in June 2016, the second period is from December 2016 to February 2017, and the third period is June 2017. The first and the third periods aim directly at the Galactic center, while the second period is for observation of the sky noise when we were not looking at the Galactic center. These are listed in Tables 3, 4 and 5. All observations were made at 21.860 MHz and data were stored in the manner given in Table 6.

5. INTERFEROMETER FRINGE FUNCTION CORRELATION METHOD (IFFCM)

5.1 Production of Interferometer Fringe Data

The radio waves received by the interferometer system at 21.86 MHz is down converted to three channels in frequency ranges centered at 900 Hz, 1000 Hz, and 1100 Hz with bandwidth of 100 Hz at the final stage where the analog data are converted into digital data with conversion rate of 3000 data points per a second.

We can express the data $D_i(\omega, t)$ received at the i-th station i.e., data sent to center station Sendai from Yoneyama, Zao, and Kawatabi station, as

$$D_i(\omega, t) = N_i(\omega, t) + S_i(\omega, t). \quad (17)$$

That is, data $D_i(\omega, t)$ are received electric field intensities of signals $S_i(\omega, t)$ together with background noises $N_i(\omega, t)$ that are modified by directivity of the primary antenna whose

doi:10.5047/978-4-88704-171-4

Table 4. Observation list of non Galaxy sky by long base line interferometer.

Date	Start Time (JST)	Stop Time (JST)	Average Group
December 5 in 2016	01:00:00	06:00:00	NGA-1
December 8 in 2016	01:00:00	06:00:00	Not Utilized
December 13 in 2016	01:00:00	06:00:00	NGA-1
December 19 in 2016	01:00:00	06:00:00	NGA-1
December 20 in 2016	01:00:00	06:00:00	NGA-1
December 21 in 2016	01:00:00	06:00:00	NGA-1
December 27 in 2016	01:00:00	06:00:00	NGA-1 & NGA-2
December 28 in 2016	01:00:00	06:00:00	NGA-1 & NGA-2
January 10 in 2017	01:00:00	06:00:00	NGA-2
January 11 in 2017	01:00:00	06:00:00	NGA-2
January 17 in 2017	01:00:00	06:00:00	NGA-2
January 20 in 2017	01:00:00	06:00:00	NGA-2
February 13 in 2017	01:00:00	06:00:00	NGA-2

Table 5. Observation list of Galaxy center by long base line interferometer.

Date in 2017	Start Time (JST)	Stop Time (JST)	Average Group
June 7 to June 8	23:30:00	04:30:00	GA-3
June 8 to June 9	23:30:00	04:30:00	GA-3
June 11 to June 12	23:30:00	04:30:00	GA-3
June 12 to June 13	23:30:00	04:30:00	GA-3
June 13 to June14	23:30:00	04:30:00	GA-3
June 14 to June 15	23:30:00	04:30:00	GA-3
June 18 to June 19	23:00:00	04:00:00	GA-3
June 19 to June 20	23:00:00	04:00:00	GA-4
June 20 to June 21	23:00:00	04:00:00	GA-4
June 21 to June 22	23:00:00	04:00:00	GA-4
June 22 to June 23	22:30:00	03:30:00	GA-4
June 25 to June 26	22:30:00	03:30:00	GA-4
June 26 to June 27	22:30:00	03:30:00	GA-4
July 02 to July 03	22:30:00	03:30:00	GA-4

Table 6. Observation station and data channel with data volume spec.

Station	900 Hz	1000Hz	1100Hz
Yoneyama	Channel 1	Channel 4	Channel 7
Zao	Channel 2	Channel 5	Channel 8
Kawatabi	Channel 3	Channel 6	Channel 9
Data Volume for a Night (5 Hour) Observation	(Channel 1 to 3) 3.4 GB	(Channel 4 to Channel 9) 7.2 GB	

doi:10.5047/978-4-88704-171-4

details will be described in Subsec. 8.3; about sky noise $N_i(\omega, t)$ it should be noticed, in the present works, that $N_i(\omega, t) \gg S_i(\omega, t)$. The signal data are, here, expressed as

$$S_i(\omega, t) = S_{i0}(t) \cdot \cos(\omega t - \boldsymbol{k}_s \cdot \boldsymbol{r}_i + \theta_i) \tag{18}$$

where $S_{i0}(t)$, ω, $\boldsymbol{k}_s$, $\boldsymbol{r}_i$, and θ_i are the pulse form of the present quest, angular frequency of signals at the final stage, the wave number vector of radio waves, the position vector of the i-th station of the interferometer, and the phase shift angle of the observation system at the i-th station, respectively.

To detect the source direction, interferometer data $I_{ij}(t)$ are produced by multiplying the data from the partner stations, i.e., multiplying between data from Yoneyama and Zao, data from Zao and Kawatabi, and data from Kawatabi and Yoneyama, that is

$$\begin{aligned} I_{ij}(t) &= \langle D_i(\omega, t) \cdot D_j(\omega, t) \rangle \\ &= \frac{1}{T} \int_t^{t+T} D_i(\omega, t) \cdot D_j(\omega, t) \cdot dt \end{aligned} \tag{19}$$

where T is the integration time interval selected to be sufficiently long for reduction of the high frequency components ω but sufficiently short not to deform the pulse component in the signal. By substituting Eq. (17), Eq. (19) is rewritten as

$$\begin{aligned} I_{ij}(t) = \frac{1}{T} \int_t^{t+T} & [N_i(t) + S_{i0}(t) \cdot \cos(\omega t - \boldsymbol{k}_s \cdot \boldsymbol{r}_i + \theta_i)] \\ & \cdot [N_j(t) + S_{j0}(t) \cdot \cos(\omega t - \boldsymbol{k}_s \cdot \boldsymbol{r}_j + \theta_j)] dt. \end{aligned} \tag{20}$$

About the noise $N_i(t)$ detected at i-th station, in the above Eq. (20), we consider widely distributed noise sources in the sky; the directions of noise sources are indicated by dividing whole sky into meshes with number $\ell \times m$. The numbers ℓ and m are defined to indicate the position of the noise sources in the celestial sphere; the details to define ℓ and m will be described in the next Subsec. 5.2.

$$N_i(t) = \sum_{\ell=1}^{L} \sum_{m=1}^{M} E_{i\ell m} \cos(\omega t - \boldsymbol{k}_{i\ell m} \cdot \boldsymbol{r}_i + \theta_{i\ell m}) \tag{21}$$

where $E_{i\ell m}$, $\boldsymbol{k}_{i\ell m}$, and $\theta_{i\ell m}$ are electric field intensity, wave number vector, and phase shift of the noise from the noise sources (ℓ, m); and L and M are maximum number of noise sources, respectively, for the noise sources meshes ℓ and m. Then, Eq. (20) is rewritten as,

$$\begin{aligned} I_{ij}(t) = \frac{1}{T} \int_t^{t+T} \Bigg\{ & \sum_{\ell=1}^{L} \sum_{m=1}^{M} \sum_{\alpha=1}^{L} \sum_{\beta=1}^{M} E_{i\ell m} E_{j\alpha\beta} \\ & \cdot \cos(\omega t - \boldsymbol{k}_{\ell m} \cdot \boldsymbol{r}_i + \theta_{i\ell m}) \\ & \cdot \cos(\omega t - \boldsymbol{k}_{\alpha\beta} \cdot \boldsymbol{r}_j + \theta_{j\alpha\beta}) \\ & + \sum_{\ell=1}^{L} \sum_{m=1}^{M} E_{i\ell m} S_{j0} \\ & \cdot \cos(\omega t - \boldsymbol{k}_{i\ell m} \cdot \boldsymbol{r}_i + \theta_{i\ell m}) \\ & \cdot \cos(\omega t - \boldsymbol{k}_S \cdot \boldsymbol{r}_j + \theta_{jS}) \\ & + \sum_{\ell=1}^{L} \sum_{m=1}^{M} E_{j\ell m} S_{i0} \\ & \cdot \cos(\omega t - \boldsymbol{k}_{j\ell m} \cdot \boldsymbol{r}_j + \theta_{j\ell m}) \\ & \cdot \cos(\omega t - \boldsymbol{k}_S \cdot \boldsymbol{r}_i + \theta_{iS}) \\ & + S_{i0} S_{j0} \cos(\omega t - \boldsymbol{k}_S \cdot \boldsymbol{r}_i + \theta_{iS}) \\ & \cdot \cos(\omega t - \boldsymbol{k}_S \cdot \boldsymbol{r}_j + \theta_{jS}) \Bigg\} dt, \end{aligned} \tag{22}$$

for a time interval T that is sufficiently longer than $2\pi/\omega$ and sufficiently shorter than the characteristic times of phase variation of $\boldsymbol{k}_S \cdot (\boldsymbol{r}_i - \boldsymbol{r}_j)$ due to time passage caused by the Earth's rotation. Following general relationships (see Appendix C, for details) Eq. (19) that contains the contents of Eqs. (20) to (22) is rewritten as

$$\begin{aligned} & \langle D_i(\omega, t) \cdot D_j(\omega, t) \rangle \\ & \quad = \frac{1}{2} \sum_{\ell=1}^{L} \sum_{m=1}^{M} E_{\ell m}^2(t) \cos[\boldsymbol{k}_{\ell m}(\boldsymbol{r}_j - \boldsymbol{r}_i) + (\theta_i - \theta_j)] \\ & \qquad + \frac{1}{2} S_0^2(t) \cos[\boldsymbol{k}_S(\boldsymbol{r}_j - \boldsymbol{r}_i) + (\theta_i - \theta_j)]. \end{aligned} \tag{23}$$

To have Eq. (23), it is assumed that pulse forms arriving at observation stations, where the same beam characteristic of the primary antenna is set, are the same as $S_{i0}(t) = S_{j0}(t) = S_0(t)$.; and it is also assumed that $E_{i\ell m}^2(t) = E_{j\ell m}^2(t) = E_{\ell m}^2(t)$. The last term in Eq. (23) shows the time dependent effect $\cos[\boldsymbol{k}_S(\boldsymbol{r}_j - \boldsymbol{r}_i) + (\theta_i - \theta_j)]$, on the observed data S_0^2; that is, the interferometer function between data from i-th and j-th sations. The function $\cos[\boldsymbol{k}_S(\boldsymbol{r}_j - \boldsymbol{r}_i) + (\theta_i - \theta_j)]$ is called the fringe function of the interferometer in this paper (FFI hereafter); the time series of FFI is called FFI data also in the present study.

5.2 IFFCM for the Detection of the Source Direction

5.2.1 Processes in time domain

a. Basic principle

In this IFFCM, we utilize the earth rotation for source finding as one of known method of the aperture synthesis in the interferometer observation (see Appendix D for equivalence of the present approach to the orthodox interferometer observation using the earth rotation). In the orthodox interferometer observation, however, it is essential to calibrate the system phase shift $\theta_i - \theta_j$ (see Eq. (23)) but we treat this phase shift in the system as unknown parameters. Then as the first step in finding the direction of the source, we generate two

doi:10.5047/978-4-88704-171-4

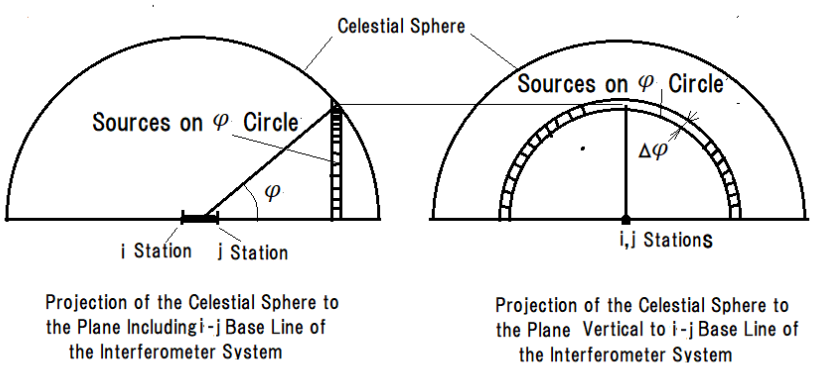

Fig. 5. Celestial sphere to describe the noise sources that are homogeneously distributed in whole direction in the sky. The sources are assigned to the unit cells which are defined along the circular belts on the celestial sphere surface located in the direction of angle $\varphi = m\pi/1800$ with respect to $\boldsymbol{r}_j - \boldsymbol{r}_i$ baseline of the interferometer; the circular belt with angle width of 0.1° divided to form the cell with angle width of 0.1° in the direction along the circular belt. The numbers m and ℓ are labels of the circular belts and the label of the cells along the circular belts, respectively that are given in Eqs. (22) and (23) and in equations following these in main text.

template functions of the FFI corresponding to search direction of the target source. That is, the template FFI functions C_{pij} and S_{pij} are prepared for operation of the i-j baseline of the interferometer as

$$C_{pij} = \cos[\boldsymbol{k}_p(\boldsymbol{r}_j - \boldsymbol{r}_i)], \tag{24}$$

and

$$S_{pij} = \sin[\boldsymbol{k}_p(\boldsymbol{r}_j - \boldsymbol{r}_i)], \tag{25}$$

where $\boldsymbol{k}_p$ is the wave number vector prepared to search for the target source. By applying this template FFI to Eq. (23) then, we can obtain a fringe correlation function $C_{ij}(t_n)$ and $S_{ij}(t_n)$ to find the signals which include the pulse components as,

$$\begin{aligned} C_{ij}(t_n) = \frac{1}{2T_F}\int_{t_n}^{t_n+T_F} & \cdot \left\{ \sum_{\ell=1}^{L}\sum_{m=1}^{M} E_{\ell m}^2(t)\cos[\boldsymbol{k}_{\ell m}(\boldsymbol{r}_j - \boldsymbol{r}_i) + (\theta_i - \theta_j)] \right. \\ & \left. + S_0^2(t)\cos[\boldsymbol{k}_S(\boldsymbol{r}_j - \boldsymbol{r}_i) + (\theta_i - \theta_j)] \right\} \\ & \cdot \cos[\boldsymbol{k}_p(\boldsymbol{r}_j - \boldsymbol{r}_i)]dt, \end{aligned} \tag{26}$$

and

$$\begin{aligned} S_{ij}(t_n) = \frac{1}{2T_F}\int_{t_n}^{t_n+T_F} & \cdot \left\{ \sum_{\ell=1}^{L}\sum_{m=1}^{M} E_{\ell m}^2(t)\cos[\boldsymbol{k}_{\ell m}(\boldsymbol{r}_j - \boldsymbol{r}_i) + (\theta_i - \theta_j)] \right. \\ & \left. + S_0^2(t)\cos[\boldsymbol{k}_S(\boldsymbol{r}_j - \boldsymbol{r}_i) + (\theta_i - \theta_j)] \right\} \\ & \cdot \sin[\boldsymbol{k}_p(\boldsymbol{r}_j - \boldsymbol{r}_i)]dt \end{aligned} \tag{27}$$

where t_n is n-th timing of the discretely defined time series data.

In the present approach of the interferometer to find the source direction by utilizing the earth's rotation, the time dependent variation of the sources in the sky due to the earth's rotation $\boldsymbol{k}_{\ell m}(\boldsymbol{r}_j - \boldsymbol{r}_i)$ and $\boldsymbol{k}_S(\boldsymbol{r}_j - \boldsymbol{r}_i)$ are significant functions. We introduce here an angle φ_{Sij} corresponding to Eqs. (26) and (27), as,

$$\boldsymbol{k}_\xi(\boldsymbol{r}_j - \boldsymbol{r}_i) = \frac{2\pi\,|\boldsymbol{r}_j - \boldsymbol{r}_i|}{\lambda}\cos\varphi_{\xi ij}, \qquad (\xi = \ell m \text{ and } S) \tag{28}$$

where λ is the wavelength of the observing decameter radio wave.

The noise components in above Eqs. (26) and (27) are expressed as ensemble of noises from sources which are distributed in whole sky by assuming homogeneous distribution on the celestial sphere with homogeneous intensity level in forms of approximated small square cells of noise sources located in the direction corresponding to sky at (ℓ, m); ℓ, and m are numbers to express the location of cells as has been defined in Fig. 5 (see the caption for detail definition). There is an exceptional cell S where the signal source of the Galaxy center is located; in this cell, the noise intensity is also specially defined to meet with the observational results of S/N ratio. The cell size is selected to be resolution limit of the interferometer of present usage of the correlation method (IFFCM) to detect the source direction which is utilizing the earth's rotation; the resolution limit is about 0.1 degree as will be given in the next sub section. By taking expansion range of the sky to be 180 degree × 180 degree along circles running from south horizon to the north horizon and the east horizon to the west horizon, on the celestial sphere, passing through the apex looked from the center of the base line $(\boldsymbol{r}_j - \boldsymbol{r}_i)$. The set of numbers (ℓ, m) to identify the cell position on the celestial sphere is defined starting from $(1, 1)$ i.e., $m = 1$ and $\ell = 1$ for the cell at the east ward horizon in the direction of the base line vector $\boldsymbol{r}_j - \boldsymbol{r}_i$; the number m is defined on the circular belts with width of 0.1 degree whose direction with respect to the base line $\boldsymbol{r}_j - \boldsymbol{r}_i$ take an-

doi:10.5047/978-4-88704-171-4

gle $\varphi_{\ell mij} = \ell\pi/1800$ radian (see Fig. 5). The number M_φ of the cells on these circular belts are then counted as

$$M_\varphi = \frac{\pi \cdot \sin\varphi_{\ell mij}}{(\pi/1800)} = 1800\sin\varphi_{\ell mij}. \tag{29}$$

The total number M_T of the noise source cells distributed on the celestial sphere are, then, given by

$$\begin{aligned} M_T &= \int_0^\pi 1800\sin\varphi_{\ell mij}\left(\frac{d\varphi_{\ell mij}}{(\pi/1800)}\right) \\ &= (1800)^2\cdot\frac{2}{\pi}. \end{aligned} \tag{30}$$

The average value of noise levels from the source cells in the same circular belt, with angle $\varphi_{\ell mij}$ with respect to the baseline $\boldsymbol{r}_j - \boldsymbol{r}_i$ are simply proportional to the number of cells: then we count only the number of the circular belts taking M_φ as weighting function which is assigned to circular belt ℓ, because there is no phase mixing effect between the noises sources on the circular belt caused by the interferometer function ($\varphi_{\ell mij}$ = constant, for given ℓ). Therefore the maximum number L for accumulation of noise source given in Eqs. (26) and (27) is given by

$$L = \int_0^\pi \left(\frac{d\varphi_{\ell mij}}{(\pi/1800)}\right) = 1800. \tag{31}$$

Therefore, $E_\ell^2(t)$ is newly defined as

$$\sum_{\ell=1}^{L}\sum_{m=1}^{M_\varphi} E_{\ell m}^2(t) = \sum_{\ell=1}^{L} E_\ell^2(t). \tag{32}$$

Further, let's define a time dependent function $\Phi_{\xi ij}(t)$ corresponding to time dependent variation of $\varphi_{\xi ij}$ in Eq. (28) as

$$\Phi_{\xi ij}(t) = \frac{2\pi|\boldsymbol{r}_j - \boldsymbol{r}_j|}{\lambda}\cos\varphi_{\xi ij}. \tag{33}$$

After several steps of mathematical manipulations, Eqs. (26) and (27) are rewritten (by writing $\Phi_{\xi ij}(t) = \Phi_{\xi ij}$), for a situation where searching direction P is set close to the source direction S with expression, $\Phi_{Pij} = \Phi_{Sij} - \Delta\Phi_{Pij}$ for small deviation angle $\Delta\Phi_{Pij}$, as

$$\begin{aligned} C_{ij}(t_n) = \frac{1}{4T_F}\int_{t_n}^{t_n+T_F} & \cdot\left\{\sum_{\ell=1}^{L} E_\ell^2(t)[\cos(\Phi_{\ell ij}+\Phi_{Sij}-\Delta\Phi_{Pij})\right. \\ &+\cos(\Phi_{\ell ij}-\Phi_{Sij}+\Delta\Phi_{Pij})]\cos\theta_{ij} \\ &-\sum_{\ell=1}^{L} E_\ell^2(t)[\sin(\Phi_{\ell ij}+\Phi_{Sij}-\Delta\Phi_{Pij}) \\ &+\sin(\Phi_{\ell ij}-\Phi_{Sij}+\Delta\Phi_{Pij})]\sin\theta_{ij} \\ &+S_0^2(t)[\cos(2\Phi_{Sij}-\Delta\Phi_{Pij}) \\ &+\cos(\Delta\Phi_{Pij})]\cos\theta_{ij} \\ &-S_0^2(t)[\sin(2\Phi_{Sij}-\Delta\Phi_{Pij}) \\ &\left.+\sin(\Delta\Phi_{Pij})]\sin\theta_{ij}\right\}dt, \end{aligned} \tag{34}$$

and

$$\begin{aligned} S_{ij}(t_n) = \frac{1}{4T_F}\int_{t_n}^{t_n+T_F} & \cdot\left\{\sum_{\ell=1}^{L} E_\ell^2(t)[\sin(\Phi_{\ell ij}+\Phi_{Sij}-\Delta\Phi_{Pij})\right. \\ &+\sin(\Phi_{\ell ij}-\Phi_{Sij}+\Delta\Phi_{Pij})]\cos\theta_{ij} \\ &+\sum_{\ell=1}^{L} E_\ell^2(t)[\cos(\Phi_{\ell ij}+\Phi_{Sij}-\Delta\Phi_{Pij}) \\ &-\cos(\Phi_{\ell ij}-\Phi_{Sij}+\Delta\Phi_{Pij})]\sin\theta_{ij} \\ &+S_0^2(t)[\sin(2\Phi_{Sij}-\Delta\Phi_{Pij}) \\ &+\sin(\Delta\Phi_{Pij})]\cos\theta_{ij} \\ &+S_0^2(t)[\cos(2\Phi_{Sij}-\Delta\Phi_{Pij}) \\ &\left.-\cos(\Delta\Phi_{Pij})]\sin\theta_{ij}\right\}dt \end{aligned} \tag{35}$$

where T_F is integration interval; and $\theta_{ij} = \theta_i - \theta_j$.

With respect to signal component associated with $S_0^2(t)$ in Eqs. (34) and (35), the integration of the functions $\cos[2\Phi_{Pij}(t) - \Delta\Phi_{Pij}]$ and $\sin[2\Phi_{Pij}(t) - \Delta\Phi_{Pij}]$ by the time t becomes a key issue to achieve the accurate interferometer correlation function to identify the source direction. When we describe these integrations by picking up from Eqs. (34) and (35), the results are given by

$$\begin{aligned} &\frac{1}{4T_F}\int_{t_n}^{t_n+T_F}\cos[2\Phi_{Pij}(t)-\Delta\Phi_{Pij}]dt \\ &\quad\approx \frac{[-\sin[2\Phi_{Pij}(t)]]_{t_n}^{t_n+T_F}}{8T_F\left\{\frac{2\pi|\boldsymbol{r}_j-\boldsymbol{r}_i|}{\lambda}\sin(\varphi_{Pij})\frac{d\varphi_{Pij}}{dt}\right\}}, \end{aligned} \tag{36}$$

and

$$\begin{aligned} &\frac{1}{4T_F}\int_{t_n}^{t_n+T_F}\sin[2\Phi_{Pij}(t)-\Delta\Phi_{Pij}]dt \\ &\quad\approx \frac{[\cos[2\Phi_{Pij}(t)]]_{t_n}^{t_n+T_F}}{8T_F\left\{\frac{2\pi|\boldsymbol{r}_j-\boldsymbol{r}_i|}{\lambda}\sin(\varphi_{Pij})\frac{d\varphi_{Pij}}{dt}\right\}}. \end{aligned} \tag{37}$$

Both in Eqs. (36) and (37), the term $D = \{(2\pi|\boldsymbol{r}_j - \boldsymbol{r}_i|/\lambda)\sin(\varphi_{Pij})(d\varphi_{Pij}/dt)$ in the denominator of the right hand side of equations shows values 3.52, 3.176, and 1.78 for Y-Z, Ka-Z, and Y-Ka base lines respectively (Y: Yoneyama, Z: Zao and Ka: Kawatabi Station), for approximated calculation where $\sin(\varphi_{Pij}) \approx 1$. Because the absolute value of numerators in the right hand side of Eqs. (36) and (37) take values equal or less than unity, we have an approximated results, for the signal component in Eqs. (34) and (35), using a form to express the order of the magnitude $O(\,)$ as,

$$\begin{aligned} &\frac{1}{2T_F}\int_{t_n}^{t_n+T_F}\cos[2\Phi_{Pij}(t)-\Delta\Phi_{Pij}]dt \\ &\quad= O\left(\frac{1}{3T_F}\right)\sim O\left(\frac{1}{8T_F}\right), \end{aligned} \tag{38}$$

doi:10.5047/978-4-88704-171-4

and

$$\frac{1}{2T_F}\int_{t_n}^{t_n+T_F}\sin[2\Phi_{Pij}(t)-\Delta\Phi_{Pij}]dt = O\left(\frac{1}{3T_F}\right)\sim O\left(\frac{1}{8T_F}\right). \quad (39)$$

b. Reduction processes of sky noises

Lets here investigate the noise components led by the term $E_\ell^2(t)$ in Eqs. (34) and (35). Through out this processes we can consider that $\Phi_{\ell ij}+\Phi_{Sij}-\Delta\Phi_{Pij}\approx\Phi_{\ell ij}+\Phi_{Sij}$ and $\Phi_{\ell ij}-\Phi_{Sij}+\Delta\Phi_{Pij}\approx\Phi_{\ell ij}-\Phi_{Sij}$ because effects of $\Delta\Phi_{Pij}$ is negligible except for the case of $\ell=S$ exactly. For convenience of expression we introduce the integration that is given by

$$K(A,B,C) = \frac{1}{4T_F}\int_{t_n}^{t_n+T_F} \cdot\left\{\sum_{\ell=1}^{L}E_\ell^2(t)\left[\cos\left(\Phi_{\ell ij}+A\Phi_{Sij}+B\frac{\pi}{2}\right)\cdot C\right]\right\}dt \quad (40)$$

where A, B and C are constant parameters to represent all of corresponding terms in Eqs. (34) and (35).

When we investigate the difference of phase angle between the, n-th and $(n+1)$-th circular belts, i.e., $(\Phi_{n+1ij}+A\Phi_{Sij})-(\Phi_{nij}+A\Phi_{Sij})$ relating to Eq. (33) for the noise sources distributed in the celestial sphere as given in Fig. 5, it is given that

$$(\Phi_{n+1ij}+A\Phi_{Sij})-(\Phi_{nij}+A\Phi_{Sij}) = \Phi_{n+1ij}(t)-\Phi_{nij}(t) = \frac{2\pi|\boldsymbol{r}_j-\boldsymbol{r}_i|}{\lambda}\sin\varphi_{nij}\cdot\Delta\varphi \quad (41)$$

where $\Delta\varphi=\varphi_{n+1ij}-\varphi_{nij}$.

When the interferometer baseline Y-Z with distance of 83 km is selected as an example, for the noise sources distributed with separation of 0.1 degree, i.e. $\Delta\varphi=0.1\times(\pi/180)rad$, then, it follows from Eq. (41) that

$$\Phi_{n+1ij}(t)-\Phi_{nij}(t) = 2\pi\times\frac{83000}{13.72}\times\sin\varphi_{ijn}\cdot\frac{\pi}{1800} \approx 21\pi\cdot\sin\varphi_{nij}. \quad (42)$$

In the case of the observation of the decameter radio wave, the total sky noise expressed by the relative level is in a range from 300 to 500 versus signal level which is defined to be unity. Then to estimate $K(A,B,C)$ given by Eq. (40), we can assign relative noise level as proportional to the cell number, on the celestial sphere, which gives $(300\cdot\sin\varphi_{\ell mij}/1.1\times10^3)$ to $(500\cdot\sin\varphi_{\ell mij}/1.1\times10^3)$ (see Eqs. (29) and (30) for $M_\varphi=1800\cdot\sin\varphi_{\ell mij}$ and $M_T=2.06\times10^6$) to $E_\ell^2(t)$ corresponding to circular belts ℓ. Again the homogeneous distribution of noise intensity for 2.06×10^6 cells of noise sources is assumed in the celestial sphere, here. Then, for accumulation of terms with $E_\ell^2(t)\cos(\Phi_{\ell ij}+A\Phi_{Sij})$ and $E_\ell^2(t)\sin(\Phi_{\ell ij}+A\Phi_{Sij})$ from $\ell=1$ to $\ell=L=1800$ (see Eq. (31)), we can expect that the results become close to 0 due to phase mixing that is endorsed by Eq. (42), in the processes of accumulation.

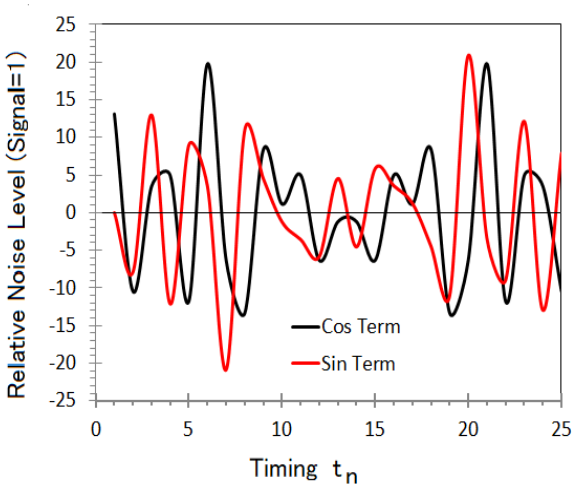

Fig. 6. Example of the accumulation of the sky noise as function of timing $t=t_n$ for $E_\ell^2(t)\cos(\Phi_{\ell ij}+A\Phi_{Sij})$ (black curve) and $E_\ell^2(t)\sin(\Phi_{\ell ij}+A\Phi_{Sij})$ (red curve) relating to Eq. (28). We can see that averaging of these noise terms tend to zero for integration in an interval $t=t_1\sim t_{25}$ due to the phase mixing of the sinusoidal functions.

For an example, we have calculated $E_\ell^2(t)\cos(\Phi_{\ell ij}+A\Phi_{Sij})$ and $E_\ell^2(t)\sin(\Phi_{\ell ij}+A\Phi_{Sij}+\pi/2)$ to estimate $K(A,B,C)$ for a model case of Yoneyama-Zao baseline where $\varphi_{Sij}=\pi/2$ or close to this period of time, following above described numerical situation. As has been indicated by results in Fig. 6, accumulations of noise term from $\ell=1$ to $M=1800$ vary depending on the timing though the averages for $T_F=25$ sec become almost 0 (-6.02×10^{-3} for cosine term and -1.00×10^{-12} for sine term); the deviations, at each timing of t_n, is 9.45 (relative level for signal level = 1) in term of the equivalent standard deviation.

The special case where $\ell=S$ appears for $A=-1$ in Eq. (40); that is

$$K(-1,B,C) = \frac{1}{4T_F}\int_{t_n}^{t_n+T_F} \cdot\left\{\sum_{\ell=S+1}^{L}E_\ell^2(t)\left[\cos\left(\Phi_{\ell ij}-\Phi_{Sij}+B\frac{\pi}{2}\right)\cdot C\right] + \sum_{\ell=1}^{S-1}E_\ell^2(t)\left[\cos\left(\Phi_{\ell ij}-\Phi_{Sij}+B\frac{\pi}{2}\right)\cdot C\right] + E_S^2(t)\left[\cos\left(\Delta\Phi_{Pij}+B\frac{\pi}{2}\right)\cdot C\right]\right\}dt, \quad (43)$$

where $\Delta\Phi_{Pij}=\Phi_{\ell ij}-\Phi_{Sij}$ for the case $\ell\cong S$. Thus starting from Eqs. (34) and (35) and taking above described steps of investigation, together with Eqs. (38) and (39) with consideration of the situation $\cos(\Delta\Phi_{Pij})\gg\sin(\Delta\Phi_{Pij})$, we arrive at the following expressions of $C_{ij}(t_n)$ and $S_{ij}(t_n)$

doi:10.5047/978-4-88704-171-4

as

$$C_{ij}(t_n) = \frac{1}{4T_F}\int_{t_n}^{t_n+T_F} E_S^2(t)\cos\Delta\Phi_{Pij}\cdot\cos\theta_{ij}dt + \frac{1}{4T_F}\int_{t_n}^{t_n+T_F} S_0^2(t)\cos\Delta\Phi_{Pij}\cos\theta_{ij}dt + O\left(\frac{1}{T_F}\right)S_0^2(t)[\cos\theta_{ij}-\sin\theta_{ij}], \quad (44)$$

and

$$S_{ij}(t_n) = -\frac{1}{4T_F}\int_{t_n}^{t_n+T_F} E_S^2(t)\cos\Delta\Phi_{Pij}\cdot\sin\theta_{ij}dt - \frac{1}{4T_F}\int_{t_n}^{t_n+T_F} S_0^2(t)\cos\Delta\Phi_{Pij}\sin\theta_{ij}dt + O\left(\frac{1}{T_F}\right)S_0^2(t)[\cos\theta_{ij}-\sin\theta_{ij}]. \quad (45)$$

5.2.2 Integration period and resolution of the direction finding of the signal sources

The selection of averaging time interval T_F in Eqs. (34) and (35) is made considering the two competing factors which decide the accuracy of the pulse forms $S_0^2(t)$ and resolution of the detecting source direction. That is, resolution of the detecting source direction $\Delta\phi$ is expressed by

$$\Delta\phi = \frac{d\varphi_{Sij}}{dt}\cdot T_F. \quad (46)$$

Because the source in the sky moves with the rate $15\pi/(6.48\times10^5)$ rad/sec, the resolution for detection of the direction becomes 0.00182 rad, i.e., 6 arc minutes while accuracy of the level decision becomes 4% in terms of error rate for the selection $T_F = 25$ sec in the present work. About capability of the direction finding by IFFCM method, confirmation will be given in Subsec. 6.2). It is also essential condition that $T_F \ll T_P$ for the characteristic period of the pulses T_P. In the present work, we are analyzing pulses with periods longer than 25 sec.

For this selection of the integration time T_F, Eqs. (34) and (35) are finally expressed by

$$C_{ij} = \frac{1}{4}[\overline{E_S^2(t_n)}\cos\Delta\Phi_{Pij} + S_0^2(t_n)\cos\Delta\Phi_{Pij}]\cos\theta_{ij} \quad (47)$$

and

$$S_{ij} = -\frac{1}{4}[\overline{E_S^2(t_n)}\cos\Delta\Phi_{Pij} + S_0^2(t_n)\cos\Delta\Phi_{Pij}]\sin\theta_{ij} \quad (48)$$

where $\overline{E_S^2(t_n)}$ is sky noise averaged over in an integration interval T_F for the sources from the direction of the semi-circular belt S in celestial sphere (see Fig. 5) which includes the signal source at the center part of our Galaxy; i.e., for Galaxy center with right ascension RA_{Gc} and declination Dec_{Gc}. At the interferometer baseline between i and j stations whose longitudes and latitudes are given as φ_i and λ_i for i-station and φ_j and λ_j for j-station the phase difference of the arriving radio wave between i and j stations are given using Earth's radius R_e as

$$\frac{2\pi}{\lambda}L_{ij}\cos\varphi_S = \frac{2\pi}{\lambda}R_e[\cos(\mathrm{RA}_{Gc})\cos(\mathrm{Dec}_{Gc})\cdot(\cos\varphi_i\cos\lambda_i-\cos\varphi_j\cos\lambda_j) + \sin(\mathrm{RA}_{Gc})\cos(\mathrm{Dec}_{Gc})\cdot(\sin\varphi_i\cos\lambda_i-\sin\varphi_j\cos\lambda_j) + \sin(\mathrm{Dec}_{Gc})(\sin\lambda_i-\sin\lambda_j)]. \quad (49)$$

In the semi-circular belts formed in the celestial sphere with angle radius $90^\circ\sin\varphi_S$ with width of 0.1° there are noises from $300\times1800\sin\varphi_S/(2.06\times10^6) = 0.262\sin\varphi_S$ to $500\times1800\sin\varphi_S/(2.06\times10^6) = 0.436\sin\varphi_S$ versus unity of the signal intensity. As it will be clarified in the next Sec, the noise intensity in this semi-circular belt much higher than this estimation; that is the observation results show that the noise level in this circular belt including Galaxy center is almost 25; it is suggested that the noise from the Galaxy center is 100 times larger than the background noise sources which are assumed to be homogeneous in the sky.

5.2.3 Final processes of data analyses in time domain

In the present study the time series data sampled at t_n is analyzed; because the sampling time is 1 sec ($t_{n+1}-t_n =$ 1 sec), the integration by $T_F = 25$ sec means that we are taking running average data starting from the original time series data. The time interval between t_n and t_{n+1} is selected to be short enough so that $S_0^2(t_n) \approx S_0^2(t_n+T_F)$ is insured not to deform the pulse during averageing process in Eqs. (47) and (48). Hereafter we use term of power for signal and noise as $P_S = S_0^2$ and $P_N(t_n) = \overline{E_S^2(t_n)}$. Then Eqs. (47) and (48) are rewritten as

$$C_{ij}(t_n) = \frac{1}{4}[P_N(t_n)+P_S(t_n)]\cos\Delta\Phi_{Pij}\cos\theta_{ij} \quad (50)$$

and

$$S_{ij}(t_n) = -\frac{1}{4}[P_N(t_n)+P_S(t_n)]\cos\Delta\Phi_{Pij}\sin\theta_{ij}. \quad (51)$$

From Eqs. (50) and (51) we form the time series data of the correlation function of fringe without depending to the ambiguity in phase, $\theta_{ij} = \theta_j - \theta_i$ as has been given below,

$$F_{ij}(t_n) = \sqrt{C_{ij}^2(t_n)+S_{ij}^2(t_n)}. \quad (52)$$

This expression is rewritten by

$$F_{ij}(t_n) = \frac{1}{4}[P_N^2(t_n)+2P_N(t_n)P_S(t_n)+P_S^2(t_n)]^{1/2}\cdot\cos\Delta\Phi_{Pij} = \frac{1}{4}[P_N(t_n)+P_S(t_n)]\cos\Delta\Phi_{Pij}. \quad (53)$$

doi:10.5047/978-4-88704-171-4

5.2.4 Processes in Fourier Transformed Domain

To search for the pulse components in the observed data we apply Fourier analyses starting for data series given by Eq. (53).

$$F_{\rm trans}(F_{ij}(t)) = \int_{-\infty}^{\infty} F_{ij}(t)e^{-i\omega t}dt \equiv F_{ij}^{T}(\omega), \qquad (54)$$

where $F_{\rm trans}(\ \ )$ denotes the operation of the Fourier transformation for a given time dependent function within the brackets. For the processes of the Fourier transformation the timing t_n at each second is approximated as to be continuous by expressing the data series as $F_{ij}(t)$. To be realistic for data analyses, we adopt FFT method with 512 data sampling, by selecting maximum interval of 8192 sec for Fourier transformation. For simplicity in these analyses we use only the absolute value of spectra without details of the phase of the Fourier transformed function. That is, for the time dependent function, the Fourier transformed function is expressed by absolute value $|F(\omega)|$ that is given by

$$|F_{ij}^{T}(\omega)| = \{[F_{R,ij}^{T}(\omega)]^2 + [F_{I,ij}^{T}(\omega)]^2\}^{1/2}, \qquad (55)$$

where $F_{R,ij}^{T}(\omega)$ and $F_{I,ij}^{T}(\omega)$ are the real and imaginary parts of $F_{ij}^{T}(\omega)$, respectively.

When we assume a completely random noise for the sky background, the Fourier transformed form is expressed by a constant function with respect to frequency that is usually called white noise; i.e., for a constant value $P_{\rm const}$, Fourier transformed noise $F_{N}^{T}(\omega)$ is given theoretically by using arbitrary function, $\theta_N(\omega)$ as

$$F_{\rm trans}(F_{Nij}(t)) \equiv F_{Nij}^{T}(\omega) = P_{\rm const}\cdot\exp[i\theta_N(\omega)], \qquad (56)$$

or

$$|F_{Nij}^{T}(\omega)| = P_{\rm const}. \qquad (57)$$

If we select the noise from the night sky without our Galaxy, the Fourier transformed function of the noise associated with correlation function of the interferometer fringe function to find the source direction is expressed by,

$$\begin{aligned} &F_{\rm trans}(P_N(t)\cos\Delta\Phi_{Pij}) \\ &\quad = F_{\rm trans}\left(P_N(t)\left[1-\frac{1}{2}(\Delta\Phi_{Pij})^2\right]\right) \\ &\quad = F_{Nij}^{T}(\omega)+\varepsilon(\omega), \end{aligned} \qquad (58)$$

where $\varepsilon(\omega)$ indicates the Fourier transformed function deviating from the white noise $F_{Nij}^{T}(\omega)$ due to organized modulation caused by the interferometer fringe together with stochastic deviation around the standard deviation; however, it should be noted that $|F_{Nij}^{T}(\omega)| \gg |\varepsilon(\omega)|$.

Using Eq. (54) then, the Fourier transformed expression of Eq. (53) is given by

$$\begin{aligned} &F_{\rm trans}\left(\frac{1}{4}[P_N(t)+P_S(t)]\cos\Delta\Phi_{Pij}\right) \\ &\quad = \frac{1}{4}\{P_{\rm const}\exp[i\theta_N(\omega)]+\varepsilon(\omega)+S(\omega)\cos\Delta\Phi_{Pij}\} \\ &\quad = \frac{1}{4}\{F_{Nij}^{T}(\omega)+\varepsilon(\omega)+S(\omega)\cos\Delta\Phi_{Pij}\}. \end{aligned} \qquad (59)$$

At this stage it becomes clear that for an observation data from a region of sky without the Galaxy center, we can apply the same interferometer fringe function, with that for the Galaxy center observation, that gives results corresponding to Eq. (59). The Fourier transformed function corresponding to Eq. (59), then, can be utilized without $S(\omega)$ as,

$$F_{\rm trans}(P_{NN}(t)) = F_{NNij}^{T}(\omega)+\varepsilon(\omega), \qquad (60)$$

where $P_{NN}(t)$ is interferometer data for radio waves from the sky without Galaxy center. Thus, the final form of Fourier transformed signals from the Galactic center are expressed by deriving from Eqs. (54) to (60) to obtain,

$$\begin{aligned} F_{\rm trans}(P_S(t)) &\equiv S(\omega)\cos\Delta\Phi_{Pij} \\ &= F_{\rm trans}([P_N(t)+P_S(t)]) \\ &\quad - F_{\rm trans}(P_{NN}(t)). \end{aligned} \qquad (61)$$

6. FFT ANALYSES OF OBSERVED DATA

FFT analyses have been conducted for the data that correspond to observation periods given in Tables 3 to 5 separated into the four groups which are indicated in the fourth column of the table as Average Group. In each group, the FFT results for the seven observation nights are averaged. FFT data analyses using Eq. (59) and other all related equations have been made for the periods of observation of the Galactic center. Using Eq. (60) and other all related equations, the FFT data analyses were made for the observations of the sky without the Galactic center that are given in Table 4. In this non-Galaxy case, the data for analyses are separated into two groups where the FFT results for the seven corresponding nights have been averaged to produce the Fourier transformed data.

The method of FFT analyses used for wide period ranges starting from the longest period of 8192 sec down to 40.96 sec corresponding to 1.22×10^{-4} Hz to 0.0244 Hz respectively. To analyze further more wide frequency range we define GS-n as the analyzing frequency range corresponding to the minimum frequency of $0.000122\times2^{10-n}$ Hz to the maximum frequency of $0.0244\times2^{10-n}$ Hz. The maximum analyzing periods of GS-n cover $8192\times(1/2)^{10-n}$ sec to the minimum period of $40.96\times(1/2)^{10-n}$ sec.

In the present work, we mainly use GS 10 for the time series of data setting corresponding to Eq. (53). The minimum requirement of the data number is 8192 for GS-10 analyses. Because the method applies a 512 point FFT for the present work, there are 16 independent data sets for analyses. For a five hour observation, i.e. 18000 sec of time series data, then we can find 32 sets of independent time series for the FFT analyses. As given in Table 6, data from three stations are divided into three independent channels with a center frequency of 900 Hz, 1000 Hz and 1100 Hz. The combinations to operate the interferometer function provide three pairs: Yoneyama vs Kawatabi, Yoneyama vs Zao, and Zao vs Kawatabi. So we have 288 ($=32\times3\times3$) independent time series of data also for FFT analyses. When we average over seven nights in each data series, then, it becomes possible to average the FFT results over 2016 (288×7) trials. The error

doi:10.5047/978-4-88704-171-4

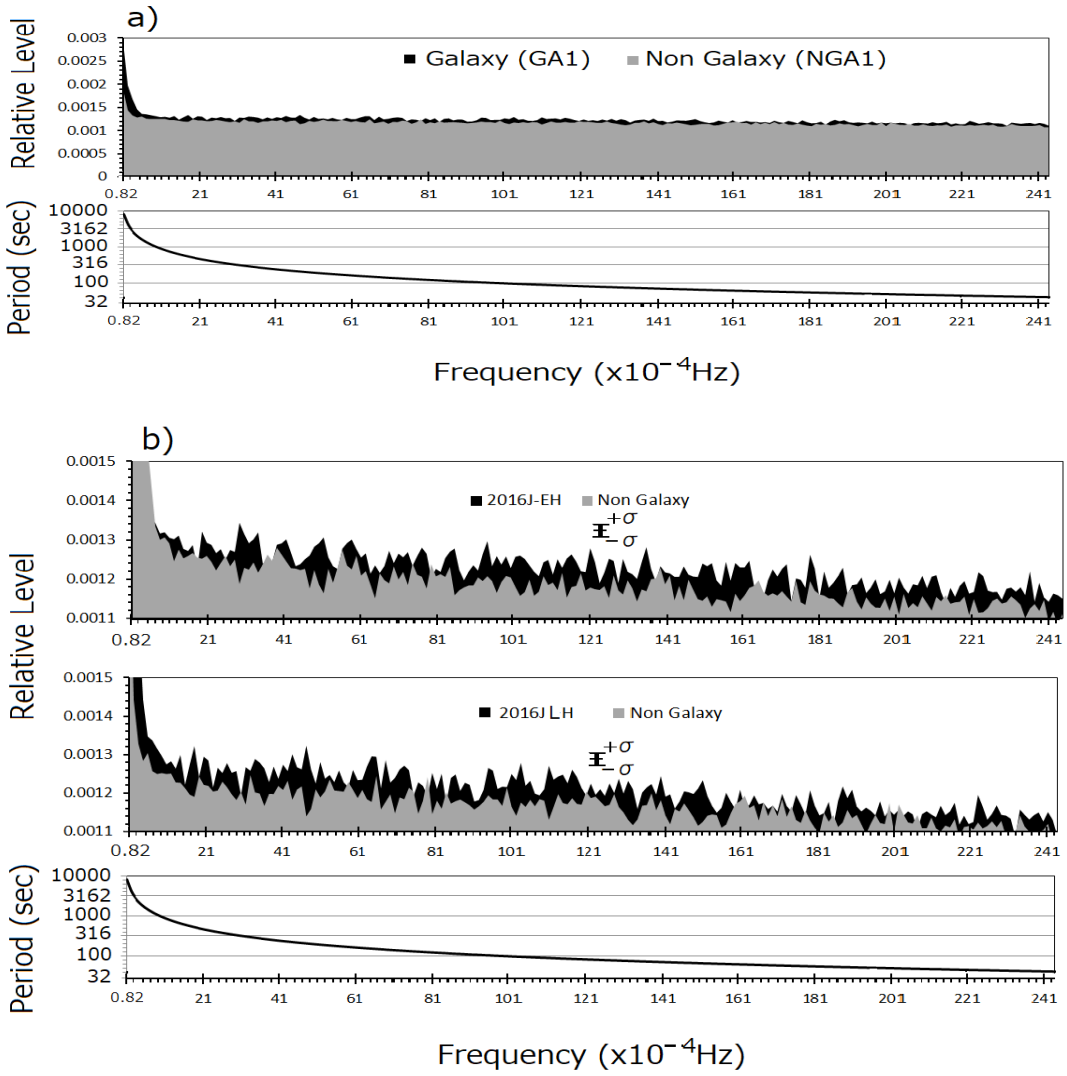

Fig. 7. (a) Results of Fourier transformation for the data group GA-1 (black spectra Labeled 2016 J-EH) together with results of the Fourier transformation for data NGA-1 (gray spectra) both averaged 2016 time trials of the FFT analyses corresponding to Eqs. (59) and (60). Abscissa indicates the linear frequency from 0.82×10^{-4} Hz to 241×10^{-4} Hz; a diagram of conversion of the frequencies to corresponding periods is given in the bottom panel. (b) Top panel: expanded display of two results of FFT analyses for GA-1 data series (black spectra) and for NGA-1 data series (gray spectra) in the relative level range from 1.1×10^{-3} to 1.5×10^{-3}, corresponding to panel (a), the mark σ in the panel is the standard deviation of the results of Fourier analyses thus suggesting that the peaks in the results show significant differences from the white noise level. Middle Panel: same as Top Panel of (b) for the cases of GA-2 (2016J-LH) data series (black spectra) together with NGA-2 data series (gray spectra). Bottom Panel: diagram of conversion of the frequencies to their corresponding periods.

rate for the final FFT in each data group (see Tables 3 to 5) is then 0.022 ($= 1/\sqrt{2016}$).

6.1 Results of observations in June 2016

The results of FFT analyses for data observed in June 2016 are indicated in Figs. 7(a) and 7(b) where the results for observation of sky with Galaxy center and observation of sky without Galaxy center (Non-Galaxy hereafter) are displayed with black and gray colors, respectively. Analyzing data are divided into an early half period (from June 5 to June 18) corresponding to data series GA1, (labeled 2016J-EH) and a late half period (from June 18 to June 30) corresponding to data series GA2 (labeled 2016J-LH) out of which we select seven nights as a data set to average for the calculated results. The averaged results of the FFT analyses are given being expanded for each data series in Fig. 7(b). As described in Subsec. 5.2.4, sky noise in Non Galaxy case is utilized as reference (reference noise data: RND hereafter); in the processes of analyzing data, these are modulated by the fringe function of the interferometer for detection of the source direction, as given by Eqs. (34) and (35) and other related equations including the noise term. To obtain spectra of RND corresponding to Eq. (60), for this case, we have used data observed from December 5 in 2016 to February 13, in 2017 dividing the data into two series to find averages of FFT results as NGA-1 and NGA-2 that are indicated in Table 4. By considering the standard deviations of averaged FFT results that have been described in the top part of the Sec. 5, and indicated in the diagrams given in Fig. 7(b), the peaks of

doi:10.5047/978-4-88704-171-4

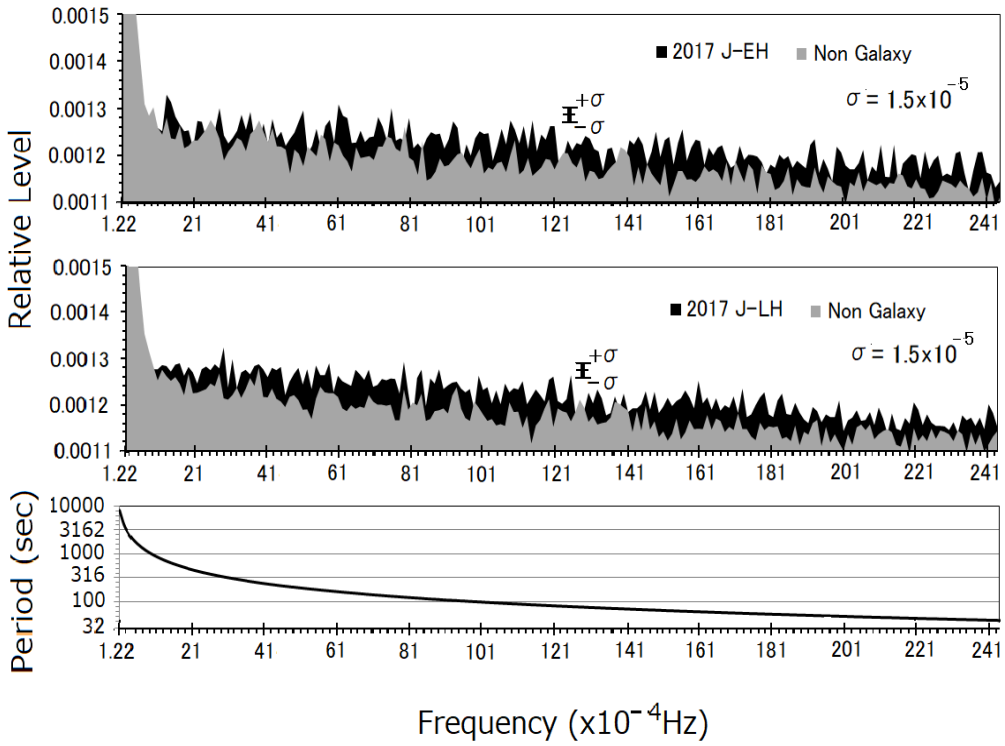

Fig. 8. Top Panel: the same as Fig. 7(b) for an expanded indication of the results of FFT analyses for the data group GA-3 (black spectra) together with results of FFT analyses for data NGA-1 (gray spectra). Middle Panel: same as Fig. 7(b) for an expanded indication of results of the FFT analyses for GA-4 data series (black spectra) with results for NGA-2 data series (gray spectra). Middle Panel: same as Fig. 7(b) for the cases of GA-4 data series (black spectra) and for NGA-2 data series (gray spectra). Bottom Panel: diagram of conversion of the frequencies to the corresponding periods.

variation of the resultant spectra contain significantly different component from the white noise signature from the sky.

6.2 Results of Observations in 2017

In Fig. 8 the results of FFT analyses are given for data observed in June and July, 2017 divided into an early half period (from June 7 to June 19, 2017J EH) corresponding to data series GA3, and a late half period (from June 19 to July 3) corresponding to data series GA4 out of which we have selected seven nights as a data set to average the calculated results. The averaged results of the FFT analyses are given for each data series in the top and the second panels of Fig. 8. The presentation of the results are the same as the presentation of the results for 2016 (see Figs. 7(a) and 7(b)). Galaxy spectra and RND to subtract the noise components spectra modulated by the fringe function are apparently different from the white noise component from the sky as it has been indicated by comparison with the standard deviation indicated in the diagram.

7. NET SPECTRA AND RECOVERY OF THE ORIGINAL PULSE FORM

7.1 Significance of Difference between Galaxy vs Non-Galaxy Data

First of all we should emphasize that the differences of levels of FFT results given in Figs. 7 and 8 for observation results, respectively 2016 and 2017 between observation results of non Galaxy cases in December 2016 and January 2017 are not the difference of the observation level, because all data are normalized to be the same level, but differences of the evidence whether the signals different from the random noise are included or not; the base of the arguments is here given as follows.

In both Galaxy and Non-Galaxy cases observed data are normalized to form basic data corresponding to Eq. (17) which is described as start point to explain procedure of the data analyses in the present paper. When we apply this expression in Eq. (17) both Galaxy observation and Non Galaxy observation cases the initial time series of data from interferometer operation $I_G(\omega, t_n)$ and $I_{NG}(\omega, t_n)$, respectively, are normalized as

$$D_G(\omega, t_m) = I_G(\omega, t_m) / \sqrt{\sum_{m=1}^{M_{TD}} I_G(\omega, t_m)^2 / M_{TD}}, \qquad (62)$$

and

$$D_{NG}(\omega, t_m) = I_{NG}(\omega, t_m) / \sqrt{\sum_{m=1}^{M_{TD}} I_{NG}(\omega, t_m)^2 / M_{TD}}, \quad (63)$$

where m is number of the data sampling; M_{TD} is total number of time series data in 5 hour observation for both Galaxy and Non Galaxy observations. When we trace the steps of the data analyses from Eq. (17) to Eq. (61), it is easily under-

doi:10.5047/978-4-88704-171-4

stood corresponding to Eq. (53), that,

$$[F_{ij}(t_n)]_G \approx [F_{ij}(t_n)]_{NG}, \tag{64}$$

where $[F_{ij}(t_n)]_G$ and $[F_{ij}(t_n)]_{NG}$ are $F_{ij}(t_n)$ values given by Eq. (53) for the case of the Galaxy observation and Non Galaxy observation, respectively. From Eq. (53) ($P_S(t_n) = 0$ for $[F_{ij}(t_n)]_{NG}$), therefore, it can be concluded that

$$[P_N(t_n)]_G + [P_S(t_n)\cos\Delta\Phi_{Pij}]_G \approx [P_N(t_n)]_{NG}. \tag{65}$$

Further we take the step of the FFT analyses relating to Eqs. (60) and (61). Then it follows that

$$[F^T_{Nij}(\omega) + \varepsilon(\omega)]_G + [S(\omega)\cos\Delta\Phi_{Pij}]_G \approx [F^T_{Nij}(\omega) + \varepsilon(\omega)]_{NG}. \tag{66}$$

It should be noticed that the FFT results for a unit periods of analyses for 8162 sec are approximately equal between the case of Galaxy and Non Galaxy observations. The difference revealed in the results given in Figs. 7 and 8 are then not the differences of the level of the detected noise and signal intensity but the difference of the results caused by the difference of the statistic characteristics of the noise and signal.

As has already been described, we take average of the FFT results over 2016 (288×7) trials, to have the results given in Figs. 7 and 8; that is,

$$FFT_G = \frac{1}{2016}\sum_{m=1}^{2016}\{[F^T_{Nij}(\omega) + \varepsilon(\omega)]_{G,m} + [S(\omega)]_{G,m}\}, \tag{67}$$

for Galaxy observation and

$$FFT_{NG} = \frac{1}{2016}\sum_{m=1}^{2016}[F^T_{Nij}(\omega) + \varepsilon(\omega)]_{NG,m}, \tag{68}$$

for Non Galaxy observation. Because $F^T_{Nij}(\omega)$ is white noise, we can rewrite both for Galaxy and Non Galaxy observations as

$$\frac{1}{2016}\sum_{m=1}^{2016}\{[F^T_{Nij}(\omega) + \varepsilon(\omega)]_{G,m} + [S(\omega)\cos\Delta\Phi_{Pij}]_{G,m}\} = P_{G\,\mathrm{const}} + \Delta P_G(\omega) + \varepsilon(\omega) + [S(\omega)]_G, \tag{69}$$

$$\frac{1}{2016}\sum_{m=1}^{2016}[F^T_{Nij}(\omega) + \varepsilon(\omega)]_{NG,m} = P_{NG\,\mathrm{const}} + \Delta P_{NG}(\omega) + \varepsilon(\omega), \tag{70}$$

where $P_{G\,\mathrm{const}}$ and $P_{NG\,\mathrm{const}}$ are constant spectrum level for white noise both for Galaxy and Non Galaxy observation, respectively; $\Delta P_G(\omega)$ and $\Delta P_{NG}(\omega)$ are fluctuating component of noise spectra both for Galaxy and Non Galaxy observation, respectively. The level of the fluctuations are approximated as $\Delta P_G(\omega) \approx P_{G\,\mathrm{const}}/\sqrt{2016}$ and $\Delta P_{NG}(\omega) \approx P_{NG\,\mathrm{const}}/\sqrt{2016}$.

The FFT results in Figs. 7 and 8 indicate FFT_G results given by Eq. (69) are larger than FFT_{NG} results given by Eq. (70) by about $3\sigma P_{NG\,\mathrm{const}}$ (σ: standard deviation). From Eqs. (69) and (70), then, it follows that

$$P_{G\,\mathrm{const}} + \Delta P_G(\omega) + \varepsilon(\omega) + [S(\omega)\cos\Delta\Phi_{Pij}]_G = P_{NG\,\mathrm{const}}(1 + 3\sigma) + \Delta P_{NG}(\omega) + \varepsilon(\omega). \tag{71}$$

Further, Eq. (71) can be rewritten as.

$$[S(\omega)\cos\Delta\Phi_{Pij}]_G = 3\sigma P_{NG\,\mathrm{const}} + [P_{NG\,\mathrm{const}} + \Delta P_{NG}(\omega)] - [P_{G\,\mathrm{const}} + \Delta P_G(\omega)]. \tag{72}$$

As it is suggested by equations from Eq. (66) to Eq. (68) that

$$[P_{NG\,\mathrm{const}} + \Delta P_{NG}(\omega)] > [P_{G\,\mathrm{const}} + \Delta P_G(\omega)]. \tag{73}$$

We can state that there exist definitely signal components indicated by difference from the spectrum level which only consists of white noise with level of $P_{NG\,\mathrm{const}}$ showing level higher than 3σ as,

$$[S(\omega)]_G > 3\sigma P_{NG\,\mathrm{const}}. \tag{74}$$

7.2 Revisit the confirmation of the direction finding capability

As has been indicated by Eq. (61), final results of signal spectra are obtained in this fringe function correlation method, IFFCM (see Subsec. 2.2 for definition), in the form of $S(\omega)\cos\Delta\Phi_{Pij}$. When we consider background noises around signal source, we introduce an index that is defined, considering Eq. (74), as

$$\mathrm{Direc} = S(\omega)\cos\Delta\Phi_{Pij}/3\sigma P_{NG\,\mathrm{const}}, \tag{75}$$

This Direc value becomes significant; that is, if Direc $<$ 1, we cannot determine $\cos\Delta\Phi_{Pij}$, because the correlation function value buried within noise level. Considering this point, we have checked the capability of the direction finding by a simulation method following all equations in Sec. 5, by generating random number in the range from 0 to 1 as noise by multiplying factors to have necessary S/N ratio. In Fig. 9, results of the simulation are indicated for four example cases of S/N ratio; the minimum threshold of S/N ratio to make the present IFFCM method feasible is indicated to be 5/100. Application of IFFCM to real observation data will be described in Sec. 8 in detail.

7.3 Net signal spectra

Net signal spectra by subtracting RND spectrum from the resultant spectra of the Galaxy observation are given in Figs. 10 and 11. To subtract RND, for analyzing data observed in June 2016 and June 2017, the data observed from December 5, in 2016 to February 13, in 2017 are utilized by dividing them into two data series called NGA-1 and NGA-2 (see Subsec. 6.1). It should be noticed that even though we use the same noise data, RND is modulated by the identical fringe function that modulates the noise and signals of the corresponding nights when we aimed at the Galactic center.

In Fig. 10 the spectra that are resulting from the subtraction of the FFT results for NGA-1 from the FFT results for

doi:10.5047/978-4-88704-171-4

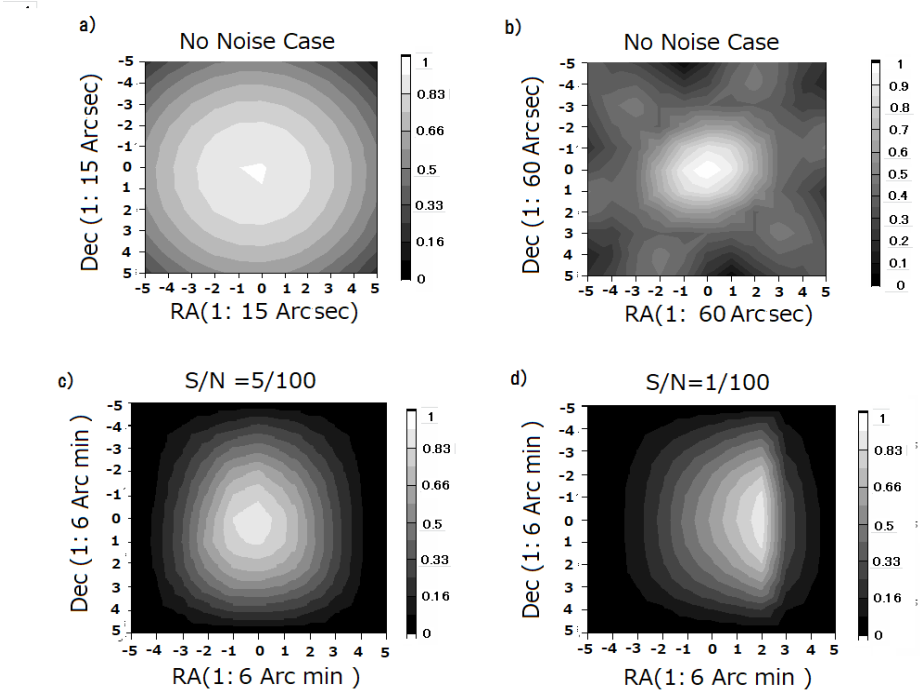

Fig. 9. Results of simulation analyses to verify the capability to find the source direction applying IFFCM. Results are indicated for a) the case of no noise with 15 arc sec directional mesh unit, b) the case of no noise with 60 arc sec directional mesh unit, c) the case with background noise of $S/N = 5/100$ and d) the case with background noise of $S/N = 1/100$. Relative levels of the fringe function correlation are indicated by gray codes whose calibrated values are indicated by column given at right hand side of each diagram. For simulation, test source is given at the center (0, 0) of each diagram. In the case of d), the source position is not identified correctly because noise level exceeds the threshold for accurate detection of the direction.

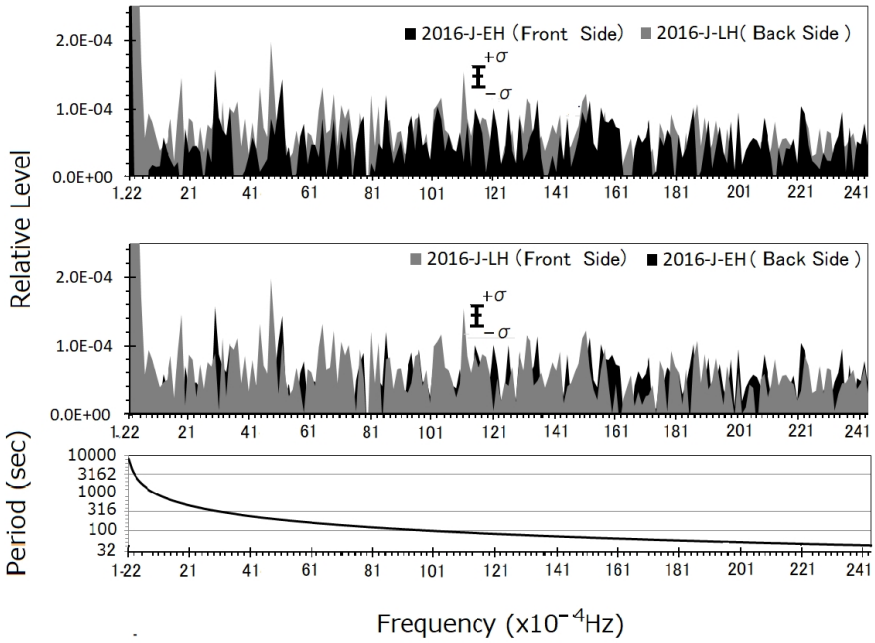

Fig. 10. Top Panel: the spectra resulting by subtracting the FFT results for NGA-1 from FFT results for GA1 (black spectra labeled as 2016 J-EH (Front Side)) and the spectra resulting by subtracting the FFT results for NGA-2 from FFT results GA-2 (gray spectra labeled as 2016 J-LH); the spectra 2016 J-EH are displayed in the front side of the top panel while the spectra 2016 J-LH are displayed in the front side of the middle panel to confirm the coincidence of the frequency of peaks in the spectra.

doi:10.5047/978-4-88704-171-4

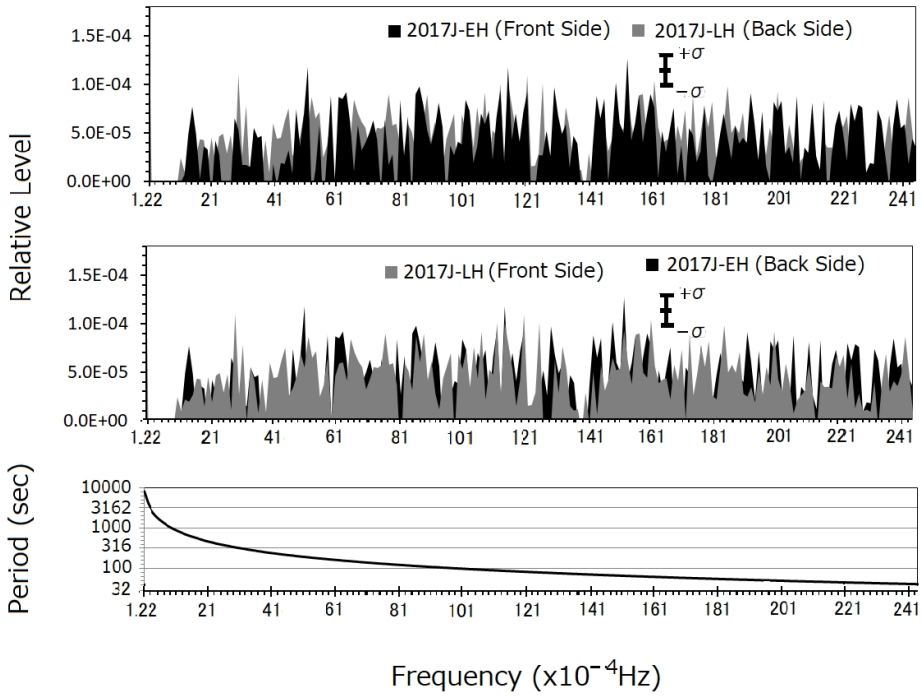

Fig. 11. Same with Fig. 9 for the net spectra Dif 2017-J-EH that is deduced by subtracting the FFT results for NGA-3 from the FFT results for GA-3 and for the net spectra Dif 2017-J-LH that is deduced by subtracting the FFT results for NGA-4 from the FFT results for GA-4.

GA1 (black spectra labeled as 2016-J-EH) and spectra that are resulting from subtraction of the FFT results for NGA-2 from the FFT results for GA-2 (gray spectra labeled as 2016-J-LH) are indicated both in the Top and Middle panels by changing the display order between the front and back sides. In Fig. 11 also, the resultant spectra by subtracting the FFT results for NGA-1 from the FFT results for GA3 (black spectra labeled as 2017-J-EH-) and the resultant spectra by subtracting the FFT results for NGA-2 from the FFT results for GA-4 (gray spectra labeled as 2017-J-LH) are displayed in both Top and Middle panels by changing the display order between the front and back sides.

By displaying two different results together, in both Figs. 10 and 11, we can investigate the coincidence of the frequency of peaks of the two spectra; we recognize that more than 80% of the frequency of peaks of corresponding spectra coincide but there are about 20% of the cases where we are not able to find a coincidence. As will be described in the next subsection Subsec. 7.4, the spectra that result from overlapping spectra of different origins are modified because the spectral peaks sometimes become spectral dips due to the combination of the underlying phases of spectra.

7.4 Criteria of the coincidence of FFT results

When we compare two FFT results for different observation data set for the same phenomenon which consist of complicated time varying functions, the two results for the peaks of the spectra at a given frequency do not necessarily coincide in all cases because of the overlapping of the spectra. We then estimate the criteria for coincidence of FFT results considering possible phase differences of overlapping spectra. We consider the case of overlap of two FFT results which consists of independent components. The FFT results basically have real and imaginary parts for the first spectra as $F_{1r}(\omega) = F_1(\omega)\cos\theta_1(\omega)$ and $F_{1i}(\omega) = F_1(\omega)\sin\theta_1(\omega)$ respectively; and for the second FFT results, $F_{2r}(\omega) = F_2(\omega)\cos\theta_2(\omega)$ and $F_{2i}(\omega) = F_2(\omega)\sin\theta_2(\omega)$ respectively. The absolute values of overlapping of the FFT function is then given by,

$$|F(\omega)| = \sqrt{F_1^2(\omega)+F_2^2(\omega)} \times \left[1+\frac{2F_1(\omega)F_2(\omega)}{F_1^2(\omega)+F_2^2(\omega)}\cos(\theta_1(\omega)-\theta_2(\omega))\right]^{1/2}. \quad (76)$$

In Fig. 12, $|F(\omega)|$ at a given ω are indicated for the overlapping of two independent spectra, assuming the same amplitude for all cases with assumed phase combinations that are randomly generated in phase range from 0 to 2π radians divided into 20 cases with a step of $\pi/10$. Because there are 20 kinds of selections for each phase, we can find 400 overlapping conditions for two overlapping spectra. We count the thresholds whether the overlapping of two peaks of FFT results makes dips without forming original peaks; the present calculation shows 127 combinations out of 400 total combination of phase values. When we compared the two FFT results associated with the possible overlapping of peaks of different components we may state, considering the above described statistics that the absolute value of the two FFT results are identical when more than 68% of peaks show the coincidence at the same frequency even if less than 32% of

doi:10.5047/978-4-88704-171-4

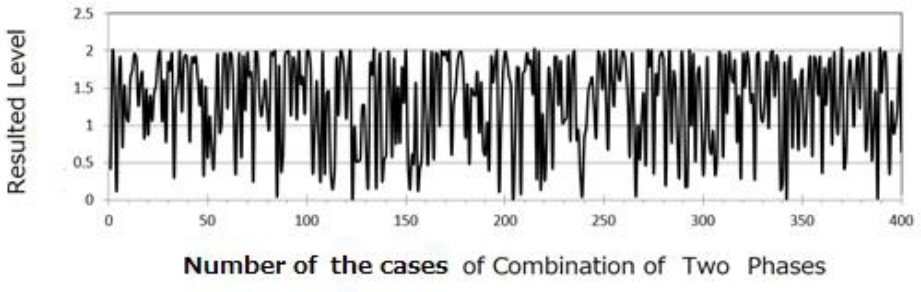

Fig. 12. Resulting level of the combination of FFT analyses for the case of the overlapping of two spectra with independent phase differences between the two spectra. The abscissa is number labelled for different combination cases of two phases, $\theta_1(\omega)$ and $\theta_2(\omega)$ in Eq. (76) between 20 kinds of different phases expressed by $(2\pi/20)m$ $(m = 1, 2, \ldots, 20)$ for $\theta_1(\omega)$ and expressed by $(2\pi/20)n$ $(n = 1, 2, \ldots, 20)$ for $\theta_2(\omega)$, i.e., the number of abscissa is given by $m \cdot n$. The maximum number of the combination is then 400.

peaks or dips indicate the opposite signature. Based on these criteria we can understand and state that the four net spectra resulting from data series GA1 vs NGA1, GA2 vs NGA2, GA3 vs NGA1 and GA4 vs NGA2 that are given in Figs. 10 and 11 are identical.

7.5 Recovery of Pulse Form by Applying Simulations

7.5.1 Process of Searching for Parameters of Binary Orbits from Side Bands Spectra

From the standpoint to find the pulse forms that indicate the spin of Kerr black holes in binary orbits, we recovered the pulse forms starting from the spectra of the FFT results. Instead of calculating the inverse Fourier transformation, we employed a simulation where we construct a pulse function whose FFT results match with the spectra obtained from the observation data. The FFT results given in Figs. 10 and 11 are characterized by a complicated distribution of spectral peaks covering a wide frequency range. These characteristics of the FFT results manifest multiple side bands that are caused by the frequency modulation on the spin periods of the two rotating objects; that is, the sinusoidal modulation on spin frequency due to Doppler effects of the orbital motion of the binary black holes.

By considering the Doppler effects due to the orbital motion whose geometrical feature is depicted in Fig. 13, we can describe the pulse of the radio wave emitted from a moving Kerr black hole for its intensity $E(t)$ as function of time t, as

$$E(t) = a_0 + \sum_{n=1}^{N} a_n \sin\left(\int_{t_0}^{t} n\omega_p dt + \varphi_n\right) \qquad (77)$$

where a_0, a_n and φ_n are fundamental levels of the pulse, amplitude of the n-th higher harmonics, and phase shift of the n-th higher harmonics, respectively; t_0 is an arbitrary selected starting time. Each harmonic is described with a sinusoidal function whose argument is expressed by the WKB approximation because the angular frequency $n\omega_p$ varies with time due to the Doppler effects caused by the orbital motion, as given by

$$n\omega_p = n\omega_{p0}(1 - \hat{\boldsymbol{k}} \cdot \boldsymbol{v}/c) \qquad (78)$$

where ω_{p0}, $\hat{\boldsymbol{k}}$, $\boldsymbol{v}$ and c are the original angular frequency of the spin of the Kerr black hole, the unit vector of the wave number vector of the radiated radio wave pulse directed towards the observation point, the orbiting velocity (see Fig. 13), and the velocity of light, respectively. Following the geometry of the orbiting source, $\hat{\boldsymbol{k}} \cdot \boldsymbol{v}$ is rewritten as:

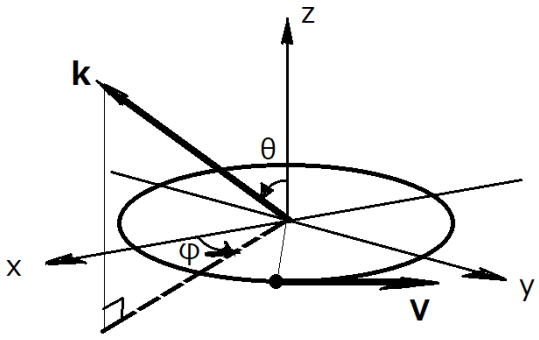

Fig. 13. Assumed circular orbit of a member of the binary black hole moving with velocity vector $\boldsymbol{v}$ in a plane whose normal direction in the z axis makes angle θ with wave number vector $\boldsymbol{k}$ directed toward the observation point. By considering the actual processes of the data analyses the orbital plane is described with Cartesian coordinate where two coordinates x and y are selected to be orthogonal with respect to z axis; the projection of $\boldsymbol{k}$ on the orbital plane makes angle φ with respect to the x axis.

$$\begin{aligned}\hat{\boldsymbol{k}} \cdot \boldsymbol{v} = & -v \sin\theta \cdot \cos\varphi \cdot \sin\Omega t \\ & + v \sin\theta \cdot \sin\varphi \cdot \cos\Omega t \end{aligned} \qquad (79)$$

where Ω is the angular frequency of the orbital motion. Using relations Eqs. (78) and (79), Eq. (77) is rewritten as

$$E(t) = a_0 + \sum_{n=1}^{N} a_n \sin[n\omega_{p0}t - K_n \cos(\Omega t - \varphi) + \Theta_n], \qquad (80)$$

where

$$K_n = \frac{n\omega_{p0}}{\Omega}\left(\frac{v}{c}\right)\sin\theta \qquad (81)$$

and

$$\Theta_n = n\omega_{p0}t_0 - K_n \cos(\Omega t_0 - \varphi) + \varphi_n.$$

doi:10.5047/978-4-88704-171-4

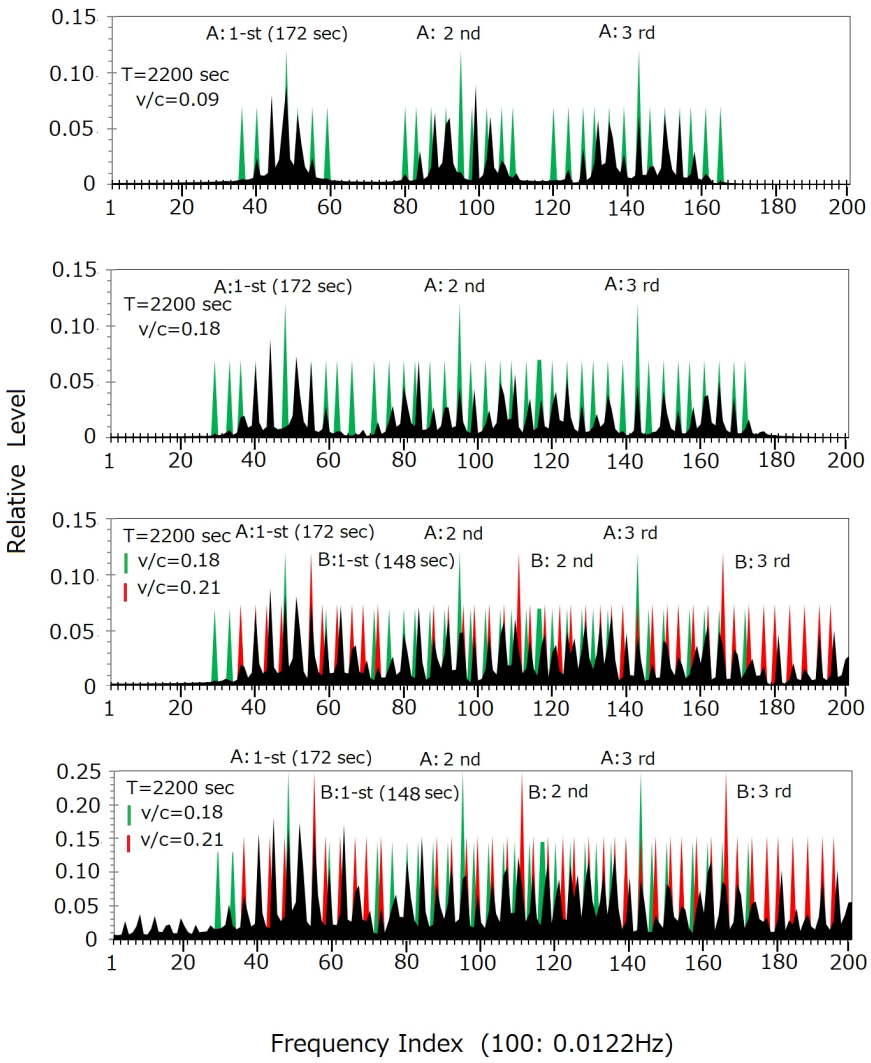

Fig. 14. The results of FFT analyses of the function corresponding to Eq. (82) (black spectra) with colored scales (green for signal from the source A; red for signal from the source B). The frequencies of possible sidebands for the 1st to 3rd corresponding harmonics given by Eq. (82) are indicated for an example case with an orbital period of 2200 sec. The top and second panels show the cases of the signal from the source A for orbital velocities 0.09 c and 0.18 c respectively (c: light velocity). The third panel shows the case where two signals from the sources A and B which have spin periods of 172 sec with orbital velocity 0.18 c and the spin period of 148 sec with orbital velocity 0.21 c respectively. The bottom panel shows the same case with the third panel where the objective function $E(t)$ is changed to $p(t) = [E(t)]^2$.

Then, Eq. (80) is expressed by ensemble of sinusoidal functions for harmonic oscillators associated with the multiple of side bands as,

$$\begin{aligned} E(t) = a_0 + \sum_{n=1}^{N} a_n [& [J_0(K_n)\sin(n\omega_{p0}t + \Theta_n) \\ & - J_1(K_n)\{\sin[(n\omega_{p0} + \Omega)t + \Theta_n] \\ & \quad + \sin[(n\omega_{p0} - \Omega)t + \Theta_n]\} \\ & - J_2(K_n)\{\sin[(n\omega_{p0} + 2\Omega)t + \Theta_n] \\ & \quad + \sin[(n\omega_{p0} - 2\Omega)t + \Theta_n]\} \\ & - J_3(K_n)\{\sin[(n\omega_{p0} + 3\Omega)t + \Theta_n] \\ & \quad + \sin[(n\omega_{p0} - 3\Omega)t + \Theta_n]\} \\ & - J_4(K_n)\{\sin[(n\omega_{p0} + 4\Omega)t + \Theta_n] \\ & \quad + \sin[(n\omega_{p0} - 4\Omega)t + \Theta_n]\} + \cdots]], \end{aligned} \tag{82}$$

where $J_0(K_n), J_1(K_n), \ldots \ldots J_4(K_n)$ are Bessel function of the first kind with order 0, 1, ...4, respectively. This result indicates that the n-th harmonics of the spectra are associated with side bands with frequency gaps of $\Omega/2\pi$ at frequencies $(n\omega_{p0} \pm m\Omega)/2\pi$ $(m = 1, 2, 3, \ldots)$ with amplitude of $a_n J_m(K_n)$, because of the orbital motion which causes the frequency modulation on the emitted pulse due to Doppler effects. Examples of sideband spectra due to frequency modulation are shown in Fig. 14 where a case of single signal with three harmonics and another case of two signals with three harmonics are displayed. In all panels in Fig. 14, the frequencies of the expected side band spectra are indicated with colored vertical bars; that is, green bar scales are for signal A whose fundamental frequency corresponds to the periods of 172 sec (tentatively selected), and red scales are for signal B whose fundamental frequency corresponds to the

doi:10.5047/978-4-88704-171-4

Table 7. Setting Values of Simulation Parameters for Periods and Orbiting Velocity.

Parameter	T_a	T_b	v_a/c	v_b/c
Value 1	172 sec	148 sec	0.16	0.19
Value 2	173 sec	149 sec	0.17	0.20
Value 3	174 sec	150 sec	0.18	0.21

Table 8. Setting Values of Simulation Parameters for Amplitudes of Harmonics.

Parameters	a_1	a_2	a_3	b_1	b_2	b_3
Value 1	1/3	1/3	1/3	1/3	1/3	1/3
Value 2	2/3	2/3	2/3	2/3	2/3	2/3
Value 3	1	1	1	1	1	1

period 148 sec (also tentatively selected). Because the observation signals are treated in the square form (see Eq. (47) vs Eq. (50) and Eq. (48) vs Eq. (51)), the results for squares of signal level are given in the bottom panel of Fig. 14; it can be seen that the square is not much modified peak frequency of spectra but the levels of spectra are expanded as much as two times.

7.5.2 Trial to Find Side Band in Observed Net Spectra

In Fig. 15 the net results of the FFT analyses for the data that are given in Figs. 8 and 9 are reproduced by applying the side band scales given in Fig. 14. The side band scales reflect the function given by Eq. (82) which confirm the possible signature of the orbital motion in the results of the decameter radio wave pulses from the Galactic center (DEPGC here after). In the bottom panel of Fig. 15, the average spectra of the four results of FFT analyses that correspond to data series GA1 (2016-J-EH), GA2 (2016-J-LH), GA3(2017-J-EH), and GA4 (2017-J-LH) are also indicated with the side band scales. Using this average FFT results we can confirm the certain recurrent nature of the occurrence of sideband spectra over entire periods of a half month and even further as long as a year. Because we have this evidence, we will select the average FFT result to investigate the characteristics of DEPGC. At this stage according to the bottom panel of Fig. 15, we can start the work for recovery of the original state with an orbital period (2200 ± 50) sec.

7.5.3 Finding simulation functions to coincide with the FFT results

After the investigations that have been described in Subsec. 7.5.1 and 7.5.2, the simulated function that describes the original wave form corresponding to detected electric fields is then given as,

$$\begin{aligned} E(t) = 1 &+ a_1 \cos\left[\omega_a t + \left(\frac{v_a}{c}\right)\frac{\omega_a}{\Omega}\sin(\Omega t) + \theta_{a1}\right] \\ &+ a_2 \cos\left[2\omega_a t + \left(\frac{v_a}{c}\right)\frac{2\omega_a}{\Omega}\sin(\Omega t) + \theta_{a2}\right] \\ &+ a_3 \cos\left[3\omega_a t + \left(\frac{v_a}{c}\right)\frac{3\omega_a}{\Omega}\sin(\Omega t) + \theta_{a3}\right] \\ &+ b_1 \cos\left[\omega_b t + \left(\frac{v_b}{c}\right)\frac{\omega_b}{\Omega}\sin(\Omega t) + \theta_{b1}\right] \\ &+ b_2 \cos\left[2\omega_b t + \left(\frac{v_b}{c}\right)\frac{2\omega_b}{\Omega}\sin(\Omega t) + \theta_{b2}\right] \\ &+ b_3 \cos\left[3\omega_b t + \left(\frac{v_b}{c}\right)\frac{3\omega_b}{\Omega}\sin(\Omega t) + \theta_{b3}\right] \end{aligned} \tag{83}$$

where $\Omega = 2\pi/T_{cm}$, $\omega_a = 2\pi/T_a$, and $\omega_b = 2\pi/T_b$, for orbiting period T_{cm}, the spin period of the first Kerr black hole T_a and the spin period of the second Kerr black hole T_b.

In the data analyses the interferometer operation is a basic step for that we cannot avoid to result the square of the field intensity (see Eq. (23)). The simulation tries to find matching parameters by constructing the original pulse forms $E(t)$ which are required to take the square of $E(t)$; i.e. $P_S(t)(= E(t)^2)$ provides the results that is expected to coincide with the FFT results for the observation data.

At this stage the sources which we have temporarily assumed as signals A and B in analyses to result Figs. 14 and 15 are considered to provide real parameters of sources at the binary system of the black holes by naming the first and second Kerr black holes as Gaa and Gab respectively. For the ensemble of harmonic oscillators corresponding to the radiation from Gaa and Gab, the harmonic numbers up to the 3rd harmonic are also assumed. The parameters given in Eq. (83) to construct the simulated pulse function, in addition to orbital period T_{cm}, the fundamental pulse periods T_a for Gaa, T_b for Gab, are the relative amplitude a_n and phase shift θ_{an} for n-th harmonic oscillator of Gaa pulse, and relative amplitude b_n with phase shift θ_{bn} for n-th harmonic oscillator of Gab pulse. Further, the orbital speeds of Gaa given by v_a/c and of Gab given by v_b/c are essential for calculating the Doppler effects caused by the orbital motion of the binary black holes. The formula for a simulation is constructed, then, with a total of 17 parameters which are searched through simulation processes.

In the total of 17 parameters, however, we consider six parameters which relate to the phases θ_{an} and θ_{bn} as unstable quantities which vary over the propagation paths. The phase values are therefore considered to have statistical significance. From this standpoint, we try to find

doi:10.5047/978-4-88704-171-4

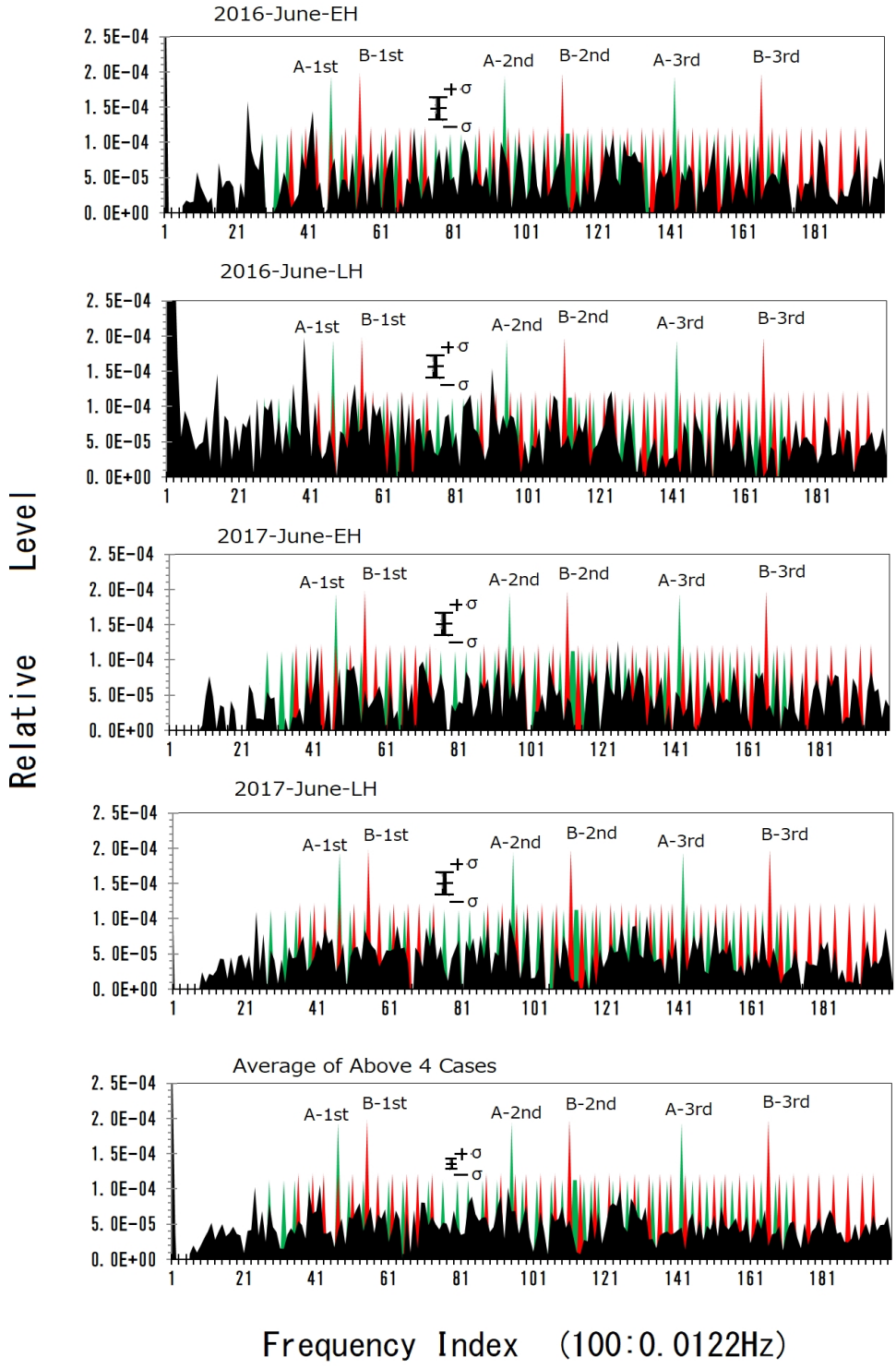

Fig. 15. Four cases of net results of the FFT analyses with frequency scales that are the same as the scales given in Fig. 14. The first four panels show the results for the observations, respectively for GA1(2016J EH), GA2(2016J LH), GA3(2017J EH), and GA4(2017J LH). The average results for these four cases are given in the bottom panel.

the statistical generation of sets of combinations for phases θ_{an} and θ_{bn} using the following procedure. That is, we set the step unit for variation of the phase value at $\pi/3$ radian; the setting phase values is made as $\theta_{an} = k_{an}(\pi/3)$ and $\theta_{bn} = k_{bn}(\pi/3)$. By selecting k_{an} and k_{bn} from a random series of numbers. We express, then, the combination of phase $(\theta_{a1}, \theta_{a2}, \theta_{a3}, \theta_{b1}, \theta_{b2}, \theta_{b3})$, by the form of $N(k_{a1}, k_{a2}, k_{a3}, k_{b1}, k_{b2}, k_{b3})$. The selection for construction of the simulation function is then made as $N1(4, 8, 8, 5, 1, 6)$, $N2(9, 7, 8, 3, 1, 6)$, $N3(7, 2, 6, 5, 1, 4)$, and $N4(7, 6, 2, 8, 9, 4)$ for the four examples. After selecting the phase value set, the FFT calculations are carried out

doi:10.5047/978-4-88704-171-4

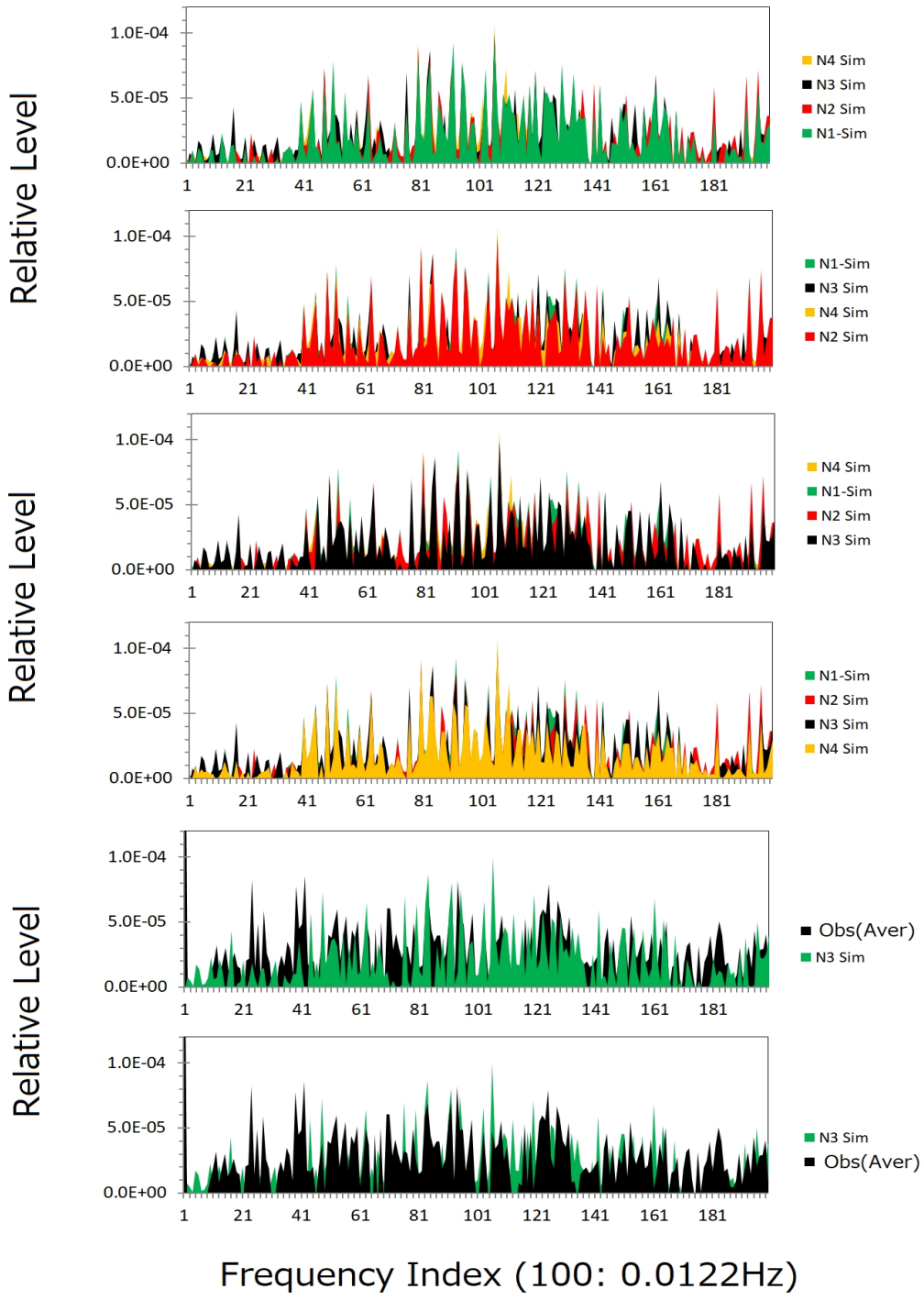

Fig. 16. Comparison of results of simulated FFT spectra among four different phase setting parameters and the observed spectra given as average of four observational data series. The simulated results for the phase settings N1, N2, N3, and N4 are given all together in each panel from the top to the 4-th panel where front view of each display runs from N1 to N4 in order. Comparisons of the spectra with that for the observations averaged GA1 to GA4 cases are given in the bottom two panels where the simulated results of the spectra for the N3 phase setting are displayed in the front side in 5-th panel while observation spectra are displayed in the front in the bottom panel.

for searching the best fit simulation function for the remaining 11 parameters.

From sidebands with a constant frequency gap between peaks in the FFT results (discussed in Subsec. 7.5.1) for the observations, the orbital period is estimated to be 2200 ± 50 sec. For four parameters such as T_a, T_b, v_a and v_b there are three assumed values for each (see Table 7); and three values to be found for six parameters, a_n and b_n ($n = 1, 2,$ and 3) (see Table 8). That is, 59049 ($= 3^{10}$) cases, in total, except for simulated phase combinations, are tried aiming to find best fitting case with the averaged observation results of FFT analyses for the observation cases GA1, GA2, GA3 and

doi:10.5047/978-4-88704-171-4

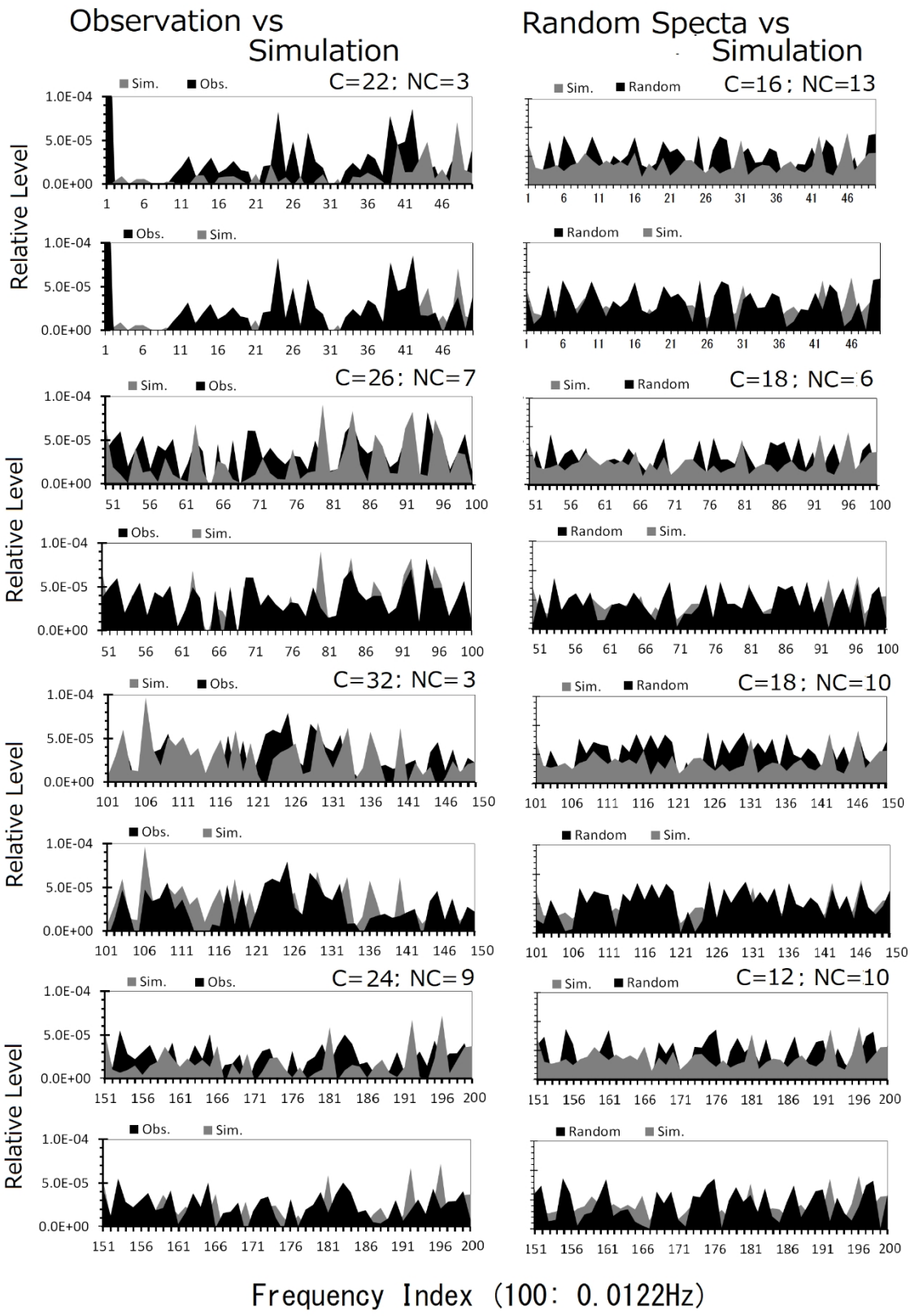

Fig. 17. An example of the diagram where details of the comparisons of the simulation FFT with FFT of observation data for GA1 and random spectrum are indicated expanding the frequency axis four times of the original diagram given in Fig. 15. That is, the original diagram is split into four parts with frequency indicators as given in the abscissa. The statistics of coincidence of the peaks of spectra versus non coincidence of the peaks of spectra are given as C = number: NC = other number.

doi:10.5047/978-4-88704-171-4

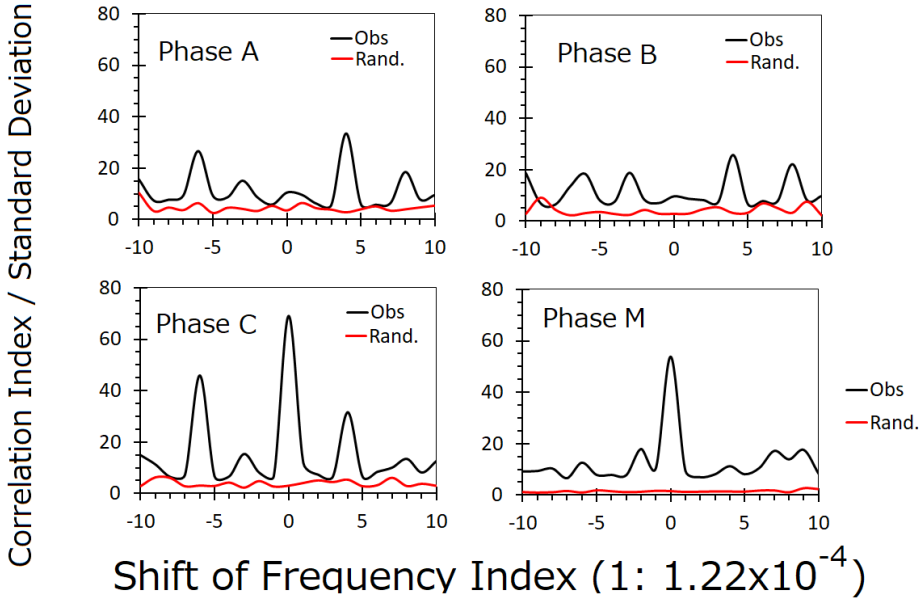

Fig. 18. The index of the coincidence $C_k(\Delta f)$ for four cases of the phase combination Phase A (N1:) Phase B (N2), Phase C(N3) and Phase M. The correlation indices for the observational spectra versus simulated spectra are indicated with black curves; and the correlation indices for the random spectra versus simulated spectra are indicated by red curves.

GA4.

7.5.4 Simulated Results

In Fig. 16, the best fit of the simulated results for an arbitrarily selected four sets of phase combinations are compared with average FFT results for observation data. It becomes clear that there is a remarkable coincidence between the simulated results for four different phase combinations from N1 to N4 when using the frequencies of the spectral peaks. That is, we can state that the difference in phase of each higher harmonic controls only the level of resulting spectra but has no effect on the occurrence of the spectral peaks. From the four simulated spectra then, we have selected the case of N3 as the best representative of the simulations whose general feature of the spectra fits well with the observations (see 5-th and bottom panels of Fig. 16). The reason for selecting the N3 spectra as representative of the simulated spectra, at this stage, will be described in the next Subsec. 7.6.

7.6 Objective evaluation of coincidence of the simulated spectra with the observations

To obtain an objective evaluation of how well the simulated spectra fit the observations, we decided to compare with the case of random spectra to which we can find only accidental coincidence. The random spectra are constructed by using a random series of numbers at each frequency slot of the spectra. There are 200 slots for the full frequency range in analyzing FFT results; then, we select 200 random numbers as a series to deliver into the 200 slots in the order as given in the right hand column of Fig. 17 as an example. A simple first step for evaluation is to determine the ratio between the number of coincidences of the spectral peaks and the simulated results. In the case of Fig. 17, the coincidence ratio between the simulated and observational results is 0.825 while the ratio between the simulated and random spectra is 0.615. There is an apparent difference between the observational versus the simulated results and the random versus the simulated spectra. Nevertheless the definite threshold is unclear because the ratio of fitting for the case of the random versus the simulated spectra. is larger than 0.5. This problem originates in the resolution limit of the frequency. That is, when we separate the spectral peaks at one frequency slot, sometimes they are delivered into the same spectra due to a numerical error of less than the 0.5 frequency slot but sometimes they are delivered into a neighboring frequency slot. Thus, the method using the ratio to evaluate the fitness of two spectra contains an ambiguity. So we have selected an index that has a better confidence level. The basic difference between random spectra and observational spectra is in the recurrence feature of the spectra when we prepare spectra that originate at different times from each other. We have four independently observed data series GA1, Ga2, GA3 and GA4; therefore, four sets of random spectra have been employed to evaluate the coincidence between the simulated spectra. For this situation, the index of the coincidence $C_{\rm IND}$ is defined by taking two steps as follows. In the first step the coincidence index S_{kj} is defined by Eq. (84)

$$S_{kj}(\Delta f) = \sum_{i=20}^{180} F_{kj}(f_i) \cdot F_{Sj}(f_i - \Delta f) / \sum_{i=20}^{180} [F_{kj}(f_i) - F_{Sj}(f_i - \Delta f)]^2 \qquad (84)$$

where $F_{kj}(f_i)$ is the k-th spectra ($k = S$ for simulated results, $k =$ Ob for observational results and $k =$ RAN for random

doi:10.5047/978-4-88704-171-4

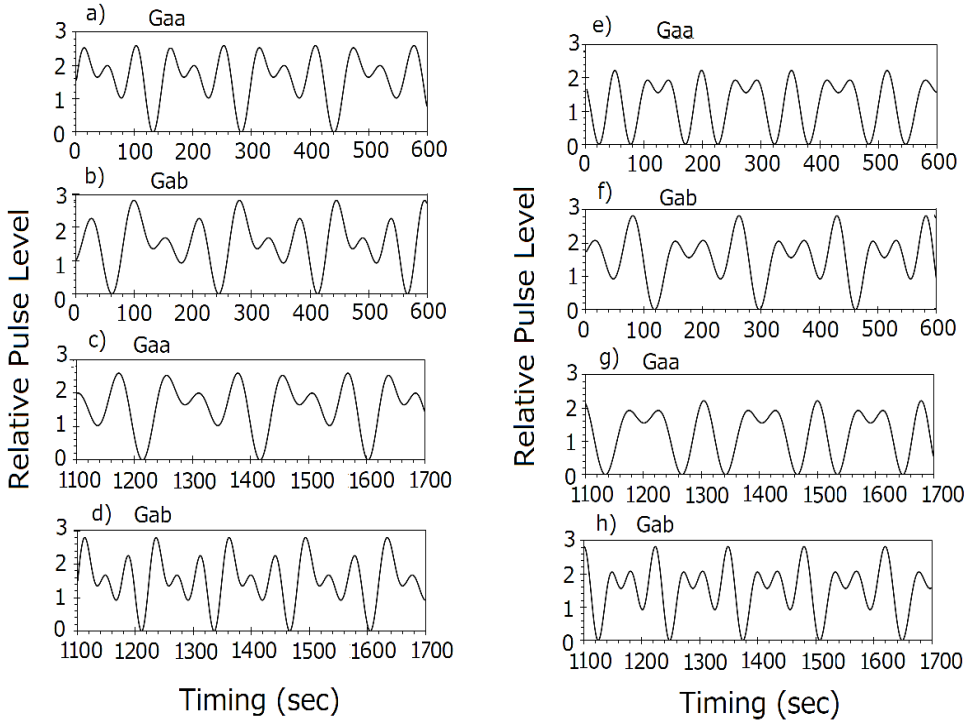

Fig. 19. Recovered pulse forms resulting as the simulation functions whose FFT results show coincidences with the observed FFT spectra. Simulated results are selected for two phase combinations, M and N3, i.e. the pulse forms given in panels a) to d) are due to the simulated function with phase combination M. The pulse forms in panels e) to h) are due to the simulated function with phase combination N3. Based on the corresponding simulated functions, pulse forms from BH Gaa and Gab are displayed for two periods which are selected between 0 to 600 sec and 1100 sec to 1700 sec; the later time interval corresponds to the passage of half of orbital period.

spectra) with data series j ($j = 1$ for GA1, $j = 2$ for GA2, $j = 3$ for GA3 and $j = 4$ for GA4 for the observations; and from $j = 1$ to $j = 4$ for random spectra from random noise series 1 to series 4, respectively). The spectra are expressed as a function of the frequency f_i corresponding to the i-th frequency slot which starts from 1 and ends at 200; because the mutual correlation function of the partner spectra frequency is shifted by frequency Δf whose minimum step is 1 out of the 200 total slots of full frequency range.

As second step to complete the definition of coincidence C_k, we take, here, averages of $S_{kj}(\Delta f)$, that is defined as

$$C_k(\Delta f) = \overline{S_k(\Delta f)}/SD_k(\Delta f) \tag{85}$$

where $\overline{S_k(\Delta f)}$ and $SD_k(\Delta f)$ are averages of $S_{kj}(\Delta f)$ and standard deviation respectively that are defined by

$$\overline{S_k(\Delta f)} = \frac{1}{4}\sum_{j=1}^{4} S_{kj}(\Delta f) \tag{86}$$

and

$$SD_k(\Delta f) = \sqrt{\frac{1}{4}\sum_{j=1}^{4}[S_{kj}(\Delta f) - \overline{S_k(\Delta f)}]^2}. \tag{87}$$

In Fig. 18, the defined indices of the coincidence $C_k(\Delta f)$ are indicated in the four panels of phase A, phase B, and phase C, which show the phase combination of the simulated function as N1, N2, N3, respectively. The apparent difference of the index values between $k =$ Ob and $k =$ RAN confirms the statement that the observational spectra are completely different from the random spectra. The result also provide a worthwhile evaluation between the simulated spectra that result from the different phase combinations. Here we have selected phase M, instead of N4; the combination M(4, 4, 5, 8, 5, 3) selected from 4096 trials of a random selection of combinations which indicate the best C_k showing fitting of the FFT results between the simulation and observation cases..

7.7 Recovery of Pulse Form

In Fig. 19, the pulse forms of radio waves transmitted from the two objects of the black hole binary are indicated as the result of the simulated functions which give FFT spectra coinciding with the observations. Simulated functions are selected for two phase combinations as M and N3, i.e. the pulse forms given from panels a), c) e) and g) are due to the black hole Gaa and panels b), d), f) and h) are for the black hole Gab.

We can see here the wave forms given by simulation functions. Results with different phase combinations show that the detail of the wave form sensitively varies depending on the phase combinations; but the occurrence of three peaks of intensity of pulses seems to be common characteristics

doi:10.5047/978-4-88704-171-4

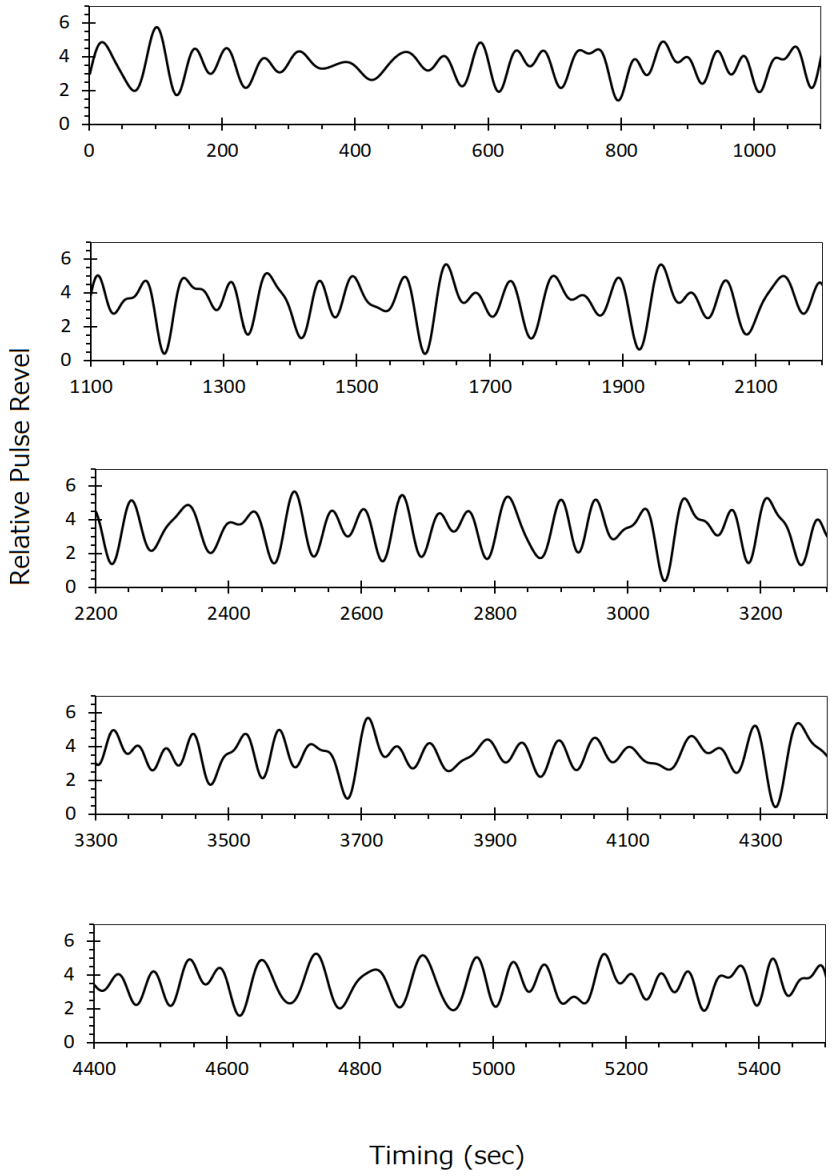

Fig. 20. Time series of combined pulse forms of real time observations of intensity variation of decameter radiation from the region close to the event horizon of binary black holes having orbital period of 2200 sec with spin periods 173 sec and 148 sec, respectively for Gaa and Gab.

suggesting basic azimuthal dependence of the radiation environment of the sources of rotating black holes. Pulse forms from BH Gaa and Gab are displayed for two periods of timing selected from 0 to 600 sec and 1100 sec to 1700 sec. The latter time is a period when it passes half of orbital period measured from the initial interval. We can then see the variation of the spinning periods due to Doppler effects of the orbital motion that opposes the motions of Gaa and Gab in their orbits. The display of the pulse forms in Fig. 19 are made by artificially distinguishing between Gaa and Gab to see the individual variations. When observing the pulses of both Gaa and Gab in real time, the results become complicated as shown in Fig. 20, where a series of combined pulse form for a period about two and a half orbital rotations is shown.

8. DETECTION OF THE SOURCE DIRECTION UNDER THE DISTURBANCE OF IONOSPHERE

8.1 Principle of Virtual Shift of the Interferometer System into the Vacuum Space

When searching for the source direction in the decameter wave range, we have tried to be free of the ionosphere which greatly shifts the propagation path of radio waves, even at 21.860 MHz, away from a straight line between the source and the receiving points. Sometimes the arrival direction of the ray deviates more than five degrees from the direction of the source depending on the plasma density and the elevation angle of the source. In the present work, the source direction has been obtained without ionospheric disturbance by artificially setting a pseudo interferometer system to the position exactly on the real ray path in space where there is no effect

doi:10.5047/978-4-88704-171-4

of ionosphere plasma.

Analyses of the source direction of the signals of the present studies have been made by applying IFFCM (interferometer fringe function correlation method) to the detection of the source direction as given in Sec. 5. To search for the source direction assumed to be the Galactic center at Sgr A*, the wave normal vector $\boldsymbol{k}_p$ is varied in Eqs. (26) and (27) around the source at right ascension 17 h 45 m 40 s and declination $-29^\circ 00' 20''$ using the deviation of the wave normal vector $\Delta\boldsymbol{k}_p$ as the searching tool. We are searching for the pulse forms which are described by the FFT spectra generated by binary black holes explained in Sec. 7. When we rewrite Eqs. (26) and (27) using only the signal part of terms, the correlation functions are expressed by,

$$\begin{aligned} SC_{ij} = \frac{1}{T_p}\int_{t=t_n}^{t_n+T_p} & S_0^2(t) \\ & \cdot\cos[(\boldsymbol{k}_s+\boldsymbol{k}_I)\cdot(\boldsymbol{r}_j-\boldsymbol{r}_i)+(\theta_i-\theta_j)] \\ & \cdot\cos[(\boldsymbol{k}_P+\Delta\boldsymbol{k}_p)\cdot(\boldsymbol{r}_j-\boldsymbol{r}_i)]dt \end{aligned} \tag{88}$$

$$\begin{aligned} SD_{ij} = \frac{1}{T_p}\int_{t=t_n}^{t_n+T_p} & S_0^2(t) \\ & \cdot\cos[(\boldsymbol{k}_s+\boldsymbol{k}_I)\cdot(\boldsymbol{r}_j-\boldsymbol{r}_i)+(\theta_i-\theta_j)] \\ & \cdot\sin[(\boldsymbol{k}_P+\Delta\boldsymbol{k}_p)\cdot(\boldsymbol{r}_j-\boldsymbol{r}_i)]dt \end{aligned} \tag{89}$$

where $\boldsymbol{k}_I$ is wave number vector which indicates the deviation of the arrival direction from the source direction $\boldsymbol{k}_s$ due to ionospheric disturbance. By selecting a point on the ray path of the arriving radio wave at $\boldsymbol{r}_{isp}$, in space, Eqs. (88) and (89) are rebuilt as

$$\begin{aligned} SC_{ij} = \frac{1}{T_p}\int_{t=t_n}^{t_n+T_p} & S_0^2(t) \\ & \cdot\cos[\boldsymbol{k}_s\cdot(\boldsymbol{r}_{jsp}-\boldsymbol{r}_{isp})+(\Phi_i-\Phi_j)] \\ & \cdot\cos[(\boldsymbol{k}_P+\Delta\boldsymbol{k}_p)\cdot(\boldsymbol{r}_{jsp}-\boldsymbol{r}_{isp})]dt \end{aligned} \tag{90}$$

and

$$\begin{aligned} SD_{ij} = \frac{1}{T_p}\int_{t=t_n}^{t_n+T_p} & S_0^2(t) \\ & \cdot\cos[\boldsymbol{k}_s\cdot(\boldsymbol{r}_{jsp}-\boldsymbol{r}_{isp})+(\Phi_i-\Phi_j)] \\ & \cdot\sin[(\boldsymbol{k}_P+\Delta\boldsymbol{k}_p)\cdot(\boldsymbol{r}_{jsp}-\boldsymbol{r}_{isp})]dt \end{aligned} \tag{91}$$

where $\Phi_i = \int_{\boldsymbol{r}_{isp}}^{\boldsymbol{r}_i}\boldsymbol{k}_s(\boldsymbol{r})\cdot d\boldsymbol{r}+\theta_i$ and $\Phi_i-\Phi_j = \int_{\boldsymbol{r}_{jsp}}^{\boldsymbol{r}_j}\boldsymbol{k}_s(\boldsymbol{r})\cdot d\boldsymbol{r} - \int_{\boldsymbol{r}_{isp}}^{\boldsymbol{r}_i}\boldsymbol{k}_s(\boldsymbol{r})\cdot d\boldsymbol{r}+(\theta_i-\theta_j)$.

Taking an analogous approach as arriving at Eqs. (47) and (48), starting from Eqs. (26) and (27), SC_{ij} and SD_{ij} given by Eqs. (90) and (91), provide following relations, as

$$\begin{aligned} SC_{ij} = \frac{1}{4}S_0^2\cos[(\boldsymbol{k}_s-\boldsymbol{k}_P-\Delta\boldsymbol{k}_p)\cdot(\boldsymbol{r}_{jsp}-\boldsymbol{r}_{isp})] \\ \cdot\cos(\Phi_i-\Phi_j), \end{aligned} \tag{92}$$

and

$$\begin{aligned} SD_{ij} = \frac{1}{4}S_0^2\cos[(\boldsymbol{k}_s-\boldsymbol{k}_P-\Delta\boldsymbol{k}_p)\cdot(\boldsymbol{r}_{jsp}-\boldsymbol{r}_{isp})] \\ \cdot\sin(\Phi_i-\Phi_j). \end{aligned} \tag{93}$$

That is, signal parts of Eqs. (47) and (48) are expressed as

$$C_{ijS} = \frac{1}{4}S_0^2(t_n)\cos\Delta\Phi_{Pij}\cos\theta_{ij}, \tag{94}$$

and

$$S_{ijS} = -\frac{1}{4}S_0^2(t_n)\cos\Delta\Phi_{Pij}\sin\theta_{ij}, \tag{95}$$

for the case $\boldsymbol{k}_s = \boldsymbol{k}_P$, in Eqs. (92) and (93), $(\boldsymbol{k}_s-\boldsymbol{k}_P-\Delta\boldsymbol{k}_p)\cdot(\boldsymbol{r}_{jsp}-\boldsymbol{r}_{isp})$ is equivalent to $\Delta\Phi_{Pij}$, and $\Phi_i-\Phi_j$ is equivalent to θ_{ij}. When we consider the total quantity including sky noise and the signal together, then we can use the processes from Eq. (26) to Eq. (48) by replacing θ_i with Φ_i and $\boldsymbol{r}_i$ with $\boldsymbol{r}_{isp}$, to obtain the source direction, of signals, that is free of ionospheric disturbance. Following the processes from Eq. (52) to Eq. (53), then, we can write the signal part from Eqs. (92) and (93), as

$$\begin{aligned} \sqrt{SC_{ij}^2+SD_{ij}^2} \\ = \frac{1}{4}S_0^2\cos[(\boldsymbol{k}_s-\boldsymbol{k}_P-\Delta\boldsymbol{k}_p)\cdot(\boldsymbol{r}_{jsp}-\boldsymbol{r}_{isp})]. \end{aligned} \tag{96}$$

To detect the source direction without the disturbance of the ionosphere, however, it is essential that the point $\boldsymbol{r}_{isp}$ is set at a point located in the space outside of the ionosphere, but still on the real ray path of the observed radio waves. We will call this point "the point of space interferometer" (PSI) hereafter. To find PSI we search for a position where the correlation values used to find the source direction become maximum. We do this by sweeping the two necessary parameters to find the position in a plane where the two vectors $\boldsymbol{r}_{isp}$ and $\boldsymbol{k}_s$ are included together.

In Figs. 21 and 22, we show the geometry that defines the procedure to set the position of PSI; the position is described in a common plane given by the observation point $\boldsymbol{r}_i$ and wave number vector $\boldsymbol{k}_s$ of the observing radio wave. As a starting point to search for the position vector of PSI, we set the point $\boldsymbol{r}_{IN}$ at the topside of the ionosphere (selected as the limit of the ionosphere) on the straight line that is assumed to connect the source and observation points by neglecting the effects of the ionosphere; then $\boldsymbol{r}_{IN}$ is expressed by using two unit vectors $\hat{\boldsymbol{r}}_i$ and $\hat{\boldsymbol{v}}_i$ that are vertically selected with respect to $\hat{\boldsymbol{r}}_i$ as

$$\hat{\boldsymbol{v}}_i = (\hat{\boldsymbol{r}}_i\times\boldsymbol{k})\times\frac{\hat{\boldsymbol{r}}_i}{K}. \tag{97}$$

By taking $A = \hat{\boldsymbol{r}}_i\cdot\hat{\boldsymbol{k}}$ and $K = \sqrt{1-A^2}$, then, Eq. (97) is rewritten to

$$\hat{\boldsymbol{v}}_i = \frac{(-A\hat{\boldsymbol{r}}_i+\boldsymbol{k})}{\sqrt{1-A^2}}. \tag{98}$$

As we can see in Fig. 22, $\hat{\boldsymbol{r}}_{IN}$ is expressed by $\cos\phi\hat{\boldsymbol{r}}_i + \sin\phi\hat{\boldsymbol{v}}_i$, then it follows that

$$\begin{aligned} \hat{\boldsymbol{r}}_{IN} = \left(\cos\phi-\frac{A}{\sqrt{1-A^2}}\sin\phi\right)\cdot\hat{\boldsymbol{r}}_i \\ +\frac{1}{\sqrt{1-A^2}}\sin\phi\cdot\hat{\boldsymbol{k}}. \end{aligned} \tag{99}$$

doi:10.5047/978-4-88704-171-4

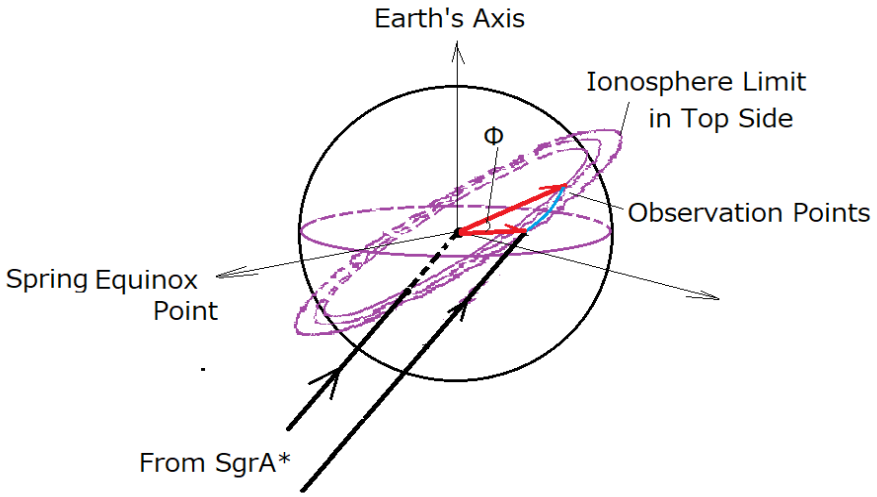

Fig. 21. A common plane including the ray path from Sgr A* and the vector of the observation point of the geocentric origin; geometrical relations are described in the coordinate system of the spring equinox, equator, and Earth-s rotation axis.

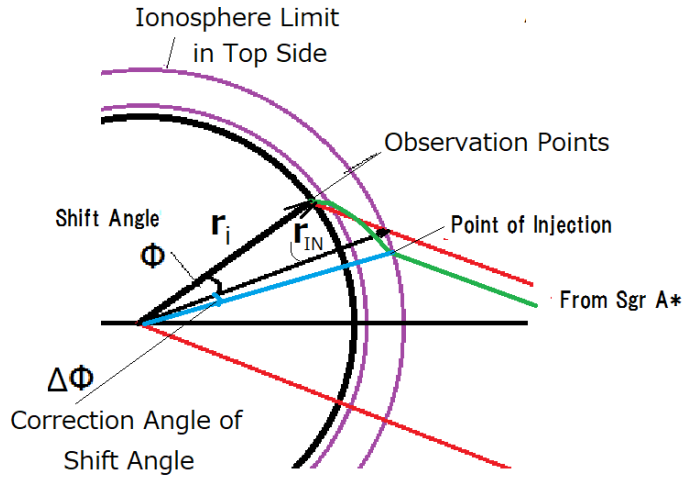

Fig. 22. Geometrical relationship of the observing ray path in a common plane of the ray path from Sgr A* and observation point vector of the geocentric origin. The image of the ray path under the effect of the ionosphere is also depicted (green curve) with the point of injection described by the geocentric vector at the top of the ionosphere.

Considering geometrical relation also in Fig. 22, the vector $\boldsymbol{r}_{IN}$ is given by

$$\boldsymbol{r}_{IN} = \boldsymbol{r}_i + (r_{IN}^2 + r_i^2 - 2r_{IN} \cdot r_i \cos\phi)^{1/2}\hat{\boldsymbol{k}}. \quad (100)$$

From Eqs. (99) and (100) $\cos\phi$ is given as

$$\cos\phi = B(1 - A^2) \pm A\sqrt{1 - B^2(1 - A^2)}, \quad (101)$$

where $B = r_i/r_{IN}$.

In the spring equinox-equator coordinate system as shown in Fig. 21, the position of the observation $\boldsymbol{r}_i$ depend on the time t as given by

$$\begin{aligned}\boldsymbol{r}_i &= r_i \cos[\Omega_e(t - t_0) + \psi]\cos\lambda\hat{\boldsymbol{x}}_e \\ &\quad + r_i \sin[\Omega_e(t - t_0) + \psi]\cos\lambda\hat{\boldsymbol{y}}_e + r_i \sin\lambda\hat{\boldsymbol{z}}_e, \end{aligned} \quad (102)$$

where Ω_e is angular velocity of the Earth's rotation; ψ, and λ are the longitude of the observation point at time t_0, and the latitude of the observation point respectively. In Eq. (102), $\hat{\boldsymbol{x}}_e$, $\hat{\boldsymbol{z}}_e$, and $\hat{\boldsymbol{y}}_e$ are the unit vector directed toward the Sun at the spring equinox, the unit vector directed to Earth's rotation axis, and the unit vectors directed vertically to $\hat{\boldsymbol{x}}_e$, and $\hat{\boldsymbol{z}}_e$, respectively. Then, A is expressed as

$$\begin{aligned} A &\equiv \hat{\boldsymbol{r}}_i \cdot \hat{\boldsymbol{k}} \\ &= \cos[\Omega(t - t_0) + \psi] \cdot \cos(Ra) \cdot \cos\lambda \cdot \cos(De) \\ &\quad + \sin[\Omega(t - t_0) + \psi] \cdot \sin(Ra) \cdot \cos\lambda \cdot \cos(De) \\ &\quad + \sin\lambda \sin(De). \end{aligned} \quad (103)$$

In Fig. 22, we can find the procedure to find PSI just on the real ray path where the decameter radio wave propagation is affected by the ionosphere. The effects of the ionosphere change the ray path from the initially assumed straight line path for propagation through a vacuum. We express this change as "correction angle of the shift angle

doi:10.5047/978-4-88704-171-4

(CASA)" which exactly decides the point of injection at a limiting height of the ionosphere. In the present study CASA cannot be analytically expressed; but we can search for it by sweeping the CASA value until the correlation function in the present IFFCM (see Sec. 5) reaches maximum for real observation data.

As indicated by Eq. (103), when the "A" value is changed as a time dependent function, the shift angle ϕ is also varies as function of time; thus, CASA is understood as the average correction angle deviating from the original shift angle. While searching for CASA we see that CASA is not only within the plane formed to include $\boldsymbol{r}_i$ and $\boldsymbol{k}_s$ but also CASA takes place in the azimuth direction, because of the inhomogeneous distribution of the ionospheric electron density in the direction of longitude. We express CASA as a shift in phi (CASA φ) which take place in the longitudinal direction. It should be noted that CASA and CASA φ never affect the result of the detected source direction but are related to the determination of PSI which affects the correlation intensity of analyzing signals to evaluate whether PSI is set just on the ray path.

8.2 The case of One degree Resolution

Figs. 23 to 26 indicate the results of direction finding for observations corresponding to GA1 to GA4, respectively. The results are given as average values of the relative spectral level (ARSL, hereafter) deduced by FFT analyses for a function of the correlation to detect the direction by IFFCM for the five directions aimed with one degree resolution surrounding the direction of Sgr A*. In all diagrams the average level of the spectra of the FFT results are plotted versus five directions that are indicated 1, 2, 3, 4, and 5 in the abscissa corresponding north-east (+1 deg, +1 deg), south-east (−1 deg, +1 deg), direction of Sgr A*, (0 deg, 0 deg) south-west (−1 deg, −1 deg), and north-west (+1 deg, −1 deg), respectively. That is, indicating by ($\pm a$ deg, $\pm b$ deg), we express the direction aiming the sky position that shifts in the north-south direction by $\pm a$ degree and shifts in east-west direction by $\pm b$ degree centered around the direction of Sgr A*. In all cases, we assume that $r_{IN} = 825$ km; in all the Figs. 23 to 26, the search results of CASA and CASA φ are expressed as a variation of the "averaged relative spectrum level (ARSL)" as a function of the aiming direction for various combinations of CASA and CASA φ as parameter. Corresponding to Figs. 23 to 26 then, we can find the maximum value of ARSL, at CASA $= 3.2^\circ$, CASA $\varphi = 0.5^\circ$ for data GA1; CASA $= 3.4^\circ$, CASA $\varphi = 0.5^\circ$ for data GA2; CASA $= 3.2^\circ$, CASA $\varphi = 2.0^\circ$ for data GA3; and CASA $= 3.8^\circ$, CASA $\varphi = 4.75^\circ$ for data GA4 respectively. Although CASA and CASA φ that give the maximum ARSL, insuring the coincidence of the ray path and PSI, are limited in a range around 3.2° for CASA and less than 5° for CASA φ, there are differences resulting from data that reflect the ionospheric condition at the observation times. The points of local maximum of ARSL are, however, fixed in the direction of Sgr A*. We conclude that the source direction of radio wave pulses represented by the spectra of the FFT results is definitely toward Sgr A* with the resolution of one degree.

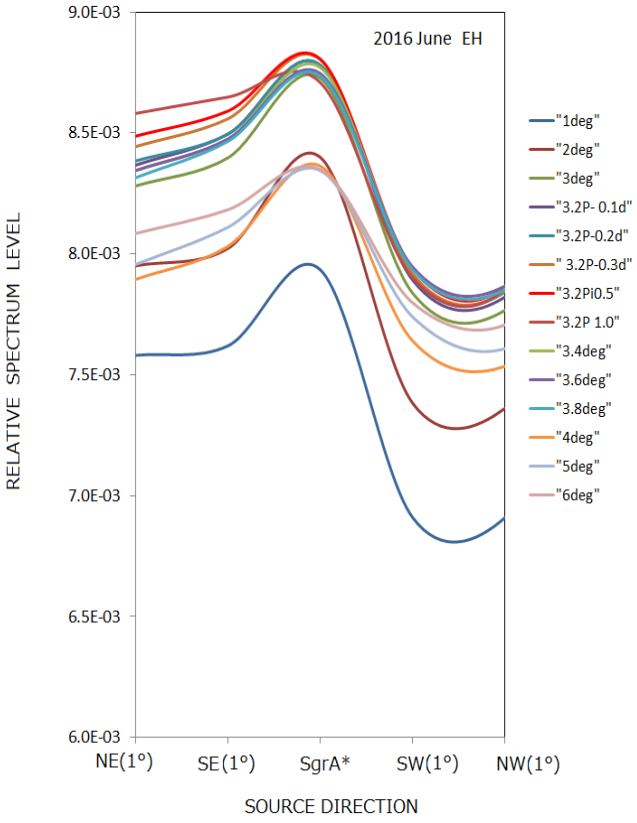

Fig. 23. Relative spectrum level for a function of the direction finding correlation in IFFCM for five directions, centered on Sgr A* for observation data GA1 (2016 June Early Half period). NE(1°), SE(1°) SW(1°), and NW(1°) indicate the direction where the differences in right ascension and declination of the direction of the interest shift by one degree as NE(1°) $= (+1^\circ, +1^\circ)$, SE(1°) $= (+1^\circ, -1^\circ)$, SW(1°) $= (-1^\circ, -1^\circ)$, and NW(1°) $= (-1^\circ, +1^\circ)$. Explanations for CASA and CASA φ for the corresponding curves are given with a form such as "3.2 P0.5" that means CASA $= 3.2^\circ$ and CASA $\varphi = 0.5^\circ$. The form "3.8 deg", for example, means that CASA $= 3.8^\circ$ and CASA $\varphi = 0^\circ$.

In Fig. 23 we can see that there is an east-west asymmetry of ARSL versus corresponding directions centered around the Sgr A* direction. The asymmetry is not due to the shifting of the source position from the exact direction of Sgr A* but is caused by the asymmetry of reception at the antenna located at each local station of the interferometer system. The details for the origin of the asymmetry will be given in the next Subsec.

8.3 The case for 0.1 degree resolution

In Fig. 27, ARSL is plotted as function of the five directions centered on the direction of Sgr A* with 0.14 degree steps in the North-East (1), South-East (2), South-West (4) and North-West (5) directions. We can see that there is an apparent east- west asymmetry of ARSL. The asymmetry is not due to the eastward shift of the radio wave source direction biased from the exact direction of Sgr A*, but the asymmetry is caused by the antenna directivity at the reception of each radio wave. at stations of the interferometer system.

Let's define the directivity of the antenna at i-th and j-th stations of the interferometer system to be $f_i(\psi, \delta)$ and $f_j(\psi, \delta)$ for the local azimuth ψ and elevations. Then the

doi:10.5047/978-4-88704-171-4

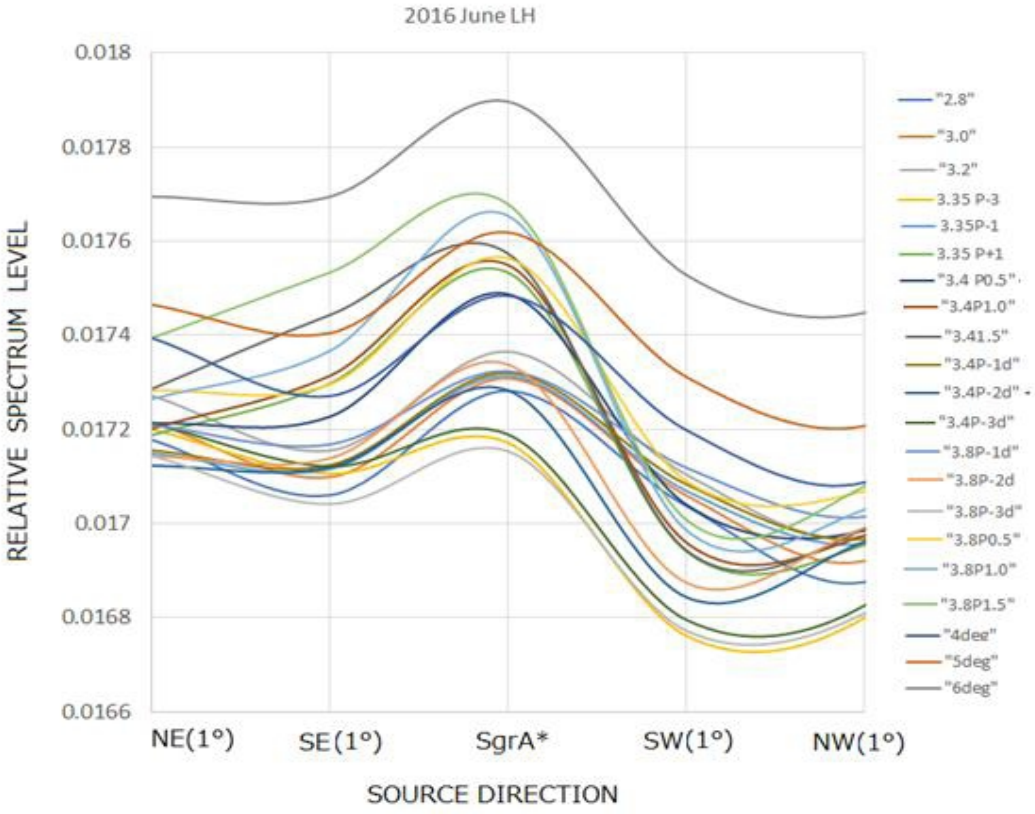

Fig. 24. The same as Fig. 23, for the case of GA2 (2016 June Late half period) observations.

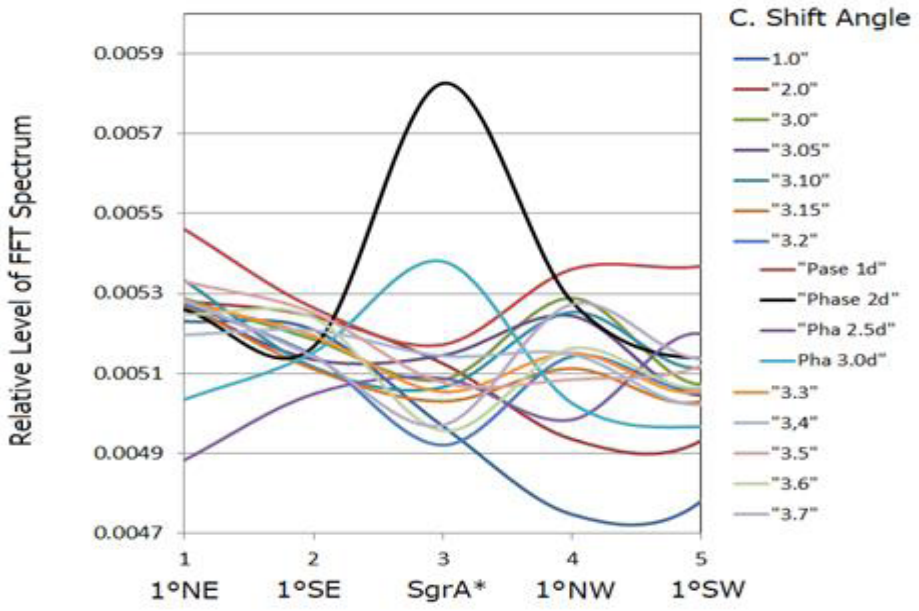

Fig. 25. The same as Fig. 23 for the observations of GA3.

doi:10.5047/978-4-88704-171-4

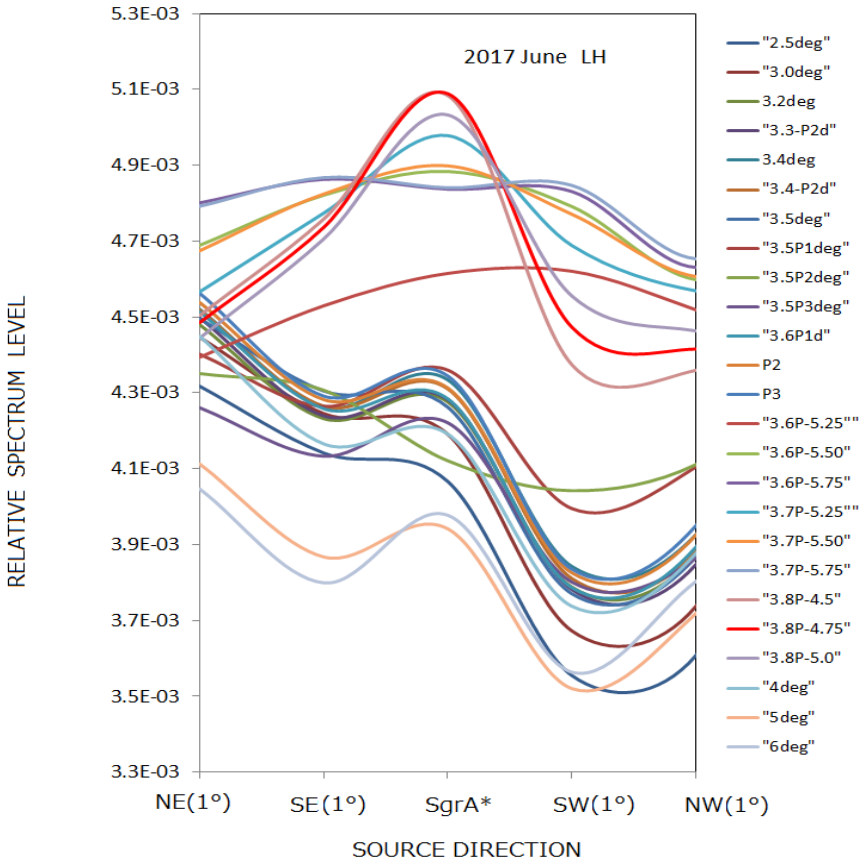

Fig. 26. The same as Fig. 23 for the observations for GA4.

average output-level of the interferometer is obtained by integrating over an observation interval T_I as given by,

$$P_{ij} = \frac{E_0^2}{T_I}\int_t^{t+T_I} f_i(\psi,\delta)\cdot f_j(\psi,\delta)\cos(\omega t - \boldsymbol{k}\cdot\boldsymbol{r}_i + \theta_i) \cdot\cos(\omega t - \boldsymbol{k}\cdot\boldsymbol{r}_i + \theta_i)dt. \quad (104)$$

Integrating Eq. (104) over an interval T_I, then it follows that (by similar mathematical manipulation as given in Appendix C)

$$P_{ij} = \frac{E_0^2}{2} f_i(\psi,\delta) f_j(\psi,\delta) \cdot\cos[\boldsymbol{k}\cdot(\boldsymbol{r}_j - \boldsymbol{r}_i) + \theta_i - \theta_i]. \quad (105)$$

When the unit vector of the antenna direction is expressed by $\hat{\boldsymbol{L}}_i$, (perpendicular to the element of Yagi or dipole antenna) then $f_i(\psi,\delta)$ is given by

$$f_i(\psi,\delta) = (\hat{\boldsymbol{L}}_i\cdot\hat{\boldsymbol{k}})^{\xi} \quad (106)$$

where ξ is integer for approximated expression of the directivity of dipole and Yagi antennas; we select $\xi = 6$ for 5-element Yagi antenna that is set at each receiving station of the interferometer for present observation. In Eq. (106), $\hat{\boldsymbol{L}}_i$ and $\hat{\boldsymbol{k}}$ are expressed by

$$\hat{\boldsymbol{L}}_i = \cos(\Omega_e t + \varphi_{ob})\cdot\cos(\lambda_{ob} - \theta_{ai})\widehat{\boldsymbol{x}_e} + \sin(\Omega_e t + \psi_{ob})\cdot\cos(\lambda_{ob} - \theta_{ai})\widehat{\boldsymbol{y}_e} + \sin(\lambda_{ob} - \theta_{ai})\widehat{\boldsymbol{z}_e}, \quad (107)$$

and

$$\hat{\boldsymbol{k}} = \cos\psi\cdot\cos\delta\widehat{\boldsymbol{x}_e} + \sin\psi\cdot\cos\delta\widehat{\boldsymbol{y}_e} + \sin\delta\widehat{\boldsymbol{z}_e}, \quad (108)$$

where $\widehat{\boldsymbol{x}_e}$, $\widehat{\boldsymbol{y}_e}$, and $\widehat{\boldsymbol{z}_e}$ are the same unit vectors that are described in Subsec. 8.1 for the coordinate system with the vernal equinox, equatorial plane, and Earth rotation axis coordinate system; the azimuth angle of the directivity of the receiving antenna at i-th station is fixed towards exactly south with a fixed elevation angle of θ_{ai}. The angle φ_{ob} is defined as the longitude of the i-th station when the start of the time t is set at UT = 00 h 00 m 00 s at the vernal equinox. Using Eqs. (107) and (108), therefore, Eq. (106) is rewritten as

$$f_i(\psi,\delta) = \cos(\Omega_e t + \varphi_{obi} - \psi)\cos(\lambda_{obi} - \theta_{ai})\cos\delta + \sin(\lambda_{obi} - \theta_{ai})\sin\delta. \quad (109)$$

In Eqs. (20) to (23) the amplitude of the output of the interferometer is given without the effects of the directivity of the receiving antenna. We then modified the signal components given in Eqs. (20) to (23) by multiplying by a factor,

doi:10.5047/978-4-88704-171-4

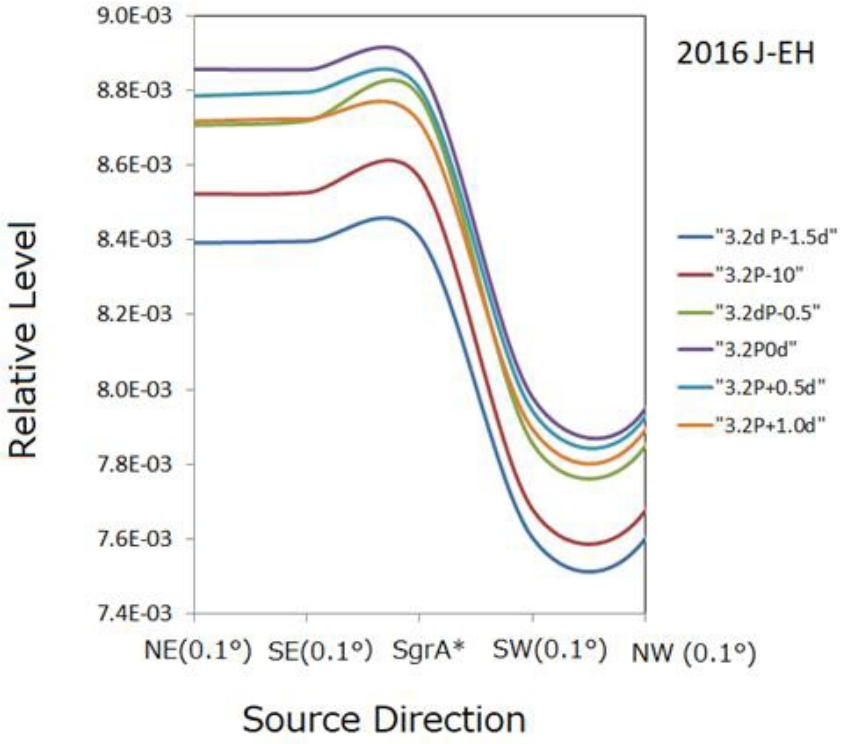

Fig. 27. Relative spectrum level for a function of the direction finding correlation ARSL in IFFCM, for five directions, NE(0.1°), SE(0.1°) SW(0.1°), and NW(0.1°), centered on Sgr A*, for observations of GA1 (2016 June Early Half period). The differences from Sgr A* in right ascension and declination of the direction is shifted by 0.1 degree as NE(0.1°) = (+0.1°, +0.1°), SE(0.1°) = (+0.1°, −0.1°), SW(0.1°) = (−0.1°, −0.1°), and NW(0.1°) = (−0.1°, +0.1°). Explanations for CASA, and CASA φ, for the corresponding curves are given with a form such as "3.2 P0.5" that means CASA = 3.2° and CASA φ = 0.5°.

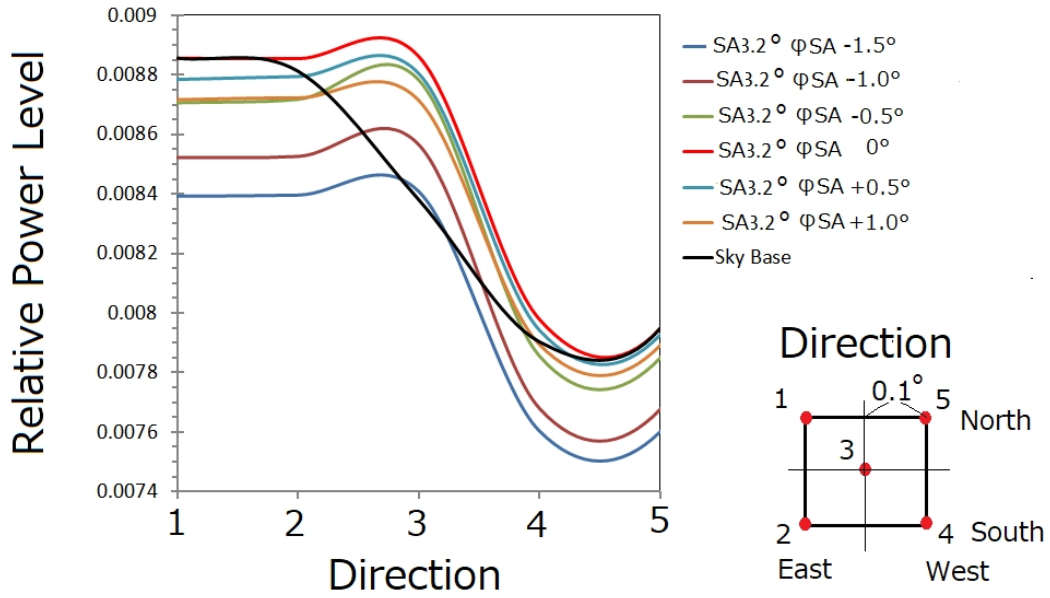

Fig. 28. The theoretically deduced ARSL for background sky (black curves) with observation results given in Fig. 27. The theoretical level is calculated for 5-element Yagi antenna assuming homogeneously distributed sources in the sky as zero base line of the present system to make the direction finding of the signal. SA and φSA are equivalent to CASA and CASAφ.

doi:10.5047/978-4-88704-171-4

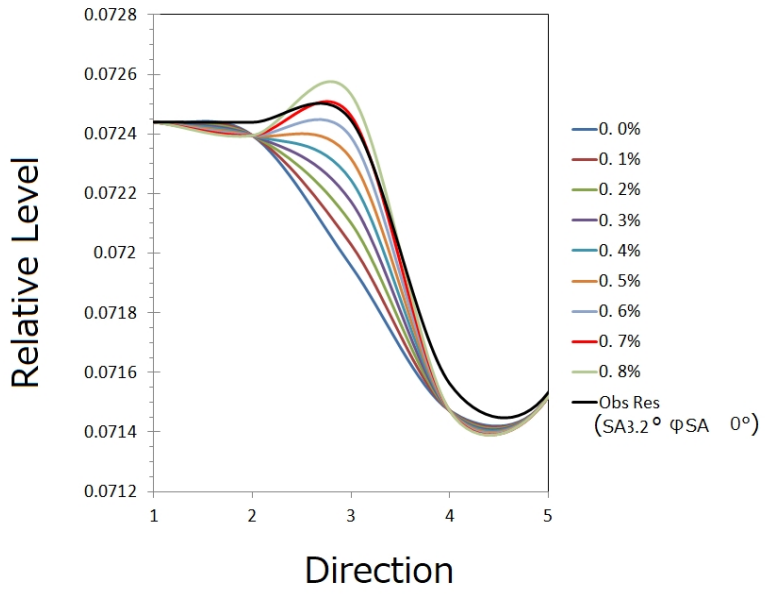

Fig. 29. Calculations of ARSL with observations results of GA1(2016 June EH: Red curves). Calculations of ARSL have been carried out assuming the source intensity at Sgr A* from 0 to 0.8% of the background level of sky noise; the definition of the direction from 1 to 5 is same with the cases of Figs. 27 and 28.

$f_i(\psi,\delta)\,f_j(\psi,\delta)$; that is, the final level deduced by applying the direction finding operation, P_{Dij}, corresponds to signal components P_S given by Eqs. (50) and (51), is expressed by

$$\begin{aligned} P_{Dij} &= \frac{1}{2}P_S f_i(\psi,\delta)\,f_j(\psi,\delta) \\ &= \frac{1}{2}P_S\Big\{\frac{1}{2}[\cos(\Phi_i+\Phi_j-2\psi)+\cos(\Phi_i-\Phi_j)] \\ &\qquad \cdot\cos\xi_i\cos\xi_j\cos^2\delta \\ &\qquad +[\cos(\Phi_i-\psi)+\cos(\Phi_j-\psi)] \\ &\qquad \cdot\cos\xi_i\cos\xi_j\cos\delta\cdot\sin\delta \\ &\qquad +\sin\xi_i\sin\xi_j\sin^2\delta\Big\}, \end{aligned} \tag{110}$$

where $\Phi_i=\Omega_e t+\psi_{ob}$, and $\xi_i=\lambda_{ob}-\theta_{ai}$.

The values of ARSL have been deduced as the average level of the FFT results for seven nights of observation for five hours each night; then the average of P_{Dij} is given by

$$\langle P_{Dij}\rangle=\frac{1}{7T}\sum_{n=1}^{7}\int_{t_n}^{t_n+T}P_{Dij}dt. \tag{111}$$

In Fig. 28, the value of $\langle P_{Dij}\rangle/E_0^2$ is plotted taking E_0^2 to be constant for five cases of (ψ,δ) centered on the direction of Sgr A*. That is, when the right ascension and the declination of Sgr A* are given, respectively by ψ_{Sgr} and δ_{Sgr}, the offset directions given by the right ascension $\psi_{Sgr}\pm\Delta\psi$, and the declination $\delta_{Sgr}\pm\Delta\delta$ are expressed here by $(\pm\Delta\delta,\pm\Delta\psi)$. The directions that deviate from the direction of Sgr A* by 0.141° to NE, SE, SW, and NW are expressed by $(+0.1^\circ,+0.1^\circ)$, $(+0.1^\circ,-0.1^\circ)$, $(-0.1^\circ,-0.1^\circ)$ and $(-0.1^\circ,+0.1^\circ)$ respectively. We noticed that the radio waves with sources distributed homogeneously, in the sky are detected in an asymmetrical fashion as if the existing sources are biased in the eastward direction. The real source direction distributed in the sky is then expressed as the differences from this reference level as indicated by the black curves in Fig. 28. In Fig. 29, the ARSL values for the assumed source distributions that can be expressed by a function as

$$P_S=E_0^2[1+K\cdot\delta(\boldsymbol{k}-\boldsymbol{k}_{Sgr})], \tag{112}$$

where $\boldsymbol{k}_{Sgr}$ and K are the wave number vector of radio waves from Sgr A* and the ratio of the source power relative to the background sky noise, respectively are expressed again as $\langle P_{Dij}\rangle/E_0^2$. By comparing with the observations illustrated in Fig. 28, we conclude that the observations with 0.1° resolution indicate that the source of radio wave pules is definitely located in the direction of Sgr A* with a power level 0.7% of the background noise level.

9. EXISTENCE OF BINARY BLACK HOLE AT THE CENTER OF OUR GALAXY

9.1 Method of deducing the black hole mass and the rotation parameter

The decameter wavelength radio wave pulses of the present study are by no means an oscillation phenomena of a plasma cloud, but related to the celestial spins and orbital motions. This comes from the steady nature of the spectra of the time varying phenomena. In the present work, we attribute the generated time varying phenomena to the rotation of Kerr black holes where the intensity of the radio wave emission depends on the longitudinal inhomogeneous radiation near the regions of the event horizon of the Kerr black holes. Furthermore the spectra are characterized by frequency modulations suggesting orbital motion of a binary

doi:10.5047/978-4-88704-171-4

Kerr black hole system as descibed in Sec. 7. Based on the parameters used to interpret the spectra whose source position is within the resolution limit of 6 arc minutes at Sgr A* (see Sec. 8), we deduced the physical parameters of the black hole binary system at the Galactic center.

Let us describe the rotation periods, masses, Schwarzschild radius, radius of the event horizon, and rotation parameters as T_i, M_i, r_{gi}, r_{Ei} and a_i respectively where the suffix i (only restricted in this section), stands for a and b for the black hole Gaa and Gab respectively. The first basic relation is an expression of the event horizon that is given by

$$r_{Ei} = \frac{r_{gi} + \sqrt{r_{gi}^2 - 4a_i^2}}{2}. \tag{113}$$

Because we assume that the decameter radio waves are generated in the region extremely close to the event horizon, the rotation period T_i is strictly related to the radius of the event horizon r_{Ei}, as $(2\pi/T_i) = ca_i/(r_{Ei}r_{gi})$. Then, coupling with Eq. (113) the rotation parameter is expressed, after a mathematical manipulation, and normalized by the Schwarzschild radius, as follows,

$$\frac{a_i}{r_{gi}} = \frac{2A_i}{4A_i^2 + 1} \tag{114}$$

where

$$A_i = \left(\frac{2\pi G}{c^3}\right)\frac{M_i}{T_i} \tag{115}$$

with gravitational constant G and speed of light c.

The mass M_i can be deduced in the present binary system from the dynamics of the orbital motion by assuming circular orbits which are in a plane surface coinciding with line of the sight. That is, the total mass of the two Kerr black holes co-rotating with the orbital period T_{cm} is expressed with Kepler's law as

$$(M_a + M_b) = \frac{1}{G}\left(\frac{2\pi}{T_{cm}}\right)^2 (r_a + r_b)^3. \tag{116}$$

When we assume the situation is close to the critical rotation of Kerr black holes, i.e., $a_i = 0.5r_{gi}$, it follows, from Eqs. (114) and (115), that

$$r_{gi} = \frac{cT_i}{2\pi} \qquad \text{or} \qquad M_i = \frac{c^3}{4\pi G}T_i. \tag{117}$$

Because centrifugal forces for orbiting the two Kerr black holes balance with the common gravitational force, it follows that

$$M_a\left(\frac{2\pi}{T_{cm}}\right)^2 r_a = M_b\left(\frac{2\pi}{T_{cm}}\right)^2 r_b. \tag{118}$$

From Eqs. (117) and (118) we find the ratio R which determine the individual masses and orbiting radius; that is:

$$\frac{M_a}{M_b} = \frac{T_a}{T_b} = \frac{r_b}{r_a} = R. \tag{119}$$

Then once we know the orbiting velocities of Gaa and Gab that are expressed by v_a and v_b, respectively, the individual masses and radius of the orbits of the binary are given by

$$M_a = \frac{1}{G}\left(\frac{2\pi}{T_{cm}}\right)^2 (r_a + r_b)^3 \frac{R}{(1+R)}, \tag{120}$$

and

$$M_b = \frac{1}{G}\left(\frac{2\pi}{T_{cm}}\right)^2 (r_a + r_b)^3 \frac{1}{(1+R)} \tag{121}$$

with

$$r_a = \frac{v_a T_{cm}}{2\pi} \qquad \text{and} \qquad r_b = \frac{v_b T_{cm}}{2\pi}.$$

9.2 Results of deduced black hole parameters

In Sec. 7, the recovery of the real pulse forms from the deduced spectra of the decameter radio wave signals has been described using simulations where the parameters show a black hole binary system where black hole Gaa and Gab are spinning with the given orbital motions. In Sec. 7, also the searching processes are described for the parameters of the motions and masses that fit the results of FFT analyses for four sets of observation data from GA1 to GA4; we concluded that these four series of data have a definite average feature that can be considered an intrinsic feature. Then we searched the parameters to fit the observations taking the average spectra of the four spectra corresponding to the data series GA1, GA2, GA3, and GA4.

For principal 11 parameters in total both for Gaa and Gab such as orbital period, spin periods, and orbital velocity and amplitudes of each higher harmonics of the spectra, search for best fitting cases by 177,147 ($= 3^{11}$) trial of the simulations have been carried out starting from initial values that are estimated from observed spectra of FFT results. In addition to the principal parameters the phases of each harmonic show details of the spectra. Though the selection of the combination of the phases of higher harmonics sensitively affect the recovered pulse form, the phase values do not affect the physical quantities such as deduced mass, radius of black hole, orbital radius of the binary, and speeds of the orbital motion, and thus we have separated the search processes from the processes of the principal parameters. Then, we selected four cases of phase combinations out of a search of 4096 trials to find fitting simulated functions. The combination M(4, 4, 5, 8, 5, 3) (see Sec. 7) provides one of the best fitting simulated function. Through the processes of the evaluation, then, the parameters have been selected as given in Tables 9 and 10.

For the binary black hole the spin periods of the larger member, Gaa, and of the smaller member, Gab, are 173 ± 1 sec and 148 ± 1 sec respectively. The simulations give an orbiting period of 2200 ± 50 sec with velocities for Gaa and Gab as $(5.40 \pm 0.15) \times 10^4$ km/sec and $(6.31 \pm 0.03) \times 10^4$ km/sec respectively assuming circular orbits. The radii of orbits of Gaa and Gab are $(1.89 \pm 0.04) \times 10^7$ km and $(2.21 \pm 0.05) \times 10^7$ km respectively. Then, the average R

doi:10.5047/978-4-88704-171-4

Table 9. Spin And Orbiting Parameters of Gaa and Gaa Binary System.

	Gaa Spin Period (sec)	Gab Spin Period (sec)	Gaa Vel. (cm/s)	Gab Vel. (cm/s)	Gaa-Orbit Radius (cm)	Gab-Orbit Radius (cm)
Case1	1.72E+02	1.48E+02	5.40E+09	6.28E+09	1.89E+12	2.20E+12
Case2	1.73E+02	1.48E+02	5.40E+09	6.31E+09	1.89E+12	2.21E+12
Case3	1.74E+02	1.48E+02	5.40E+09	6.35E+09	1.89E+12	2.22E+12
Aver.			5.40E+09	6.31E+09	1.89E+12	2.21E+12
S.D.			0.00E+00	2.98E+07	0.00E+00	1.04E+10

Table 10. Deduced Back Hole Masses.

(Unit: Solar Mass)

	Gaa Mass	Gab Mass	Total Mass
Case1	2.24E+06	1.93E+06	4.18E+06
Case2	2.27E+06	1.94E+06	4.22E+06
Case3	2.30E+06	1.96E+06	4.25E+06
Aver.	2.27E+06	1.94E+06	4.22E+06
S.D.	2.23E+04	9.89E+03	3.22E+04

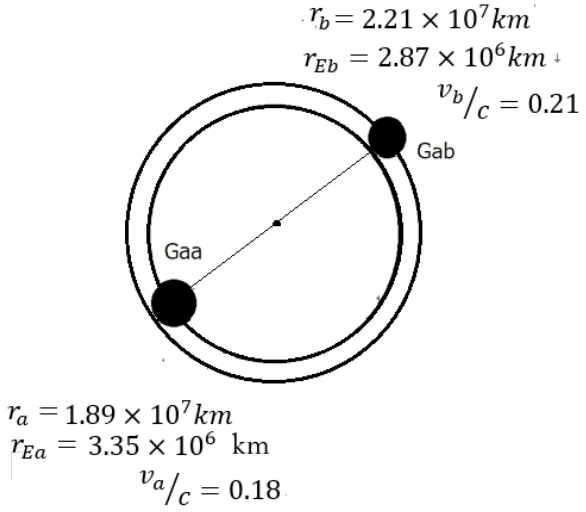

Fig. 30. An image of the orbits of the binary black holes Gaa and Gab based on the deduced parameters which are discussed in the Subsec. 9.2. The labels r_a, r_{Ea},and v_a are for the orbit radius, radius of the event horizon and orbiting velocity of Gaa, respectively; and r_b, r_{Eb}, and v_b are for the orbit radius, radius of the event horizon and orbiting velocity of Gab, respectively. The numerical value of labels are indicated only for the represented one.

value defined by Eq. (119) is 1.168; therefore, the mass is $(2.27 \pm 0.02) \times 10^6 M_\odot$ for Gaa and $(1.94 \pm 0.01) \times 10^6 M_\odot$ for Gab, assuming the orbital plane parallel to line of sight.

In Fig. 30, an image of the orbiting binary Gaa and Gab is depicted assuming a circular orbits which are looked down from the direction of the normal of the orbiting plane taking the size of each event horizon of member black holes to correspond to deduced masses with rotation parameters that are discussed in the next Subsec. 9.3.

9.3 Deduction of the rotation parameters and masses of Gaa and Gab

From Eq. (114) with Eq. (115), the rotation parameters normalized by the Schwarzschild radius are deduced using the observed spin periods and the deduced masses of Gaa and Gab; i.e., the values for Gaa and Gab are indicated by almost equal quantity, 0.490. This value is consistently acceptable because the value is close enough under the assumption of maximum rotation as $a_i/r_g = 0.5$.

Following the results in Subsec. 9.2, the total combined mass for Gaa and Gab is $(4.21 \pm 0.03) \times 10^6 M_\odot$. There are several research groups monitoring the stellar orbits surrounding Sgr A* in the quest for a possible black hole. The latest reports of the group give $(4.31 \pm 0.42) \times 10^6 M_\odot$ (Gillessen *et al*., 2009) and $(4.28 \pm 0.31) \times 10^6 M_\odot$ (Gillessen *et al*., 2017). Such a close coincidence with the results of present work cannot be expected a priori because of differences in the approach. The total mass of the present work coincides extremely well with the results of the stellar monitoring works, thus indicating the inclination of the orbital plane of the binary system could be less than 10 degrees from the line of sight between the Sun and Sgr A* implying that the system is in the general plane of our Galaxy.

10. DISCUSSIONS

10.1 Generation and Propagation of Decameter Radio Wave in the Region Close to the Event Horizon

10.1.1 Plasma environment in the region close to the event horizon of the Kerr BH's

The plasma density and magnetic field intensity have been discussed based on observation of the transport of the plasma and magnetic fields within 0.1 pc surrounding the possible black holes in Sgr A*. The falling rate of the plasma and gas into a central black hole has been discussed using Bondi's first estimation of $dM/dt = 10^{-3} M_\odot$/year (Bondi and Hoyle, 1944). Based on observations of the total radiation energy of the electromagnetic waves, the proposed rates of transport into the black holes are somewhat lower than Bondi's first estimation, now indicating a range from $10^{-4} M_\odot$/year to $10^{-8} M_\odot$/year (Melia, 1994; Narayan, 1998; Inayoshi *et al*., 2018). Authors who discussed the accretion rate of the plasma and gas into the center of our

doi:10.5047/978-4-88704-171-4

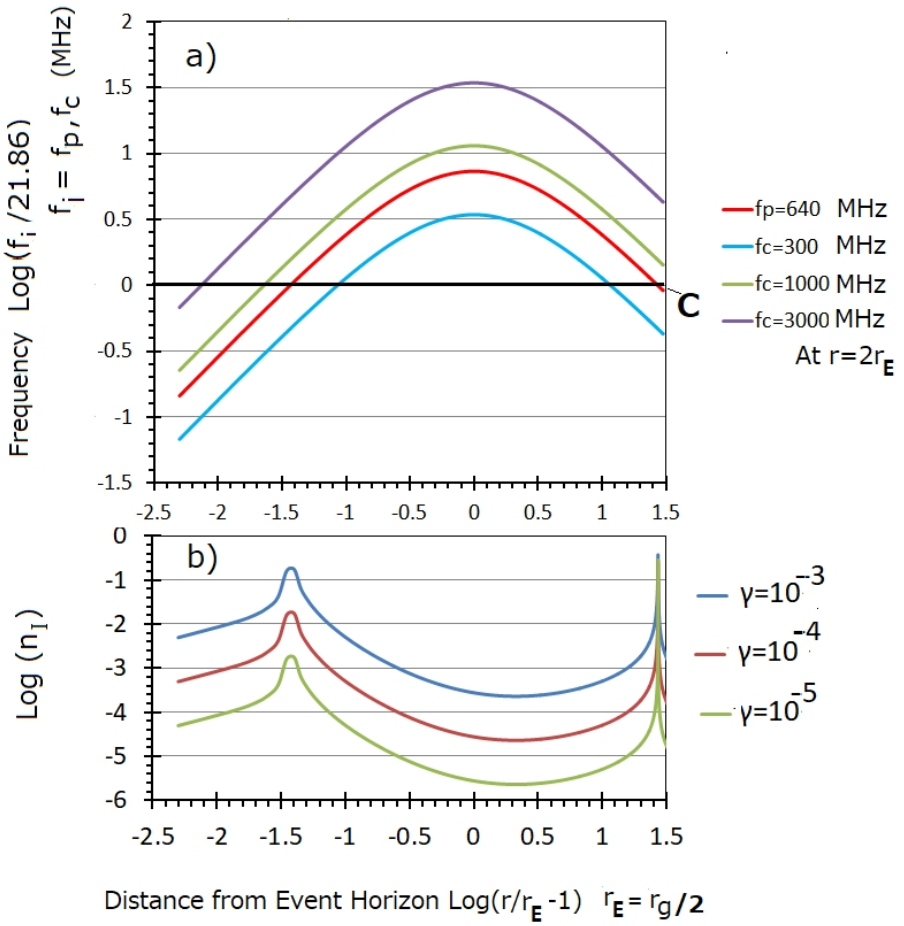

Fig. 31. Panel a) Plasma and electron cyclotron frequencies versus the position outside and close to the event horizon of a Kerr BH, which is expressed by logarithmic function starting from the event horizon. Frequencies are given by ratio to the observation frequency at 21.86 MHz plotted as a Log function. For three cases of the cyclotron frequency and one case of the plasma frequency. Panel b) Growth rate given by Log n_I (see Appendix E and Eq. (E.10) for n_I) for three example cases of the rate of the momentum transfer from the electron beam to the generated wave.

Galaxy pointed out the homogeneous nature for the low luminosity of the center region of our Galaxy. The studies using mm wavelength radiation especially have a tendency to require a tenuous feeding rate from $10^{-8}M_\odot$/year to $10^{-9}M_\odot$/year. We propose that the mechanism for the low luminosity of radiation, for the case of the close binary, may differ from the case of single black hole. Plasma falling in is not so tenuous as the rate that is extremely lower than Bondi's limit. From this standpoint then, we have selected $10^{-5}M_\odot$/year that is close to the upper limit. In this case the plasma number density, in the region close to the event horizon (RCEH hereafter) takes the value $5.10 \times 10^9/cc$ if we could observe in the coordinate transformed to Minkowski space time corresponding to the regions close to the event horizon. The corresponding plasma frequency is then about 640 MHz when we measure in the coordinate transformed to the Minkowski. space time again.

Plasmas that flow into the black hole carry magnetic fields into RCEH keeping the total magnetic flux approximately constant. When we apply a possible magnetic field intensity of 10^{-5} to 10^{-4} G in the region 0.1 pc around the black hole binary, as a representative case, the magnetic field intensity can be estimated to a range from 170 G to 1700 G in RCEH of the each member of the black hole binary also in the coordinate transformed to Minkowski space time there. This estimate of magnetic field intensity does not diverge from the magnetic field intensity observed from Faraday rotation using pulsar radio waves which propagate across the accreting disc (Eatough *et al.*, 2013). The electron cyclotron frequency goes from about 300 MHz to 3000 MHz again transforming to Mikowski spacetime. In RCEH, the dependence of the plasma number density and the magnetic field intensity versus the radial distance r become different; the plasma density can be thought as controlled by gravity while the magnetic fields are affected by currents in the accreting disk; and we consider the equipartition of the magnetic field energy density with kinetic and gravitational energy following Melia (1994). Then we assume the values of plasma number density $N(r)$ and magnetic field intensity $B(r)$ in the coordinate transformed to Minkowski space are given by

$$N(r) = N_0 \left(\frac{2r_E}{r}\right)^2, \tag{122}$$

doi:10.5047/978-4-88704-171-4

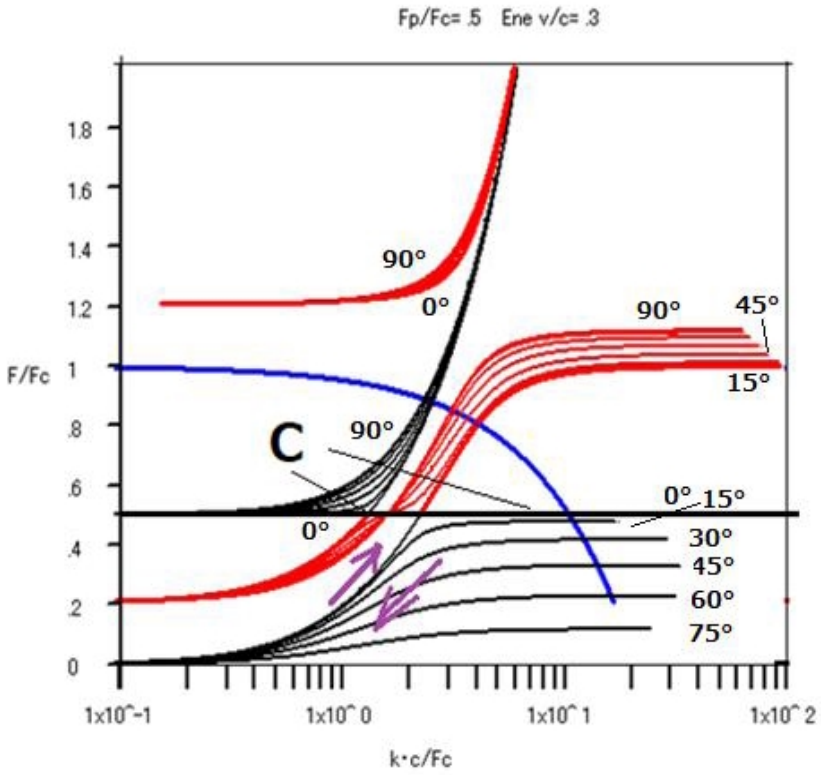

Fig. 32. Dispersion curves ($\omega - k$ relation of plasma waves) in the region close to the event horizon (RCEH) of the black hole being transformed to Minkowski space time. The curves have been calculated following Appleton Hartree equation for real part of refractive index taking the angle between the wave normal and magnetic field as parameter that is set to take 15-degree step between a range from 0 degree to 90 degree. For this selected plasma condition, $f_p/f_c = 0.3$, whistler mode waves are given in the frequency range $f < f_P$. The O mode waves which vary naturally to radio waves escaping into free space is tightly bound with the whistler mode waves in the frequency close to $f = f_p$ that is indicated by C in the dispersion diagram. The waves originally generated as the whistler mode waves in the domain close to $f = f_p$ shift towards bottom side of the diagram in the direction of the downwards going arrow while the waves propagate in the media where f/f_c become lower with increasing r. After passing through $r = 2r_E$ the waves keep propagating in the media where f/f_c become higher with increasing r until arriving at C ($f = f_p$). At this point the whistler mode waves are effectively converted to the O-mode waves that can escape outside of the black hole freely.

and

$$B(r) = B_0 \left(\frac{2r_E}{r}\right)^{5/4}, \tag{123}$$

where N_0 are B_0 plasma density and the magnetic field intensity at the position $r = 2r_E$; and r_E is the radius of the event horizon that is given as $r_E = r_g/2$, where $r_g = 2GM/c^2$, for the case of the maximum rotation (see Subsec. 9.2) which is the case of the present observations.

As explained in Appendix D in detail, the frequency f_M observed in Minkowski space time is converted to frequency f_K in the Kerr black hole, in RCEH, as,

$$f_K = f_M \left(1 - \frac{r_E}{r}\right). \tag{124}$$

The plasma frequency and electron cyclotron frequencies are converted to the values in RCEH as shown in Fig. 31 where the converted frequencies are indicated in terms of the logarithmic ratio to the frequency 21.86 MHz that we have observed. The points where curves cross the 0 line are, therefore, significant positions because the value matches the observed 21.86 MHz.

When we assume $f_c = 3000$ MHz at $r = 2r_E$ the coincidence point is at $r = 1.016r_E$. As we will discuss in next Subsec. 9.1.2, the generated wave with frequency 21.86 MHz at $r = 1.016r_E$ should propagate through the media at a frequency much less than the local plasma frequency; that is, as shown in Fig. 32, the wave should propagate under the condition $f_p/f = 6.3$ ($f_p > f$) when passes at region $r = 2r_E$. The process is only feasible when the waves take the form of whistler mode waves.

10.1.2 Generation of decameter radio waves due to wave particle interaction

The source of the decameter radio wave in RCEH of the Kerr black hole can be assumed as a plasma wave particle interaction caused by electrons falling towards black hole through the magnetized ambient plasma. The most feasible generation process can then be considered as a wave particle interaction between whistler mode waves. Because there is no place for effective reflection of radio waves in RCEH, the generated waves should propagate directly outward. The wave particle interaction therefore should take place as counter motions between outgoing waves and inward falling electrons. The exchange of energy in the counter moving state of the waves and particles is only possible be-

doi:10.5047/978-4-88704-171-4

tween spiraling electric fields and spiraling electron beams under the control of ambient magnetic fields, as is the case of the cyclotron resonance that is described for the angular frequency ω and wavenumber vector $\boldsymbol{k}$ as:

$$\omega + \boldsymbol{k} \cdot \boldsymbol{V} = \Omega_c, \tag{125}$$

where $\boldsymbol{V}$ and Ω_c are electron beam velocity and angular electron cyclotron frequency respectively.

In Fig. 32, the dispersion relation that is expressed as f/f_c versus $k \cdot c/f_c$. ($f_c = \Omega_c/2\pi$) for the electromagnetic waves in plasma following the Appleton-Hartree's equation is displayed for plasma condition $f_p/f_c = 0.5$. The relation given by Eq. (125) is also displayed in Fig. 32 for the case $V/c = 0.3$ with a blue curve. The crossing points between the blue curve and dispersion curves given by black and red plots become candidates for the generation of the radio waves.

Since the first work of Storey (1953) on propagating electromagnetic waves in space, studies on whistler mode waves became subjects, attracting interests in the fields of the electromagnetic waves in magnetized plasma, in the middle of the 20th century. Though the possibility of the existence was tacitly indicated by Appleton-Hartree's equation (Appleton, 1932; Hartree, 1931), the experimental confirmation of the VLF wave was an epoch-making step. It expanded studies on the whistler and whistler mode VLF waves that are clearly generated in the space with magnetized plasma surrounding the Earth as in the polar region upper atmosphere and inner magnetosphere. Whistler mode waves of natural origin such as the aurora hiss and dawn chorus (e.g., Helliwell, 1967) were explained through wave particle interaction where the helical motion of the electron resonates with the helically varying electric and magnetic fields of the whistler mode waves. Through a series of works (e.g., Kennel and Petschek, 1966; Gurnett and Frank, 1972; Demekhov, 2010) we may say that the understanding of physics of the whistler mode waves is completed at present in so far as the linear wave regime.

After the works that had pointed out the key processes of the wave particle resonance of helically moving electrons (Bell and Buneman, 1964; Brice, 1964), a basic studies on whistler wave generation had been presented by Kennel and Petschek (1966) indicating coherent generation of the VLF waves. That is; the primary generation mechanism is due to the coherent generation of the whistler mode waves rather than the ensemble of the cyclotron emissions from individual electrons. This coherent mechanism due to a group of electrons has been described using a velocity distribution function in the form of the kinetic theory of plasma waves where the shape of the function of the electron velocity distribution deviating from the Maxwell function has the key role to generate the whistler mode waves. Instead of the employ of the kinetic theory of plasma, we, here, employ a simple model where the waves described in a cold plasma interact with the helical beam which coherently injects the momentum of the particle motion into the wave fields. We describe this harmonic momentum transfer model for generating whistler mode waves in Appendix E.

We describe effective wave particle interaction processes in the regime of the whistler mode wave in Minkowski spacetime which is transformed from the Ker Black hole spacetime in RCEH; the wave with field strength $F(r', t')$ then starts to propagate in RCEH with following form given by,

$$F(r', t') = F_0(r'_0, t'_0) \exp\left[i\omega\left(dt' - \frac{n_R}{c}dr'\right)\right] \cdot \exp\left[2\pi \cdot n_I\left(\frac{dr'}{\lambda}\right)\right] \tag{126}$$

where $t' = t'_0 + dt'$ and $r' = r'_0 + dr'$ are time and radial distance from the black hole center, respectively when transformed into the Minkowski coordinate system and spacetime; ω, λ, n_R, and n_I are the angular frequency, wavelength in vacuum, real part of the refractive index, and imaginary part, respectively. By considering the transformation between the Kerr black hole spacetime (see Appendix E for details), that is given by

$$dt' = \left(1 - \frac{r_g}{2r}\right)dt,$$

and

$$dr' = \frac{1}{1 - \frac{r_g}{2r}}dr, \tag{127}$$

the generated and propagating radio waves are expressed in RCEH of the Kerr black hole by

$$F(r, t) = F_0(r_0, t_0) \cdot \exp\left\{i\left[\omega\left(1 - \frac{r_g}{2r}\right)dt - \frac{n_R}{c} \cdot \frac{1}{1 - \frac{r_g}{2r}}dr\right]\right\} \cdot \exp\left[2\pi \cdot n_I \frac{dr}{\lambda\left(1 - \frac{r_g}{2r}\right)}\right] \tag{128}$$

where r and t are given by $r = r_0 + dr$ and $t = t_0 + dt$, respectively.

As given in Appendix F, $n_I dr'/\lambda$ takes the plus value always to make the wave grow when there are effective wave particle interactions due to plasma falling towards the black hole. As indicated by the resonance condition given in Fig. 32, the effective wave particle interaction takes place near the local plasma frequency (see the crossing of the blue line with dispersion curves). By considering the observational frequency, we can find the relation, as,

$$21.86\ (\mathrm{MHz}) = \kappa f_p\left(1 - \frac{r_g}{2r}\right) \tag{129}$$

where κ is an arbitrary constant ranging $1 > \kappa > 0$ that is decided by the condition of the wave particle resonance. It may be selected close to $\kappa = 1$ where wave growth rate become close to maximum as has been indicated in panel b) of Fig. 31. That is, we can see a concrete example when the waves are generated with a high growth rate near the region $\kappa = 1$, which satisfies Eq. (129). Taking $f_p = 640$ MHz in the corresponding Minkowski spacetime as has already

doi:10.5047/978-4-88704-171-4

been discussed, the radio wave emission at 21.86 MHz is generated in the range $1.035r_E < r < 1.039r_E$ which corresponds to the range $0.9 < \kappa < 1$ where r_E is the position of the event horizon of the Kerr black hole; i.e., $r_E = r_g/2$.

10.1.3. Propagation of the Decameter Radio Waves through the Plasma Environment Outside of the Black Hole

Currently it has not been familiar in the field of radio astronomy, that radio waves with a frequency lower than the local plasma frequency can propagate outward from the dense plasma region. However, this is the case for the decameter radio waves propagating from the center region of our Galaxy where the space is filled with a highly energetic dense plasma. It has been confirmed, theoretically and experimentally, in the field of solar system plasma physics, that a mode conversion of radio waves takes place in the regime of space plasma waves (Oya, 1971, 1991; Jones, 1976; Okuda *et al*., 1982). Mode conversion between O-mode waves, Z-mode waves, and whistler mode waves in magnetized plasma, which are able to propagate in the plasma media with a frequency lower than the local plasma frequency has been reported by satellite observations in the Earth's aurora plasma region (Beghin *et al*., 1989). The rationale of the conversion processes between the O-mode waves and whistler mode waves was confirmed theoretically by Layden *et al*. (2011).

We then extend the concept of conversion of whistler mode waves to O-mode waves which can escape into free space as regular radio waves. There are two stages in the varying plasma environment when the generated waves, in a frequency range close to local plasma frequency, with form of whistler mode waves propagate from RCEH toward the outside of the black hole. The first stage is where the local plasma frequency and electron cyclotron frequency increase above the frequency of the propagating waves (FPW hereafter) mainly due to variation of the curvature of the relativistic spacetime corresponding to the distance from the event horizon (see Fig. 31 where FPW is given by a thick black straight line at ordinate 0). The second stage is where the local plasma frequency and the electron cyclotron frequency become lower than FPW, in regions of almost flat spacetime, as a function of distance outward of the black hole environment.

In the first stage of the propagation, between $\mathrm{Log}(r/r_E - 1) = -1.5$, i.e., $r = 1.031r_E$ and $\mathrm{Log}(r/r_E - 1) = 0$ corresponding $r = 2.0r_E$, the local f_p and f_c increase; therefore, the f/f_c value decreases as when we plot the point in Fig. 32. It is indicated by a locus with a down going arrow that corresponds to keeping the propagation in the form of the whistler wave mode. After passing the point $r = 2.0r_E$ the propagation of the wave enters the second stage where the local f_p and f_c start to decrease with increasing r. The f/f_c value then increases with increasing r. This second stage propagation is plotted as a locus with up going allow on the dispersion curves of whistler wave mode in Fig. 32.

The whistler wave mode that keeps going outward (in the direction of increasing r) eventually arrives at the point where FPW becomes the same with the local f_p as indicated with the point C in both Figs. 31 and 32 where the energy of whistler wave mode converts at a fairly high rate into the O mode electromagnetic wave. The O-mode wave (now called radio wave) is naturally connected to the electromagnetic wave in a vacuum or extremely tenuous plasm with a weak magnetic field as is the case of the propagation in the interstellar space; i.e., the radio wave can smoothly escape into Galactic space to arrive at the observation points on the Earth's surface.

10.2 Feasibility of existence of the close binary black holes

The righteousness of the result of the present study which conclude the existence of the close binary whose parameters are given in Tables 8 and 9 in Sec. 9 is strictly depend on the truth of the generation mechanism of the gravitational waves from the black holes that extract tremendous energy from orbiting objects. We understand in so far as we follow the present day established method of calculation for binary of the compact objects, two black holes in the orbits with masses that are concluded by the present work merge within a few hours. Instead of abandoning the results of the present studies, however, we select here to investigate the propagation situation of the gravitational waves inside of the event horizon. It is evident, in the current studies of the gravitational waves from the black holes, that no constraint is given for the spacetime of propagating media but only consider the generation processes of the gravitational waves. Significance for the environmental condition is the assumption of the week background gravitational field so as the gravitational wave intensity can be treated as perturbation from the Minkowski spacetime following the Einstein's first approach (eg. Blanchet *et al*., 1995).

We consider the generation and propagation of the gravitational waves in a frame of the Minkowski spacetime which is transformed corresponding to the black hole spacetime; this means that we never assume weak gravitational field but observe the generation and propagation processes of the gravitational waves at the frame making free fall following the local gravitational field. Therefore, real feature of the propagation of the gravitational waves in the real black hole spacetime can deduce by transformation between the Minkowski spacetime without weak field assumption. Within the inside region of the Karr black hole, there exists sufficient vacuum region between the event horizon and material body of the black hole; in this vacuum region the generated gravitational waves propagate with form in Minkowski spacetime corresponding black hole spacetime as

$$G = \sum_p G_p(r') \exp[i(\omega \cdot t' - k \cdot r')] \qquad (130)$$

where $G_p(r')$ is the representative amplitude of the gravitational waves for all possible polarization modes at the local place r'; and ω and k are the angular frequency and wave number of the gravitational wave that give $(\omega/k) = c$. The propagation velocity can be deduced from the relation to trace the point of a constant phase of the wave as,

$$\omega \cdot dt' - k \cdot dr' = 0. \qquad (131)$$

doi:10.5047/978-4-88704-171-4

When we rewrite the propagating wave in the black hole spacetime by applying the transformation given by Eq. (127) extending to the inside region of the event horizon (also see Eq. (E.16), in Appendix E), the outgoing wave which approaches to the event horizon from the inside of the event horizon with the propagation condition equivalent to Eq. (131), is transformed as (see Appendix E for r_1 and t_1),

$$\omega\left(\frac{r_g}{2r_I}-1\right)dt_1-\frac{k}{\frac{r_g}{2r_I}-1}dr_1=0. \qquad (132)$$

Then the propagation velocity V is given by:

$$\frac{dr_1}{dt_1}=V=\left(\frac{\omega}{k}\right)\left(\frac{r_g}{2r_I}-1\right)^2=c\left(\frac{r_g}{2r_I}-1\right)^2. \qquad (133)$$

When the gravitational waves approach the event horizon ($r_I \to r_E = r_g/2$) then $V = 0$. We should state that the gravitational wave generated inside the event horizon has no way to avoid the passage that crosses the event horizon where the propagation speed becomes zero. That is, from the black hole which is associated with the event horizon, no gravitational wave comes out.

The LIGO achievement of the first direct detection of a gravitational wave is highly admirable; but the claim of the LIGO team (Abbott *et al.*, 2016(a), 2016(b), 2017(a), 2017(b)) that has concluded the origin of the source of the observed gravitational waves to be black hole mergers is not the matter of observational confirmation. There remain questions whether the objects with mass range from $7M_\odot$ to $36M_\odot$ are black holes or compact stars without event horizon. In 2016 a paper was published pointing out the possibility of a different merger model for the LIGO result by stating "Did GW150914 produce a rotating gravastar?" (Chirenti and Rezzolla, 2016). Though their conclusion is not negative for black hole merger from analyses of gravitational wave signature, we still think that it is important to consider the black hole mimic which has no event horizon, not necessarily restricting to the arguments of the gravitational condensation star, "gravastar" (Mazur and Mottola, 2001, 2004; Pani, 2015; Uchikawa *et al.*, 2016). The studies on the compact star whose compactness is equivalent to the black hole but the boundary of the material is a little lager than the possible event horizon deduced from the vacuum condition of the Einstein equation are deferred for future.

11. CONCLUSION

The present quest for a possible black hole in the region of Sgr A* has been pursued by observing the relatively low frequency radio wave at 21.86 MHz by using decameter wave length radio waves observed by the long base line interferometer system of Tohoku University with baseline lengths of 44 km to 83 km. Observations were made in 2016 June and 2017 June during periods when we could aim at the Galactic center. To verify the existence of specific signals from the Galactic center, observations using the same system were made in 2016 and 2017 from December to January when we detected the noise characteristics of the background sky without the Galaxy center in the sky.

By accumulating results of FFT analyses for 2016 sets of independent time series from observed data, we detected spectra that revealed the pulse components that show a level of a few percent above the averaged background noise level with an accuracy of 2 to 3σ where σ is the standard deviation. The detected spectra show the features of an ensemble of signals from multiple sources which emit radiation modulated by rotation of the sources. The timing and shapes of the detected pulses coincide with emissions from the multiple rotating sources. The variations in intensity of the radio waves, associated with higher harmonic components suggested by shape of the pulses, are thought to reflect the azimuthal dependence of the electromagnetic and plasma environment of the rotating objects.

Based on the observed interferometer data we analyzed the direction of the source. To find the arrival direction of the detected pulse, we utilized unique method for operation of the interferometer by modifying orthodox method for aperture synthesis utilizing the earth's rotation. We call this method "Interferometer Fringe Function Correlation Method (IFFCM)"; as equivalent concept to the inverse Fourier transformation that is essential for the processes of the aperture synthesis, we apply template fringe function; by finding the maximum point of the correlation between the observed interferometer fringe and the artificially generated template fringe the source direction can be identified. By generating two template fringe functions with phase shift of $\pi/2$ rad each other, we determined the direction of the source of arrival radio waves by eliminating unknown phase shifts of the system by IFFCM. Then, our method has been effectively applied to eliminate the ionosphere propagation effect that is significant for the decameter wavelength range. That is, the phase lags of arriving decameter radio waves due to ionospheric propagation effects are able to be included in the ambiguity of the phase lag of the signals at each observation station of the interferometer system. We set, therefore, a virtual interferometer system at a location on the ray path in space. The final results show, without any ionospheric disturbance, that the source of pulse spectra detected from the observations is located in the direction within ± 6 arc minutes centered at Sgr A* (at RA 17 h 45 m 40 s and Dec $-29^\circ 0' 28''$).

Detailed analyses of the timing variation of the pulses indicate the Doppler effects on the emitted pulses with a periodic variation of the pulse frequency i.e., frequency modulation on pulse frequencies suggesting orbital motions of sources. Simulation analyses have been carried out by constructing simulation functions that consist of an ensemble of sinusoidal functions containing a total of 17 parameters to express spin and orbiting motion of two black holes and emitted radio wave pulse levels with phase differences. We applied the same processes for FFT analyses with the cases of the analyses for the observational data to simulate the observational results of FFT analyses. As results, we find that there are two basic spin periods at 173 ± 1 sec and 148 ± 1 sec which correspond to two Kerr black holes named, here, Gaa and Gab respectively. Together with two inherent spin periods, there are multiples of sidebands of the spectra, around

doi:10.5047/978-4-88704-171-4

the main spectra, that are caused by the frequency modulation due to two massive black holes orbiting in binary orbits; from the frequency gap of the multiple side bands the orbiting period is decided to be 2200 ± 50 sec. From the extent of side band formation, associated with the two series of the harmonics, we find that the velocities of Gaa and Gab in binary orbits are about 18.0% and 21.4% (see Subsec. 9.2 for accurate values) of the speed of light respectively.

From two simple assumptions—circular orbits in the plane coinciding with the Galactic plane and Newtonian dynamics for the binary system—the masses of Gaa and Gab are deduced to be $(2.27\pm0.02)\times10^6\mathrm{M}_\odot$ and $(1.94\pm0.01)\times10^6\mathrm{M}_\odot$ respectively. The total mass of the system is $(4.22 \pm 0.03) \times 10^6\mathrm{M}_\odot$ which is fairly close to the newest results of the black hole mass $(4.28 \pm 0.31) \times 10^6\mathrm{M}_\odot$ at the Galactic center (Gillessen *et al*., 2017).

In the present works, six significant subjects which seem to contradict current concepts in astrophysics when we base our discussions on the firmness of the observational evidence. The six subjects are 1) the propagation of decameter radio wave pulses keep the original pulse form without being destroyed due to the plasma irregularity in Galactic space, 2) severe ionosphere refraction effects that prevent a determination of the source direction with an accuracy of a few arc minutes; 3) propagation of low frequency waves through the dens plasma environment in the center region of our Galaxy, 4) the problem of the generating radio waves in the region extremely close to the event horizon where the photon energy is shrinking due to effects of general relativity, 5) violation of the stability criteria from the standpoint of the rotational and tidal deformation effects on the objects due to perturbations from the gravitational interaction of the close binary and 6) gravitational wave generation that exhausts the potential energy which keeps the orbital motion decaying into a merger.

We accept the observational evidence, rather than following the established paradigm. For problem 1) we pointed out the importance of the observational bandwidth over the previous multipath concept where no argument was made for the correlation of pulse signals as function of the receiving bandwidth. For problem 2) we used an analysis method that is equivalent to virtually shifting the observing interferometer system into vacuum space and skipping the ionosphere effects. About problem 3) we proposed the propagation of whistler wave modes, through the magnetized plasma in the center part of our Galaxy, that eventually convert to the ordinary mode radio waves in the plasma; the mode conversion has already been confirmed in space by the satellite observations. Problem 4) is solved through wave particle interactions at the generation points where high energy plasmas are falling towards the black hole; the shrinking of the photon energy is compensated by increasing the number of the photons that are due to the exponential growth of the coherent plasma waves, The stability problem 5) is significant if the objects are regular stars where the deviation of the equipotential surfaces are remarkably skewed from a complete sphere configuration; but in the case of a Kerr black hole that is close to the maximum rotation, the possible sphere of matter inside of the event horizon could be maintaining super symmetry so that the perturbation theory for a binary star cannot be applied. But details for this subject are deferred for future studies.

Finally problem 6) is a major issue and contradicts the most widely accepted paradigm; but it raises a basic question of why the gravitational wave crosses the event horizon while no electromagnetic wave can propagate across the event horizon. We have presented an interpretation that the gravitational wave is not able to propagate across the event horizon. We have also mentioned evidence that LIGO observations of gravitational waves may relate to the merger of objects that are not associated with the event horizon. For gravity itself there may be an era in the future to investigate where the real truth lies. It may leave behind the traditionally assumed concept of the graviton and be guided by general relativity especially related to black holes. The question remains why the graviton comes out of the black hole while no photon can do the same, except for minor fractions endorsed by quantum physics regime (Hawking, 1976).

Acknowledgments. The significant core of present work is in the observation of the decameter radio wave pulses from the center of our Galaxy; observations were made with the decameter long baseline interferometer at Tohoku University. The author gives sincere thanks to Professor Y. Kato, Dr. A. Kumamoto and Dr. H. Misawa for giving the important assistance to keep system running. The author is also grateful to them for detailed discussions which have become vital encouragements to continue exploring the processes of the present work.

A part of processes of data analyses have been financially supported by Seisa University of Seisa Group, the author sincerely thanks to Mr. Y. Miyazawa the president of Seisa Group and Dr. H. Inoue the president of Seisa University for their deep understanding and support of the present study.

References

Abbott, B. P., Abbott, R., Abbott, T. D., Abernathy, M. R., Acernese, F., Ackley, K., Adams, C., Adams, T., Addesso, P., Adhikari, R. X. and 972 coauthors, *Phys. Rev. Lett*., **116**, 061102, 2016(a).

Abbott, B. P., Abbott, R., Abbott, T. D., Abernathy, M. R., Acernese, F., Ackley, K., Adams, C., Adams, T., Addesso, P., Adhikari, R. X. and 969 coauthers, *Phys. Rev. Lett*., **116**, 241103, 2016(b).

Abbott, B. P., Abbott, R., Abbott, T. D., Acernese, F., Ackley, K., Adams, C., Adams, T., Addesso, P., Adhikari, R. X., Adya, V. B. and 1100 coauthors, *Phys. Rev. Lett*., **118**, 221101, 2017(a).

Abbott, B. P., Abbott, R., Abbott, T. D., Acernese, F., Ackley, K., Adams, C., Adams, T., Addesso., P., Adhikari, R. X., Adya, V. B. and 1100 coauthors, *Phys. Rev. Lett*., **119**, 141101, 2017(b).

Appleton, E. V., *JIEE*, **71**, 642, 1932.

Beghin, C., Rauch, J. L. and Bosqued, J. M., *J. Geophys. Res*., **94**, 1359, 1989.

Bell, T. F. and Buneman, O., *Physical Review*, **133**, A1300, 1964.

Bondi, H. and Hoyle, F., *Monthly Notices of the Royal Astronomical Society*, **104**, 273, 1944.

Blanchet, L., Damour, T., Iyer, B. R., Will, C. M. and Wiseman, A. G., *Phys. Rev. Lett*., **74**, 3515.

Brice, N., *J. Geophys. Res*., **69**, 4515, 1964.

Chirenti, C. and Rezzolla, L., *Physical Review*, **D94**, 084016, 2016.

Demekhov, A. G., *R&QE*, **53**, 609D, 2011.

Eatough, R. P., Falcke, H., Karuppusamy, R., Lee, K. J., Champion, D. J., Keane, E. F., Esvignes, G., Schnitzeler, D. H. F. M., Spitler, L. G., Kramer, M., Klein, B., Bassa, C., Bower, G. C., Bruthaler, A., Cognard, I., Deller, A. T., Demorest, P. B., Freire, C., Kraus, A., Lyne, A. G., Noutsos, A., Stappers, B. and Wex, N., *Nature*, **501**, 391, 2013.

Eckart, A. and Genzel, R., *Astron. Astrophys. Suppl. Series*, **191**, 9707E, 29-1366, 1997.

Genzel, R., Eisenhauer, F. and Gillessen, S., *Review of Modern Phys*., **82**,

doi:10.5047/978-4-88704-171-4

3121, 2010.
Gillessen, S., Plewa, P. M., Eisenhauer, F., Sari, R., Weisberg, I., Habibi, M., Pfuhl, O., George, E., Dexter, J., von Fellenberg, S., Ou, T. and Genzel, R., *Astrophys. J.*, **837**, 30, 2017.
Gurnett, D. A. and Frank, L. A., *J. Geophys. Res.*, **77**, 190, 1972.
Hartree, D. R., *PCPS*, **27**, 143, 1931.
Hawking, S. W., *Phys. Review D*, **14**, 2460, 1976.
Helliwell, R. A., *J. Geophys. Res.*, **72**, 4773, 1967.
Inayoshi, K., Ostriker, J. P., Haiman, Z. H. and Kuiper, R., *Monthly Notices of the Royal Astronomical Society*, **476**, 1412, 2018.
Jansky, K., *Nature*, **132**, 66, 1933.
Jones, D., *Nature*, **260**, 686, 1976.
Kennel, C. F. and Petschek, E. H., *J. Geophys. Res.*, **71**, 1, 1966.
Ker, P. P., *Phys. Rev. Lett.*, **11**, 237, 1963.
Lacy, J. H., Townes, C. H., Gebolle, T. R. and Hollenbach, D. J., *Astrophys. J.*, **241**, 132, 1980.
Little, L. T., *PSS*, **16**, 749, 1968.
Lyden, A., Cairns, I. H., Robinson, P. A. and LaBelle, J., *J. Geophys. Res.*, **116**, A12328, 2011.
Lynden-Bell, D. and Rees, M. J., *Monthly Notices of the Royal Astronomical Society*, **152**, 461, 1971.
Lo, K. Y. and Claussen, M. J., *Nature*, **306**, 647, 1983.
Melia, F., *Astrophys. J.*, **426**, 577, 1994.
Mazure, P. O. and Mottola, E., *Physical Review*, **D64**, 104022, 2001.
Mazure, P. O. and Mottola, E., *Proc. Natl. Acad. Sci.*, **101**, 9545M, 2004.
Narayan, R., Mahadevan, R. and Grindlay, J. E., *Astrophys. J.*, **492**, 554, 1998.
Okuda, H., Ashour-Abdara, M., Chance, S. and Kuruth, W. S., *J. Geophys. Res.*, **87**, 10457, 1982.
Oya, H., *Radio Science*, **6**, 1131, 1971.
Pani, P., *Physical Review*, **D92**, 124030, 2015.
Rankin, J. M., Comella, J. M., Craft, H. D., Richards, D. W., Campbell, D. B. and Counselman III, C. C., *Astrophys. J.*, **162**, 707, 1970.
Rohlfs, K., *Tools of Radio Astronomy*, Springer, 105-112, 1986.
Serabyn, E. and Lacy, J. H., *Astrophys. J.*, **293**, 445, 1985.
Sheuer, P. A. G., *Nature*, **218**, 920, 1968.
Storey, L. R. O., *Philos. Trans. Royal Soc. Ser. A*, **246**, 113, 1953.
Uchikata, N., Yoshida, S. and Pani, P., *Physical Review*, **D94**, 064015, 2016.

Appendix A.

All symbols in this Appendix have already defined in the main text; we will not repeat them. The geometry of the ray paths and boundaries of the plasma irregularity follow the depictions in Figs. 3(a) and 3(b).

The refraction processes of Ray-1 and Ray-2 (we will express two rays as ray-α hereafter with understanding that $\alpha = 1$ and 2) take place with Snell's relation as given by:

$$\mu_{\alpha i} \sin(\theta_{Ni} - \theta_{\alpha i}) = \mu_{\alpha i+1} \sin(\theta_{Ni} - \theta_{\alpha i+1}). \quad (A.1)$$

By defining small shift angle $\Delta\theta_{\alpha i}$ for the ray-α an alternative of, Eq. (A.1) is given by:

$$\mu_{\alpha i} \sin(\theta_{Ni} - \theta_{\alpha i}) = \mu_{\alpha i+1} \sin(\theta_{Ni} - \theta_{\alpha i} + \Delta\theta_{\alpha i}). \quad (A.2)$$

We assume here that $\Delta\theta_{\alpha i} \ll \theta_{\alpha i}$. From Eq. (A.2) it then follows, after mathematical manipulation, that

$$\Delta\theta_{\alpha i} = [(\mu_{\alpha i} - \mu_{\alpha i+1})/\mu_{\alpha i+1}] \tan(\theta_{Ni} - \theta_{\alpha i}). \quad (A.3)$$

The refractive index $\mu_{\alpha i}$ and $\mu_{\alpha i+1}$ in the plasma where plasma angular frequencies are given by ω_{pi} and ω_{pi+1}, respectively are expressed by

$$\mu_{\alpha i} = \sqrt{1 - (\omega_{pi}/\omega_\alpha)^2}, \quad (A.4)$$

and

$$\mu_{\alpha i+1} = \sqrt{1 - (\omega_{pi+1}/\omega_\alpha)^2}. \quad (A.5)$$

For the case of interstellar propagation we can assume that $(\omega_{pi}/\omega_\alpha)^2 \ll 1$ and $(\omega_{pi+1}/\omega_\alpha)^2 \ll 1$; then, it follows that

$$\frac{\mu_{\alpha i} - \mu_{\alpha i+1}}{\mu_{\alpha i+1}} = \frac{1}{2}\left(\frac{\omega_{pU}}{\omega_\alpha}\right)^2 (N_{i+1} - N_i), \quad (A.6)$$

where N_i and N_{i+1} are electron number densities in i-th and $(i+1)$-th segments of the irregularities in the plasma distributed along the propagation path; and $\omega_{pU}^2 = e^2/m\varepsilon_0$, for dielectric constant of vacuum ε_0.

From Eq. (A.3), therefore, we can obtain $\Delta\theta_{\alpha i}$, as

$$\Delta\theta_{\alpha i} = \frac{1}{2}\left(\frac{\omega_{pU}}{\omega_\alpha}\right)^2 (N_{i+1} - N_i) \tan(\theta_{Ni} - \theta_{\alpha i}). \quad (A.7)$$

Because ray-α which arrive at the observation point starting from extremely long distant source is not deviate from the S–O line (see main text for definition) while the boundary normal of the plasma segments vary within arbitrary angle range, we can assume that

$$\theta_{Ni} \gg \theta_{\alpha i}. \quad (A.8)$$

Though θ_{Ni} values are in arbitrary range, we can select the i-th and $(i+1)$-th plasma segments so as the angle difference $\Delta\theta_{Ni,i+1} (= \theta_{Ni+1} - \theta_{Ni})$ to be small which can be expressed as

$$\theta_{Ni} \gg \Delta\theta_{Ni,i+1}. \quad (A.9)$$

Under this circumstance, we can rewrite Eq. (A.7) as follows

$$\Delta\theta_{\alpha i} = \frac{1}{2}\left(\frac{\omega_{pU}}{\omega_\alpha}\right)^2 [N_{i+1}\tan\theta_{Ni+1} - N_i \tan\theta_{Ni} - N_{i+1}(\tan\theta_{Ni+1} - \tan\theta_{Ni})]. \quad (A.10)$$

At this stage we further rewrite the term $\tan\theta_{Ni+1} - \tan\theta_{Ni}$ as

$$\tan\theta_{Ni+1} - \tan\theta_{Ni} = \frac{\tan\theta_{Ni} + \Delta\theta_{Ni,i+1}}{1 - \tan\theta_{Ni} \cdot \Delta\theta_{Ni,i+1}} - \tan\theta_{Ni} \approx \Delta\theta_{Ni,i+1}. \quad (A.11)$$

Plasma density of each irregularity segment N_i is expressed using average density N_a and perturbation ΔN_i, as

$$N_i = N_a + \Delta N_i. \quad (A.12)$$

Then, $\Delta\theta_{\alpha i}$ is finally expressed as

$$\Delta\theta_{\alpha i} = \frac{1}{2}\left(\frac{\omega_{pU}}{\omega_\alpha}\right)^2 [N_{i+1}\tan\theta_{Ni+1} - N_i \tan\theta_{Ni} - (N_a + \Delta N_{i+1})\Delta\theta_{Ni,i+1}]. \quad (A.13)$$

From Eqs. (A.1) and (A.2) it follows that

$$\theta_{\alpha i+1} = \theta_{\alpha i} - \Delta\theta_{\alpha i}. \quad (A.14)$$

doi:10.5047/978-4-88704-171-4

By taking summation for both side of Eq. (A.14) from $i = 1$ to $i = M - 1$ sequentially, the result is given by

$$\begin{aligned}\theta_{\alpha M} &= \theta_{\alpha 1} - \sum_{i=1}^{M-1} \Delta\theta_{\alpha i} \\ &= \theta_{\alpha 1} - \frac{1}{2}\left(\frac{\omega_{pU}}{\omega_\alpha}\right)^2 \\ &\quad \cdot \left[N_M \tan\theta_{NM} - N_1 \tan\theta_{N1} \right. \\ &\quad \left. - \sum_{i=1}^{i=M-1} (N_a + \Delta N_{i+1}) \Delta\theta_{Ni,i+1} \right] \end{aligned} \tag{A.15}$$

We can assume boundary values $\theta_{\alpha 1}$ and θ_{NM} to be zero. It can be thought as statistic characteristic of plasma irregularity that

$$\sum_{i=1}^{i=M-1} \Delta\theta_{Ni,i+1} = 0. \tag{A.16}$$

Considering that the plasma angular frequency is given by $\omega_{pM} = \omega_{pU}\sqrt{N_M}$; and considering that

$$\omega_{PM}^2/\omega_\alpha^2 \ll 1$$

for the expression

$$\begin{aligned}&\theta_{\alpha M} + \frac{1}{2}\left(\frac{\omega_{pM}}{\omega_\alpha}\right)^2 \tan\theta_{NM} \\ &\qquad = - \sum_{i=1}^{i=M-1} \Delta N_{i+1} \cdot \Delta\theta_{Ni,i+1} \end{aligned} \tag{A.17}$$

that is rewritten from Eq. (A.15), we have finally the result as

$$\theta_{\alpha M} = - \sum_{i=1}^{i=M-1} \Delta N_{i+1} \cdot \Delta\theta_{Ni,i+1}. \tag{A.18}$$

Appendix B.

In this Appendix, symbols that have been defined in Appendix A and main text will not be repeated their definition here. From statistic character of the plasma irregularity we have the relation

$$\sum_{i=1}^{\text{Max}} \Delta N_{j+1} = 0 \tag{B.1}$$

and

$$\sum_{i=1}^{\text{Max}} \Delta\theta_{Nj,j+1} = 0. \tag{B.2}$$

Then it follows, starting from Eq. (10) of main text, that

$$\theta_{\alpha\,\text{Max}} = \frac{1}{4}\left(\frac{\omega_{pU}}{\omega_\alpha}\right)^2 \sum_{i=1}^{\text{Max}} \Delta N_i \cdot \Delta\theta_{Nj,j+1}. \tag{B.3}$$

Through total paths from $i = 1$ to $i = \text{Max}$, occurrence probability of ΔN_{j+1} and $\Delta\theta_{Ni-1,i}$ follow the Gaussian function considering that ΔN_i and $\Delta\theta_{Ni-1,i}$ ($i = 1$ to $i = \text{Max}$) cover variables ΔN and $\Delta\theta$, respectively, in a range from minus infinity to plus infinity across zero. Then Eq. (B.3) is rewritten by

$$\begin{aligned}\theta_{\alpha\,\text{Max}} = \frac{1}{2}\left(\frac{\omega_{pU}}{\omega_\alpha}\right)^2 &\frac{1}{2\pi\sigma_N\sigma_\theta} \int_{-\infty}^{\infty}\int_{-\infty}^{\infty} \Delta N \cdot \Delta\theta \\ &\cdot \exp\left[-\left(\frac{\Delta N}{\sqrt{2}\sigma_N}\right)^2 \right] \\ &\cdot \exp\left[-\left(\frac{\Delta\theta}{\sqrt{2}\sigma_\theta}\right)^2 \right] d(\Delta N) d(\Delta\theta). \end{aligned} \tag{B.4}$$

From Eq. (B.4), then it follows that

$$\theta_{\alpha\,\text{Max}}^2 \equiv \theta_\alpha^2 = \frac{1}{4}\left(\frac{\omega_{pU}}{\omega_\alpha}\right)^4 \sigma_N^2 \sigma_\theta^2. \tag{B.5}$$

Appendix C.

As a general expression, we consider here two waves $A(t)\cos(\omega t - \boldsymbol{k}_\nu \boldsymbol{r}_i + \theta_\lambda + \theta_i)$ and $B(t)\cos(\omega t - \boldsymbol{k}_\mu \boldsymbol{r}_j + \theta_\mu + \theta_j)$ where the symbols are the same as in the main text. When we calculate the correlation coefficient I_{AB} for these two waves, it follows that

$$\begin{aligned} I_{AB} &= \frac{1}{T}\int_t^{t+T} A(t)\cos(\omega t - \boldsymbol{k}_\nu \boldsymbol{r}_i + \theta_\lambda + \theta_i) \\ &\quad \cdot B(t)\cos(\omega t - \boldsymbol{k}_\mu \boldsymbol{r}_j + \theta_\mu + \theta_j) dt \\ &= \frac{1}{2T}\int_t^{t+T} A(t)B(t)\{\cos[2\omega t - (\boldsymbol{k}_\nu \boldsymbol{r}_i + \boldsymbol{k}_\mu \boldsymbol{r}_j) \\ &\qquad + (\theta_\lambda + \theta_\mu) + (\theta_i + \theta_j)] \\ &\qquad + \cos[(\boldsymbol{k}_\mu \boldsymbol{r}_j - \boldsymbol{k}_\nu \boldsymbol{r}_i) \\ &\qquad + (\theta_\lambda - \theta_\mu) + (\theta_i - \theta_j)]\} dt \\ &= \frac{1}{2T}\int_t^{t+T} A(t)B(t)\left\{\cos[2\omega t - (\boldsymbol{k}_\nu \boldsymbol{r}_i + \boldsymbol{k}_\mu \boldsymbol{r}_j) \right. \\ &\qquad + (\theta_\lambda + \theta_\mu) + (\theta_i + \theta_j)] \\ &\qquad + \cos\left[\frac{1}{2}(\boldsymbol{k}_\nu + \boldsymbol{k}_\mu)(\boldsymbol{r}_j - \boldsymbol{r}_i) \right. \\ &\qquad + \frac{1}{2}(\boldsymbol{k}_\mu - \boldsymbol{k}_\nu)(\boldsymbol{r}_i + \boldsymbol{r}_j) \\ &\qquad \left.\left. + (\theta_\lambda - \theta_\mu) + (\theta_i - \theta_j)\right]\right\} dt. \end{aligned} \tag{C.1}$$

When two waves propagate with same velocity in the same direction, the correlation coefficient reaches maximum; then for $\boldsymbol{k}_\nu = \boldsymbol{k}_\mu$ and $\theta_\lambda = \theta_\mu$, Eq. (C.1) gives the maximum correlation coefficient as

$$I_{AB} = \frac{1}{2}A(t)B(t)\cos[\boldsymbol{k}_\nu(\boldsymbol{r}_j - \boldsymbol{r}_i) + (\theta_i - \theta_j)]. \tag{C.2}$$

We apply this principle, in the main text, to obtain Eq. (23) starting from Eq. (22).

doi:10.5047/978-4-88704-171-4

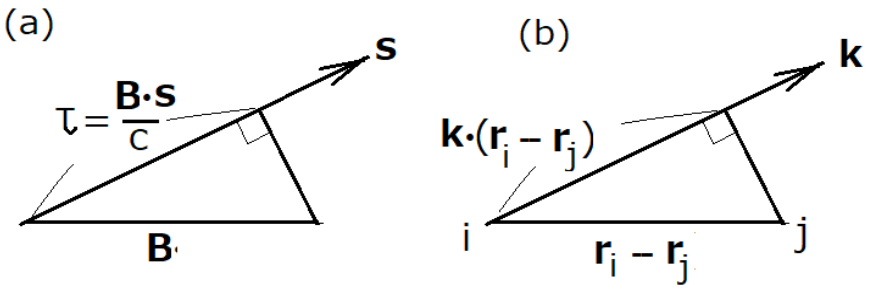

Fig. D.1. The comparison of the symbols that describe the interferometer system for aperture synthesis. (a) The symbols in OASIO; versus the source direction vector $\boldsymbol{s}$, the baseline vector is described as $\boldsymbol{B}$. The interferometer data are described with delay time $\tau = \boldsymbol{B} \cdot \boldsymbol{s}/c$, as $A(\boldsymbol{s})I(\boldsymbol{s})\exp(i\omega\tau)$. (b) The symbols in IFFCM; versus the source direction vector $\boldsymbol{k}$ where $|\boldsymbol{k}| = 2\pi/\lambda$ with wavelength λ, the baseline vector is described as $\boldsymbol{r}_i - \boldsymbol{r}_j$. The interferometer data are described with phase delay $\boldsymbol{k} \cdot (\boldsymbol{r}_i - \boldsymbol{r}_j)$ as $S_0^2(t)\exp[i\boldsymbol{k}(\boldsymbol{r}_j - \boldsymbol{r}_i)]$ where $S_0^2(t)$ is the received signal power affected by the primary antenna beam characteristic.

Appendix D.

Equivalence between IFFCM and the orthodox aperture synthesis of interferometer observation (OASIO hereafter).

As an example description of OASIO we follow the description made by K. Rohlfs (1986); then we use the same mathematical symbols as described by Rohlfs, although there are many conflicts between the symbols in the present paper. The essence of the OASIO description starts with the configuration given in panel (a) of Fig. D.1 where the definition used in the present paper is given in panel (b) in parallel. In OASIO, the mapping of the radio wave source distribution is described by introducing a vector $\boldsymbol{\sigma}$ to sweep the sky direction as:

$$\boldsymbol{s} = \boldsymbol{s}_0 + \boldsymbol{\sigma} \qquad \text{with} \quad |\boldsymbol{\sigma}| = 1, \tag{D.1}$$

where the $\boldsymbol{s}$ and $\boldsymbol{s}_0$ vectors describe the radiation source and the conveniently selected center of the source, respectively. The baseline vector is described by a vector $\boldsymbol{B}$ that is given in a Cartesian coordinate system (u, v, w) as:

$$\frac{\omega}{2\pi c}\boldsymbol{B} = u\hat{\boldsymbol{u}} + v\hat{\boldsymbol{v}} + w\hat{\boldsymbol{w}} \tag{D.2}$$

where $\hat{\boldsymbol{u}}$, $\hat{\boldsymbol{v}}$, and $\hat{\boldsymbol{w}}$ are unit vectors for the u, v, and w directions, respectively. In OASIO, they describe the total interferometer output data $R(\boldsymbol{B})$ as:

$$R(\boldsymbol{B}) = \exp\left[i\omega\left(\frac{1}{c}\boldsymbol{B}\cdot\boldsymbol{s}_0 - \tau_i\right)\right]\Delta\omega \cdot V(u, v, 0), \tag{D.3}$$

with instrumental delay time τ_i and

$$V(u, v, 0) = \int_{-\infty}^{\infty}\int_{-\infty}^{\infty} A(x, y)\cdot I(x, y) \cdot \exp[i2\pi(ux + vy)]dxdy, \tag{D.4}$$

where $A(x, y)$ and $I(x, y)$ are the antenna beam characteristic and radio wave source distribution, respectively; these are expressed in the coordinate in another Cartesian coordinate (x, y, z) to describe the sweeping vector $\boldsymbol{\sigma}$ as:

$$\boldsymbol{\sigma} = x\hat{\boldsymbol{x}} + y\hat{\boldsymbol{y}} + z\hat{\boldsymbol{z}}. \tag{D.5}$$

While the term $\exp[i\omega((1/c)\boldsymbol{B}\cdot\boldsymbol{s}_0 - \tau_i)]$ is considered as a constant in Eq. (D.3), $V(u, v, 0)$ is a significant factor which reflects the sweeping of the $\boldsymbol{\sigma}$ combined with baseline distribution $\boldsymbol{B}$ of the interferometer. By performing the inverse Fourier transformation, then, the radio sources are mapped being modified by the primary beam shape $A(x, y)$ as:

$$A(x, y)\cdot I(x, y) = \int_{-\infty}^{\infty}\int_{-\infty}^{\infty} V(u, v, 0) \cdot \exp[-i2\pi(ux + vy)]dudv. \tag{D.6}$$

In OASIO, there are a variety of selections for forming $V(u, v, 0)$ as given by Eq. (D.4), if we consider a wide distribution area of the antenna system covering the $(u, v, 0)$ plane. However, when we are allowed a distribution of only a few antennas, we need to use the Earth's rotation to expand the distribution of antennas in $(u, v, 0)$ plane. In OASIO, Rohlfs had described an example case of an east-west baseline interferometer where u and v are described by their Eq. (6.34) as:

$$u = \frac{\omega L}{c}\cos t, \qquad \text{and}$$

$$v = \frac{\omega L}{c}\sin t \cdot \sin\delta_0, \tag{D.7}$$

where t is the hour angle due to the Earth's rotation; and δ_0 is the declination of the center of the radio source.

In the present paper, to determine a direction in the IFFCM method, we start with Eqs. (26) and (27) in the main text, where the interferometric functions are described with $\cos A$, $\cos B$, and $\sin B$ with $A = \boldsymbol{k}_S \cdot (\boldsymbol{r}_j - \boldsymbol{r}_i) + \theta_i - \theta_j$ and $B = \boldsymbol{k}_P \cdot (\boldsymbol{k}_j - \boldsymbol{k}_i)$. The combinations $\cos A \cdot \cos B$ and $\cos A \cdot \sin B$ in Eqs. (26) and (27) are then expressed for

doi:10.5047/978-4-88704-171-4

signal part as:

$$\cos A \cdot \cos B = \frac{1}{4}[\exp(iA) \cdot \exp(iB) + \exp(iA) \cdot \exp(-iB) + \exp(-iA) \cdot \exp(iB) + \exp(-iA) \cdot \exp(-iB)], \quad \text{(D.8)}$$

$$\cos A \cdot \sin B = \frac{1}{4i}[\exp(iA) \cdot \exp(iB) - \exp(iA) \cdot \exp(-iB) + \exp(-iA) \cdot \exp(iB) - \exp(-iA) \cdot \exp(-iB)]. \quad \text{(D.9)}$$

In Eqs. (D.8) and (D.9), terms $\exp(iA) \cdot \exp(iB)$ and $\exp(-iA) \cdot \exp(-iB)$ are $\exp\{i[(k_s + k_p)(r_j - r_i) + (\theta_i - \theta_j)]\}$ and $\exp\{-i[(k_s + k_p)(r_j - r_i) + (\theta_i - \theta_j)]\}$ respectively; all these terms are eliminated because of phase mixing while taking average in time. Since the processes that search for a direction related to Eqs. (26) and (27) belong to the same principle, we will only consider the case which is described by Eq. (26) hereafter. As it has been described in detail in Subsec. 5.2 of the main text for the IFFCM, the term for sky noise N_{sky} given in Eq. (26) as:

$$N_{sky} = \frac{1}{2T_F} \int_{t_n}^{t_n+T_F} \left\{ \sum_{\ell=1}^{L} \sum_{m=1}^{M} E_{\ell m}^2(t) \cdot \cos[\boldsymbol{k}_{\ell m}(\boldsymbol{r}_j - \boldsymbol{r}_i) + (\theta_i - \theta_j)] \right\} \cdot \cos[\boldsymbol{k}_p(\boldsymbol{r}_j - \boldsymbol{r}_i)] dt, \quad \text{(D.10)}$$

is diminished by the integration of T_F. Then we start with the signal terms as:

$$Sig[C_{ij}(t_n)] = \frac{1}{2T_F} \int_{t_n}^{t_n+T_F} S_0^2(t) \cdot \exp\{i[\boldsymbol{k}_S(\boldsymbol{r}_j - \boldsymbol{r}_i) + (\theta_i - \theta_j)]\} \cdot \exp[-i\boldsymbol{k}_p(\boldsymbol{r}_j - \boldsymbol{r}_i)] dt. \quad \text{(D.11)}$$

In Eq. (D.11) $\boldsymbol{r}_i$ and $\boldsymbol{r}_j$ are position vectors of the i-th and j-th observation stations of the present interferometer system, respectively; then $(\boldsymbol{r}_j - \boldsymbol{r}_i)$ is the baseline vector of the present IFFCM that is expressed by $\boldsymbol{B}$ in OASIO. When we consider the east-west direction of the baseline vector, $\boldsymbol{r}_j - \boldsymbol{r}_i$ is expressed in the equatorial coordinate system, as:

$$\boldsymbol{r}_j - \boldsymbol{r}_i = -L \sin\Phi \cdot \boldsymbol{x}_e + L \cos\Phi \cdot \boldsymbol{y}_e, \quad \text{(D.12)}$$

where L is the baseline length; and $\boldsymbol{x}_e$ and $\boldsymbol{y}_e$ are unit vectors in the vernal equinox-equatorial coordinate system. The unit vector $\boldsymbol{x}_e$ indicates the solar direction in the vernal equinox while $\boldsymbol{y}_e$ is defined as $\boldsymbol{y}_e = \boldsymbol{z}_e \times \boldsymbol{x}_e$ with respect to the unit vector $\boldsymbol{z}_e$ directed along the rotation axis of the Earth, towards the north pole, also in the vernal equinox-equatorial coordinate system. In Eq. (D.12), angle Φ is defined as:

$$\Phi = \Omega_e(t - t_0) + \varphi_j, \quad \text{(D.13)}$$

where t and t_0 are the observation time and initial time of the start of an observation, respectively; and Ω_e and φ_i are the angular velocities of the rotating Earth and longitude of the i-th observation station of the interferometer. The radio waves from the source in the direction given by the unit vector $\widehat{\boldsymbol{k}_p}$ where the right assention and declination are given respectively by R_A and δ is expressed by:

$$\boldsymbol{k}_p = \frac{2\pi}{\lambda}\widehat{\boldsymbol{k}_p} = \frac{2\pi}{\lambda}(\cos R_{A\cdot}\cos\delta \cdot \boldsymbol{x}_e + \sin R_{A\cdot}\cos\delta \cdot \boldsymbol{y}_e + \sin\delta \cdot \boldsymbol{z}_e). \quad \text{(D.14)}$$

Then $\boldsymbol{k}_p(\boldsymbol{r}_i - \boldsymbol{r}_j)$ in the argument of the exponential function in Eq. (D.11) is given by:

$$\boldsymbol{k}_p(\boldsymbol{r}_i - \boldsymbol{r}_j) = \frac{2\pi}{\lambda} L \cos\delta \cdot \sin(R_{A\cdot} - \Phi). \quad \text{(D.15)}$$

To compare IFFCM with OASIO we express the sweep of the direction of $\boldsymbol{k}_p$ using $\Delta\boldsymbol{k}_p$ as:

$$\boldsymbol{k}_p = \boldsymbol{k}_S + \Delta\boldsymbol{k}_p. \quad \text{(D.16)}$$

That is, Eq. (D.16) in IFFCM is equivalent to Eq. (D.1) in OASIO. Then we introduce small variations of the right ascension $\Delta R_{A\cdot}$ and declination $\Delta\delta$ centered at $R_{AS\cdot}$ and δ_S to define $\Delta\boldsymbol{k}_p$ in the equatorial coordinate system; that is,

$$(\boldsymbol{k}_S + \Delta\boldsymbol{k}_p)(\boldsymbol{r}_i - \boldsymbol{r}_j) = \frac{2\pi}{\lambda} L \cos(\delta_S + \Delta\delta) \cdot \sin(R_{AS\cdot} + \Delta R_{A\cdot} - \Phi). \quad \text{(D.17)}$$

Considering the small values of $\Delta R_{A\cdot}$ and $\Delta\delta$ it follows that:

$$\Delta\boldsymbol{k}_p(\boldsymbol{r}_i - \boldsymbol{r}_j) = \frac{2\pi}{\lambda} L[\cos(\Phi - R_{AS\cdot})\cos\delta_S \Delta R_{A\cdot} + \sin(\Phi - R_{AS\cdot}) \cdot \sin\delta_S \cdot \Delta\delta] \quad \text{(D.18)}$$

with

$$\boldsymbol{k}_S(\boldsymbol{r}_i - \boldsymbol{r}_j) = -\boldsymbol{k}_S(\boldsymbol{r}_j - \boldsymbol{r}_i) = \frac{2\pi}{\lambda} L \cos\delta_S \cdot \sin(R_{AS\cdot} - \Phi). \quad \text{(D.19)}$$

In Eq. (D.18), angle $\Phi - R_{AS\cdot}$ is given using Eq. (D.13) as:

$$\Phi - R_{AS\cdot} = \Omega_e(t - t_0) + \varphi_i - R_{AS\cdot}. \quad \text{(D.20)}$$

When we select the start time t_0 to be $(\varphi_i - R_{AS\cdot})/\Omega_e$ then, Eq. (D.18) can be further rewritten by:

$$\Delta\boldsymbol{k}_p(\boldsymbol{r}_i - \boldsymbol{r}_j) = \frac{2\pi}{\lambda} L[\cos\Omega_e t(\cos\delta_S \Delta R_{A\cdot}) + \sin\Omega_e t \cdot \sin\delta_S \cdot \Delta\delta]. \quad \text{(D.21)}$$

Corresponding to expressions in Eqs. (D.6) and (D.7), we rewrite Eq. (D.18) as:

$$\Delta\boldsymbol{k}_p(\boldsymbol{r}_i - \boldsymbol{r}_j) = 2\pi(ux + vy) \quad \text{(D.22)}$$

doi:10.5047/978-4-88704-171-4

where $x = \cos\delta_S \Delta R_{A\cdot}$ and $y = \Delta\delta$; these are identical with the definition of the AOSIO case. We obtain u and v from Eq. (D.18) so that:

$$u = \frac{\omega L}{c}\cos\Omega_e t \qquad \text{and}$$
$$v = \frac{\omega L}{c}\sin\Omega_e t \cdot \sin\delta_S, \tag{D.23}$$

where $(\omega L/c) = kL = 2\pi L/\lambda$. We see that the set of equations Eq. (D.23) is completely identical with Eq. (D.7) of AOSIO when we understand that Rohlfs's expression of hour angle t is same as $\Omega_e t$.

By unifying expressions from Eq. (D.7) in AOSIO and Eq. (D.23) in the present IFFCM, the basic equation for source mapping, using the Earth's rotation in AOSIO which is given by Eq. (D.6), is rewritten for the narrowly defined declination range $\Delta\delta_S$ with an assumed time interval from t_0 to t, given by:

$$A(x,y)\cdot I(x,y) = \int_{t_0}^{t} V^*(u,v,0) \cdot \exp[-i2\pi(ux+vy)]\cdot dt, \tag{D.24}$$

where

$$V^*(u,v,0) = -\frac{\Omega_e}{2}\left(\frac{2\pi L}{\lambda}\right)^2 \cos\delta_S \Delta\delta_S \cdot \int_{-\infty}^{\infty}\int_{-\infty}^{\infty} A(x,y)\cdot I(x,y) \cdot \exp[i2\pi(ux+vy)]dxdy. \tag{D.25}$$

When we substitute equations spanning Eq. (D.15) to Eq. (D.23) into Eq. (D.11), it follows that:

$$Sig[C_{ij}(t_n)] = \frac{1}{2T_F}\int_{t_n}^{t_n+T_F} U^*(u,v,0) \cdot \exp[-i2\pi(ux+vy)]\cdot dt, \tag{D.26}$$

where

$$U^*(u,v,0) = S_0^2(t_n)\cdot\exp[i(\theta_i-\theta_j)]. \tag{D.27}$$

Thus we can see that the principles of present IFFCM are identical to the method of AOSIO which has been known as standard method. This is clear by comparing Eqs. (D.24) and (D.26) with Eq. (D.27), where $S_0^2(t_n)$ is modified by the primary antenna beam characteristic (details for primary antenna beam effects are described in Subsec. 8.3 in main text).

When we see the center direction of the source, by taking $x = 0$ and $y = 0$ in Eq. (D.26) with Eq. (D.27) together with the complex conjugate, it follows that:

$$\begin{aligned} &Sig[C_{ij}(t_n)] \\ &\quad = \frac{1}{2}S_0^2(t_n)\{\exp[i(\theta_i-\theta_j)] + \exp[-i(\theta_i-\theta_j)]\} \\ &\quad = S_0^2(t_n)\cos(\theta_i-\theta_j). \end{aligned} \tag{D.28}$$

Thus we can see identity between the principles of present IFFCM and well understood AOSIO. Further, when we consider the combinations of term $(-1/i)\exp(iA)\cdot\exp(-iB)+C.C$ relating to Eq. (D.9), we have relation, corresponding to Eq. (D.28) as

$$\begin{aligned} &Sig[S_{ij}(t_n)] \\ &\quad = \frac{1}{2i}S_0^2(t_n)\{\exp[i(\theta_i-\theta_j)] - \exp[-i(\theta_i-\theta_j)]\} \\ &\quad = S_0^2(t_n)\sin(\theta_i-\theta_j). \end{aligned} \tag{D.29}$$

Appendix E.

For the case of the Kerr metric (Kerr, 1963) in spherical coordinates for space that is given by

$$\begin{aligned} ds^2 = &-c^2\left(1-\frac{rr_g}{\Sigma}\right)dt^2 - \frac{2carr_g\sin^2\theta}{\Sigma}dtd\varphi \\ &+\frac{\Sigma}{\Delta}dr^2 + \Sigma d\theta^2 \\ &+\left(r^2+a^2+\frac{a^2rr_g\sin^2\theta}{\Sigma}\right)\sin^2\theta d\varphi^2 \end{aligned} \tag{E.1}$$

with $r_g = \frac{2GM}{c^2}$, $a = \frac{J}{Mc}$, $\Sigma = r^2 + a^2\cos^2\theta$ and $\Delta = r^2 - rr_g + a^2$, we make an approximate approach paying special attention to the event horizon in the equatorial plane. We consider the case of a Kerr black hole with maximum rotation where $a \approx 0.5r_g$; therefore the position of the event horizon r_E is located close to $0.5r_g$. In the equatorial plane ($\theta = \pi/2$) the inherent length ds given by Eq. (E.1) is expressed, taking $d\theta = 0$, as

$$\begin{aligned} ds^2 = &-c^2\left[\left(1-\frac{r_g}{r}\right) - \frac{2car_g}{r}\Omega \right. \\ &\left. +\left(r^2+a^2+\frac{a^2r_g}{r}\right)\Omega^2\right]dt^2 + \frac{r^2}{\Delta}dr^2 \end{aligned} \tag{E.2}$$

where $\Omega = d\varphi/dt$ which indicates the angular frequency of the rotating space of a Kerr black hole. By considering the conditions $a \approx 0.5r_g$ and $\Delta \approx 0$ near the event horizon, where Ω approach to $ca/(r_g r_E)$, Eq. (E.2) is rewritten to

$$\begin{aligned} ds^2 = &-c^2\left[1-\frac{r_g}{r}+\frac{1}{4}\left(\frac{r_g}{r}\right)^2\cdot\frac{r}{r_E}\left(2-\frac{r}{r_E}\right)\right]dt^2 \\ &+\frac{1}{1-\frac{r_g}{r}+\frac{1}{4}\left(\frac{r_g}{r}\right)^2}dr^2 \end{aligned} \tag{E.3}$$

where r_E is given by $\Delta = 0$ as $r_E = (r_g + \sqrt{r_g^2 - 4a^2})/2$.

The expression Eq. (E.3) can be further rewritten as:

$$\begin{aligned} ds^2 = &-c^2\left[\left(1-\frac{r_g}{2r}\right)^2\cdot(1+F(r))\right]dt^2 \\ &+\frac{1}{\left(1-\frac{r_g}{2r}\right)^2}dr^2, \end{aligned} \tag{E.4}$$

where

$$F(r) = -\left(\frac{1}{1-\frac{2r}{r_g}}\right)^2\left(1-\frac{r}{r_E}\right)^2$$

doi:10.5047/978-4-88704-171-4

which tends to zero at $r = r_E$.

When we are in the spacetime of rotating Kerr black holes with angular velocity Ω, then we can describe the metric close to the event horizon as Eq. (E.4) that gives a good approximation of the expression in the region close to the event horizon as

$$ds^2 = -c^2\left(1-\frac{r_g}{2r}\right)^2 dt^2 + \frac{1}{\left(1-\frac{r_g}{2r}\right)^2}dr^2. \tag{E.5}$$

Here the co-ordinate φ degenerates to being fixed to time t, as $\varphi = \Omega t + \varphi_M$ with a constant φ_M; that is all physical processes take place in the rotating frame with an approximate angular frequency near the event horizon $\Omega = ca/(r_E r_g)$.

Considering a spacetime which makes a spiraling free fall motion down into the Kerr black hole showing the characteristics of Minkowski spacetime with coordinate r' in the radial direction and time t'. For this case, there is no variation in polar and azimuth angles that give the relations $d\theta' = 0$ and $d\varphi' = 0$. When we define the metrics in black hole spacetime and Minkowski spacetime, as g_{ij} and η_{ij}, respectively, the transformation between black hole spacetime and the free falling Minkowski spacetime is given by

$$\eta_{mn} = g_{ij}\frac{\partial x^i}{\partial x'^m}\frac{\partial x^j}{\partial x'^n}. \tag{E.6}$$

When we write down individual formulae corresponding to Eq. (E.6) it follows that

$$\eta_{00} \equiv -1 = g_{00}\frac{\partial x^0}{\partial x'^0}\frac{\partial x^0}{\partial x'^0} + g_{11}\frac{\partial x^1}{\partial x'^0}\frac{\partial x^1}{\partial x'^0}, \tag{E.7}$$

$$\eta_{11} \equiv 1 = g_{00}\frac{\partial x^0}{\partial x'^1}\frac{\partial x^0}{\partial x'^1} + g_{11}\frac{\partial x^1}{\partial x'^1}\frac{\partial x^1}{\partial x'^1}, \tag{E.8}$$

where

$$g_{00} = -\left(1-\frac{r_g}{2r}\right)^2, \tag{E.9}$$

and

$$g_{11} = \frac{1}{\left(1-\frac{r_g}{2r}\right)^2}. \tag{E.10}$$

At the local place r, then the transformation of the coordinate system between the black hole spacetime and freely falling spiral- Minkowski spacetime can be described so as to satisfy Eqs. (E.7) and (E.8), as:

$$\begin{aligned} x'^0 &= a_{00}x^0 + a_{01}x^1 \\ x'^1 &= a_{10}x^0 + a_{11}x^1 \end{aligned} \tag{E.11}$$

where $x^0 = cdt$, $x^1 = dr$, $x'^0 = cdt'$ and $x'^1 = dr'$.

That is, the coefficients a_{00}, a_{01}, a_{10} and a_{11} are solved to satisfy Eqs. (E.7) and (E.8) together with the requirement that the square of inherent length of 4 dimensional spacetime is satisfied by:

$$-(x'^0)^2 + (x'^1)^2 = g_{00}(x^0)^2 + g_{11}(x^1)^2. \tag{E.12}$$

After mathematical manipulations we arrive at the solution as

$$\begin{aligned} dt &= \frac{dt'}{1-\frac{r_g}{2r}} \\ dr &= \left(1-\frac{r_g}{2r}\right)dr'. \end{aligned} \tag{E.13}$$

The invers transformation is then given by

$$\begin{aligned} dt' &= \left(1-\frac{r_g}{2r}\right)dt \\ dr' &= \frac{1}{1-\frac{r_g}{2r}}dr. \end{aligned} \tag{E.14}$$

The frequency f_M of waves which show phase shift $\Delta\emptyset$ in time interval dt' in the Minkowsky spacetime, is then observed in the Kerr black hole spacetime as f_K following the relation given by

$$\begin{aligned} f_M &= \frac{1}{2\pi}\left(\frac{\Delta\emptyset}{dt'}\right) \\ &= \frac{1}{2\pi}\left[\frac{\Delta\emptyset}{\left(1-\frac{r_g}{2r}\right)dt}\right] = \frac{f_K}{\left(1-\frac{r_g}{2r}\right)}. \end{aligned} \tag{E.15}$$

The expression of the inherent length given by Eq. (E.5) shows that we can apply the metric even inside the event horizon; but the equation of the transformation given by Eq. (E.14) shows that the expression should be changed to

$$\begin{aligned} dt' &= -\left(1-\frac{r_g}{2r_I}\right)dt_I \\ dr' &= -\frac{1}{1-\frac{r_g}{2r_I}}dr_I \end{aligned} \tag{E.16}$$

for the spacetime-t_I and r_I inside the event horizon, to keep the physical meaning of time passage rigorous.

Appendix F.

To show the possibility of generation of the whistler mode waves interacting with electrons falling into the black hole in the region close to the event horizon (RCEH), we apply a model where the incoming electron beam gives an additional moment of motion to the electrons in the plasma, coherently harmonized with the wave fields. That is, we are able to use Appleton-Hartree's equation where the coherent plasma motion is described as,

$$Nm\frac{d\boldsymbol{V}}{dt} = -Ne(\boldsymbol{E} + \boldsymbol{V}\times\boldsymbol{B}_0) + \kappa Nm\boldsymbol{V}. \tag{F.1}$$

doi:10.5047/978-4-88704-171-4

In the plasma media where electrons are mixed with neutral particles, the last term in Eq. (F.1) is expressed by $-\nu N m\boldsymbol{V}$ which indicates the momentum loss of the electron motion harmonized with the oscillation of the wave fields by colliding with neutral particles; i.e., that means the damping of the electromagnetic waves. As opposed to the wave damping case, we use the expression given by Eq. (F.1) to produce a gain in momentum of the electron motions harmonized with the oscillation of the wave fields due to the cyclotron frequency resonance of the electron beam. The term $+\kappa N m\boldsymbol{V}$ has a positive sign and the coefficient κ indicates the rate of increase of the momentum per second per each electron with unit $m\boldsymbol{V}$.

Then, we can follow the Appleton-Hartree's equation by changing the sign of the collision term Z to positive to describe the growth of whistler wave modes that result from an encounter with electron beams with the condition of the electron cyclotron resonance. Let n be the refractive index of the complex quantity with real part n_R and imaginary part n_I; that is,

$$n = n_R + i n_I \tag{F.2}$$

where i is the imaginary unit. Using the traditional expression of Appleton Hartree's equation as $X = \omega_P/\omega$, $Y = \Omega/\omega$, and $Z = \kappa/\omega$, for plasma angular frequency, electron cyclotron angular frequency, and momentum increasing ratio, respectively; the square of the refractive index is given by

$$n^2 = 1 - \frac{X(1 - X + iZ)}{(1 + iZ)(1 - X + iZ) - (1/2)Y^2 \sin^2\theta \pm \sqrt{(1/4)Y^4 \sin^4\theta + Y^2 \cos^2\theta \cdot (1 - X + iZ)^2}}. \tag{F.3}$$

As the first step to express the refractive index n by rewriting Eq. (F.3), we introduce the following expressions as:

$$K_R = 1 - X - Z^2 - (1/2) \cdot Y^2 \sin^2\theta \pm (A^2 + B^2)^{1/4} \cdot \cos\xi, \tag{F.4}$$

$$K_I = Z(2 - X) \pm (A^2 + B^2)^{1/4} \cdot \sin\xi, \tag{F.5}$$

where A, B, and ξ are given by following equations,

$$A = (1/4)Y^4 \sin^4\theta + Y^2 \cos^2\theta[(1 - X)^2 - Z^2], \tag{F.6}$$

$$B = 2Z(1 - X)Y^2 \cos^2\theta, \tag{F.7}$$

and

$$\xi = \frac{1}{2} \tan^{-1}\left(\frac{B}{A}\right). \tag{F.8}$$

Using expressions from Eq. (F.4) to Eq. (F.8), then, we have the real and imaginary parts of the refractive index n as,

$$n_R = \frac{\{[K_R^2 + K_I^2 - X(1 - X)K_R - ZXK_I]^2 + X^2[(1 - X)K_I - ZK_R]^2\}^{1/4}}{\sqrt{K_R^2 + K_I^2}} \times \cos\left\{\frac{1}{2} \tan^{-1} \frac{X[(1 - X)K_I - ZK_R]}{K_R^2 + K_I^2 - X(1 - X)K_R - ZXK_I}\right\} \tag{F.9}$$

and

$$n_I = \frac{\{[K_R^2 + K_I^2 - X(1 - X)K_R - ZXK_I]^2 + X^2[(1 - X)K_I - ZK_R]^2\}^{1/4}}{\sqrt{K_R^2 + K_I^2}} \times \sin\left\{\frac{1}{2} \tan^{-1} \frac{X[(1 - X)K_I - ZK_R]}{K_R^2 + K_I^2 - X(1 - X)K_R - ZXK_I}\right\}. \tag{F.10}$$

(Online published on December 2, 2019)

doi:10.5047/978-4-88704-171-4